JEOL NEWS

(a)

(b)

Electron beam

Electron beam

B

B

Over-focused
image plane

(c)

50 nm

150 nm

(d)

100 nm

JEOL

Contents

Cover micrograph

(a) Schematic of a Bloch-type skyrmion. The arrows show magnetic spins. (b) Schematics of Lorentz transmission electron microscopy (LTEM) imaging for skyrmions with counter clockwise (CCW) (left) and clockwise (CW) (right) spin helicities (twist directions of spins in the skyrmions). (c) Over-focused LTEM images (upper panels) and the corresponding magnetization textures (lower panels) obtained under a normal magnetic field of 240 mT at RT (left panels; β-Mn type Co-Zn-Mn alloy) and under a normal magnetic field of 50 mT at 100 K (right panels; $Fe_{0.5}Co_{0.5}Ge$). The colors and arrows depict the magnitude and direction of in-plane magnetizations, while the black means the out-of-plane magnetizations. (d) Skyrmion crystal (SkX) realized under a normal magnetic field of 100 mT in a FeGe thin plate at 260 K.

Lorentz TEM Study on Magnetic Skyrmions and Their Dynamics

Xiuzhen Yu[1] and Yoshinori Tokura[1,2]

[1] RIKEN Center of Emergent Matter Science (CEMS)
[2] Department of Applied Physics, The University of Tokyo

The magnetic skyrmion is a vortex-like topological particle, in which spins swirl from the north-pole in the core to the south-pole in the outermost circle of the vortex. Nanometric skyrmions realized recently in magnetic materials are promising for applications to the high-density and low-power-consumption magnetic memory. The key research issue for practical applications is to realize and manipulate such a nanoscale spin-ensemble object in a well controlled manner. We report here the Lorentz transmission electron microscopy (LTEM) studies on magnetic skyrmions and their dynamics under external magnetic fields, spin-polarized electric current and irradiated electron beam in helimagnets/uniaxial-ferromagnets with non-centrosymmetric/centrosymmetric structures. We have developed a useful technique not only to create skyrmions by a precise control of the magnetic field in a standard transmission electron microscope (TEM), but also to view the skyrmions and their dynamics in real-space in the LTEM mode.

Introduction

Electron spins play a key role not only in magnetism but also in many emergent phenomena of solids, such as the high-T_C superconductor [1] and colossal magneto-resistance (CMR) in condensed matters [2]. In addition, electron spin can act as an information bit, namely form spintronics – a field of the manipulation of electron spin by electron current, heat current, etc. [3-4]. Among them, the topological spin textures emerging in magnetic materials are attracting much attention in materials physics and are expected to contribute to future highly functional devices [5-6]. Magnetic skyrmion is one such example and promising for the application of the high-density and low-power consumption memory [6]. The skyrmion is vortex- like topological texture which was theoretically proposed more than half a century ago [7], but has only recently been experimentally confirmed in chiral-lattice magnets by using small angle neutron scattering (SANS) [8] and Lorentz transmission electron microscopy (LTEM) [9]. In a Bloch-type skyrmion shown in **Fig. 1**(a), several hundreds of spins swirl with a unique direction and point down in the core and point up in the outermost circle of the skyrmion. The adjacent non-coplanar spins shown in the left panel of Fig. 1(b) subtend a solid angle $S_i \cdot (S_j \times S_k)$ named spin chirality, which acts on the conduction electrons as emergent (fictitious) magnetic field (B_{eff}). The whole spins in the skyrmion just wrap a unit sphere, i.e. subtending the spin solid angle of 4π. The skyrmion number or topological charge in real space, as defined

by $N_s = \frac{1}{4\pi} \int n \cdot \left(\frac{\partial n}{\partial x} \times \frac{\partial n}{\partial y} \right) dxdy, n = \frac{S(x, y)}{|S(x, y)|}$, corresponds to the fictitious magnetic flux carried by one skyrmion; it should deflect conducting electrons as a background field (see Fig. 1(c)), resulting in the novel electromagnetic transport such as the topological Hall effect [6]. As a counteraction of topological Hall effect, the Hall motion of skyrmion should occur as shown in Fig. 1(c) when the spin-polarized current passes though the skyrmion [6]. If the skyrmion density is large enough, the magnitude of the fictitious field should become gigantic (e.g. about 400 Tesla for a 3 nm-spaced skyrmion lattice) and hence produce a huge topological Hall effect [6].

Although the magnetic skyrmion causes the enormous interest in basic physics and future applications to spintronics [10], it is difficult to be realized and manipulated due partly to its unstable nature in the (three-dimensional) 3D systems [8] and partly to the minuscule size (smaller than 100 nm in general [6]) close to or less than the spatial resolutions of real-space observation techniques of magnetism.

The skyrmion crystal (SkX) was identified first by SANS measurements in a helimagnet MnSi with non-centrosymmetric cubic structure. At the ground state, the magnetic structure shows a proper screw structure with a periodicity of ~ 19 nm, which is induced by Dzyaloshinskii-Moriya interaction (DMI) originating from the relativistic spin-orbit interaction [8]. With respect to the external magnetic field applied perpendicular to the wave vector of screws, the multiple wave vectors are generated. When the three vectors meet each other with angle

〉〉 2-1 Hirosawa, Wako, Saitama 351-0198, Japan | E-mail: yu_x@riken.jp

Fig. 1

(a)

Bloch-type skyrmion

(b)

Solid angle   Electron spin   Emergent filed

(c)
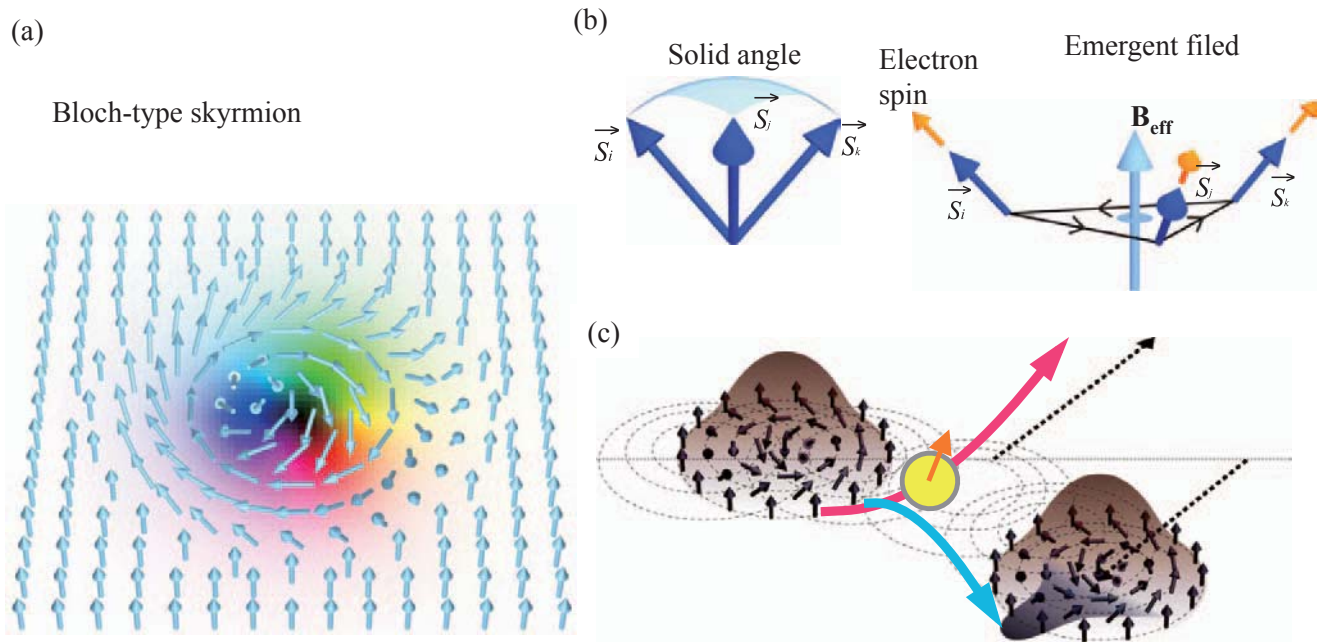
Schematics of (a) a Bloch-type skyrmion, (b) the solid angle subtended three spins and the emergent (fictitious) magnetic field B_{eff} induced by these non-coplanar spins, (c) topological Hall effect and Hall motion of skyrmion.

of 120-degree, a SkX with six-fold symmetry emerges in the plane perpendicular to the external magnetic field irrespective of the crystal lattice orientation. SkX seems to occur only within a limited temperature range in the 3D bulk sample [8]. After this work, LTEM observations confirmed the spin textures for a single skyrmion and SkX in one other helimagnetic $Fe_{0.5}Co_{0.5}Si$ thin plate [9]. The study demonstrated that the spins in the skyrmion align parallel/anti-parallel to the normal magnetic field at the core/peripheral and swirling between the core and outmost circle of skyrmion, respectively. LTEM has also established and stabilized the skyrmion phase in thin plates of helimagnets $Fe_{0.5}Co_{0.5}Si$ [9] and FeGe [11]: When the plate thickness is smaller than the helical period, i.e. magnetically two-dimensional (2D), the thinner plate sample has a much wider window of skyrmion phase in the $T - B$ plane. These results show a good agreement with Monte Carlo simulations: skyrmion is remarkably stabilized in 2D thin samples [9]. After these studies, skyrmion attracts much attention not only in condensed-matter physics but also in the field of spintronics [5-6, 10].

In this paper, we present how to realize the skyrmion in two standard transmission electron microscopes (TEMs) (JEM-2100F and JEM-2800, JEOL). We show the real space imaging of SkX and its dynamics by taking advantage of LTEM under controllable magnetic field, spin-polarized electric current and irradiation of electron beam.

Principles of LTEM with controlled magnetic field

The LTEM is very powerful for observing spontaneous magnetic configurations in ferromagnetic (FM) materials owing

to its high spatial resolution (< 2 nm under zero magnetic field). **Figure 2**(a) is a schematic diagram for the principle of LTEM: Magnetizations perpendicular to the incident electron beam induce a Lorentz force normal to both magnetizations and the electron beam, while the magnetizations parallel to the incident electron beam has no magnetic interaction. The Lorentz forces induced by perpendicular magnetizations deflect the electron beam, resulting in the convergent (bright) and divergent (dark) contrasts in the defocused LTEM image planes. This type of LTEM observation technique is known as the Fresnel method [12] and can be used effectively to obtain information about the in-plane magnetization normal to irradiated electron beam. Figures 2(b)-2(d) show the under-focused LTEM images for (b) 180-degree magnetic domains in a FM thin plate with the in-plane easy axis of magnetization, (c) stripe domains in a uniaxial FM thin film with the out-of-plane easy axis of magnetization and (d) stripes related to the projective imagery of helical structure, respectively. Figures 2(e)-2(f) are the corresponding magnetization profiles of M_y along the x axis. The bright and dark line contrasts in Figs. 2(b) and 2(c) mean the antiparallel domain walls, and the alternative bright and dark stripes in Fig. 2(d) indicate a proper screw structure with a short period of 5 nm. The alternative up-down domains (the out-of-plane magnetic domains) separated by the domain walls with opposite helicities (spin rotating directions) show a "Fan" stripe domain structure.

Since the electron beam is sensitive to the external electromagnetic field, LTEM has a very limited capability in applying magnetic field to samples. This means that it is almost impossible to generate and observe skyrmion by the conventional LTEM, because the magnetic skyrmions are

Fig. 2
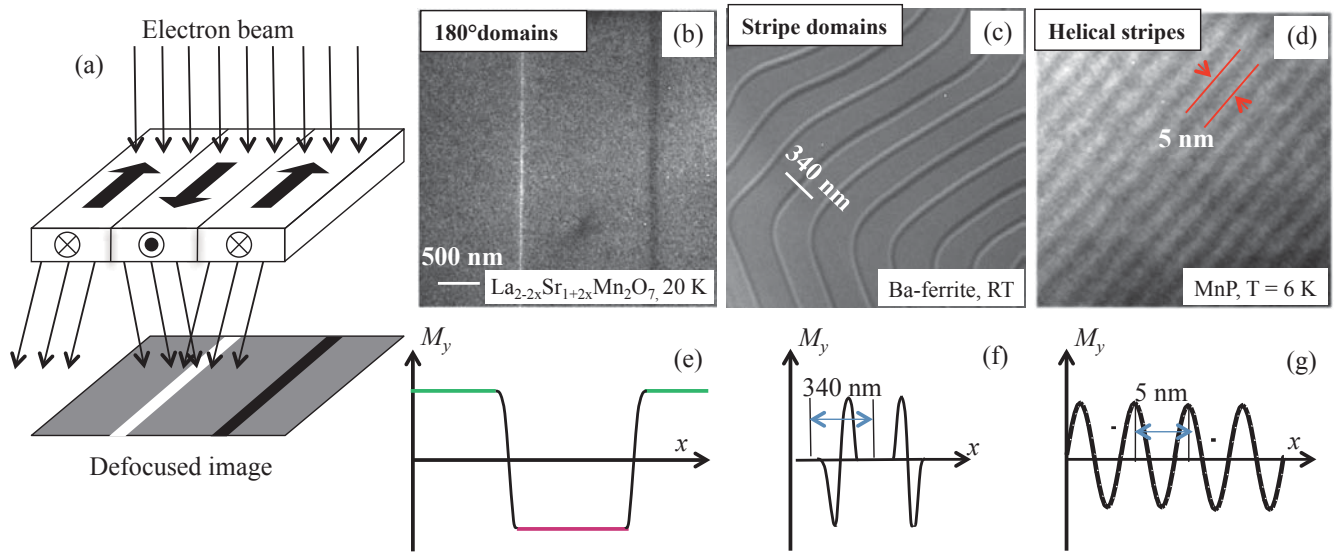
(a) Schematic of Lorentz transmission electron microscopy (LTEM). (b-d) Under-focused LTEM images for the spontaneous magnetic domain (MD) structures of (b) 180-degree domains, (c) stripe domains, and (d) helical stripes. (e-g) The line profiles of transverse component M_y along the x axis in the corresponding MDs shown in the (b-d).

usually generated by an appropriate magnetic field in the magnetic systems, namely the transformation from helical stripes into SkX is hardly obtained in a conventional LTEM. On the other hand, the magnitude of applied fields to generate skyrmions depends strongly on the material parameters and has a large range from zero field up to several Tesla [6]. To create and then visualize skyrmions at the same time, we consider to use the magnetic lens of a standard TEM and then to induce the external magnetic field which is almost perpendicular to the thin TEM sample plane [9]. The fine control of lens current gives us a precise control of the magnetic field. Usually, in the standard TEM, normal operation mode uses a high lens current to make focal length as short as possible, and hence to achieve higher magnification and better atomic-level resolution. A strong magnetic field of around 2 to 3 T is always applied to the sample in the standard TEM [12]. Obviously, skyrmions cannot exist stably under such a strong magnetic field except special cases. However, by decreasing the objective lens current in so-called "free lens-control mode", we can reduce the magnetic field applied on the sample [13]. By carefully adjusting the lens control system, we finally found the appropriate conditions to convert helical stripes into skyrmions. Also, under such an imaging condition, the focal length of magnetic lens drastically increases, i.e., that the diffraction pattern is enlarged much larger than the standard diffraction mode. Thus, we can expect that detection of the electron beam deflection caused by in-plane magnetizations of the sample becomes much easier. As a consequence, reducing the objective lens current can generate skyrmions and also make detection of electron beam deflection induced by magnetic interaction much easier.

On the other hand, the TEM samples are always thinned for electron transparency, which turns out to be favorable for stabilizing 2D skyrmions in thin specimen. Furthermore, combining LTEM images with phase analysis method allows mapping of the spatial distribution of the magnetization.

Experimental

For the LTEM study on magnetic skyrmions and their dynamics, we target several correlated-electrons materials including helimagnets with non-centrosymmetric cubic structure and uniaxial ferromagnets with centrosymmetric structure. Among them, the single crystals $Fe_{0.5}Co_{0.5}Si$, Ba-ferrite with Sc doping, and $La_{2-2x}Sr_{1+2x}Mn_2O_7$ ($x = 0.315$) were grown by using the floating zone (FZ) method [9, 14-15], while the single crystals FeGe and Cu_2OSeO_3 were prepared by the chemical vapor transport technique. Samples for LTEM observation were thinned to thicknesses below 100 nm through mechanical and ion beam polishing by using a MultiPrep™ polishing system (Allied High Tech) and a Precision Ion Polishing System (PIPS™) (model 691,Gatan Inc.). A microdevice composed of a FeGe thin plate and current-feed electrodes was fabricated by a Focused Ion Beam system (Hitachi FB2100). The obtained thin samples were placed in special TEM sample holders (HC3500 and ULTST, Gatan Inc.) and were observed in TEMs (JEM-2100F and JEM-2800, JEOL). Under the free lens-control mode, the current of the objective lens was first set to zero to obtain the helical spin texture. Then the current was gradually increased carefully until the magnetic skyrmion textures were successfully observed. The magnitude of magnetic field as a function of objective lens current was measured by a Hall probe in advance.

Determination of skyrmion helicity

The skyrmion arises most typically from helical structure under an external magnetic field in helimagnets with non-centrosymmetric structure as induced by strong DMI [16-17]. Skyrmion size and its helicity are determined by the material parameters: the size has a fixed magnitude proportional to the ratio of DMI and spin exchange interaction energies; the skyrmion helicity (spin swirling direction) is determined by the sign of DMI and hence also by crystal chirality [9, 11, 18-19].

Figures 3(a) and 3(b) show the one-to-one correspondence of crystal chirality and skyrmion helicity: In the case I, the counter-clockwise/clockwise skyrmion helicity responds to left-handed/right-handed crystal chirality when the external magnetic field applied from top-down; when the sign of spin orbit interaction is reversed (case II), the counter-clockwise/clockwise skyrmion helicity responds to right-handed/left-handed crystal chirality with the same situation of the applied field. The concept has been confirmed by using the convergent electron beam diffraction technique and LTEM observations [18-19]. In this paper, we leave out the confirmation of crystal chirality using the convergent electron beam diffraction technique which was described in the previous reports [18-19]. The followings show a technique to determine the skyrmion helicity by analyzing LTEM images.

Figure 3(c) is schematics of LTEM for imaging two skyrmions with opposite helicities at the over-focused image plane. The contrasts for the two skyrmions should reverse at the same defocused condition. Figure 3(d) demonstrates two over-focused LTEM images for isolated skyrmions. One is observed in $Co_8Zn_8Mn_4$ (left panel) with the left-handed crystal chirality and another is obtained in $Fe_{0.5}Co_{0.5}Ge$ (right panel) with the right-handed crystal chirality. To determine the spin helicity of the skyrmion, the three sets of images with under-, over- and just (or zero) focal-lengths were recorded by a Charge Coupled Device (CCD) camera (USC1000, Gatan Inc.), and then analyzed the in-plane magnetizations by the QPt software based on the transport of intensity equation (TIE) [20]. The spatial distribution of the magnetizations was deduced by such analyses and finally we successfully obtained the magnetization textures shown in Fig. 3(e). The colors and arrows depict the magnitude and direction of in-plane magnetizations, while the black means the out-of-plane magnetizations. These magnetization textures show clearly the counter-clockwise and clockwise helicities for the isolated skyrmions respectively.

Realization of skyrmion crystal phase in a helimaget FeGe thin plate

We have succeeded in realizations of the isolated skyrmions shown in Fig. 3 by LTEM observations with the application of normal magnetic fields. In some cases, it is also desirable to generate the skyrmion crystal (SkX) phase or increase the skyrmion density at higher temperatures, preferably at room temperature, to obtain large electromagnetic responses from the emergent magnetic field, such as topological Hall effect. Thus, we proceeded to realize SkX on a FeGe system with higher magnetic ordering transition temperature near room temperature

Fig. 3
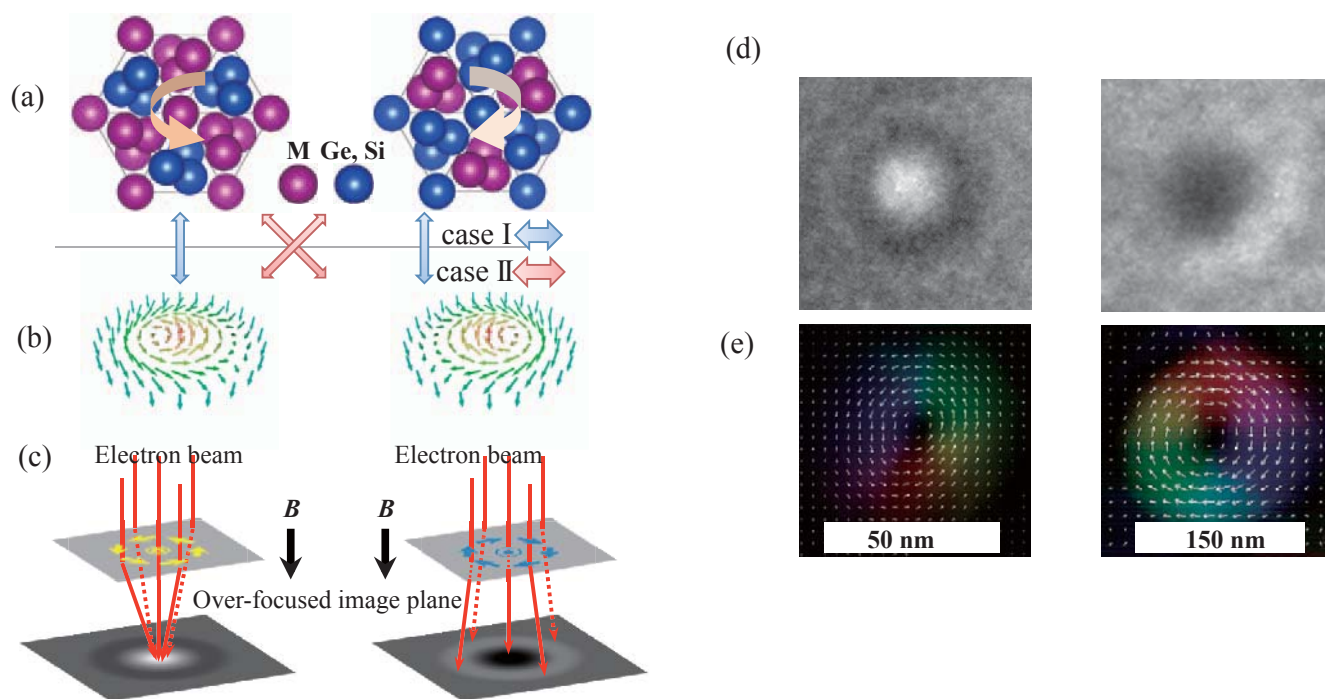
(a-b) Schematics of the crystalline structures and skyrmion configurations in helimagnets with opposite crystal chiralities [Ref. 19]. (c) Schematics of LTEM imaging for skyrmions with opposite spin helicities. (d) Over-focused LTEM images and (e) the corresponding magnetization textures obtained under a normal magnetic field of 240 mT at RT (left panels; β-Mn type Co-Zn-Mn alloy) and under a normal magnetic field of 50 mT at 100 K (right panels; $Fe_{0.5}Co_{0.5}Ge$).

such as ~ 278 K [11]. We have also succeeded in the creation of SkX and stabilization of SkX phase in 2D FeGe thin plates [11].

Figures 4(a) and 4(b) represent the color images obtained by TIE analyses of LTEM images in a FeGe thin plate at 260 K, only slightly below room temperature. Figure 4(a) is a magnetization texture obtained under zero magnetic field. The alternative stripe domains reveal a proper screw structure at the ground state. The period of helical structure is approximately 70 nm. As the magnetic field is applied perpendicularly to the helix, the striped pattern related to the helical structure starts to curve. When the magnitude of magnetic field is increased to 150 mT, the stripy pattern disappears almost completely and the perfect SkX with a hexagonal symmetry shown in Fig. 4(b) is created. The diameter of each skyrmion and the lattice parameter of the SkX are approximately the same value of about 80 nm. In TIE images of SkX, the relatively dark color indicates the out-of-plane magnetizations, rendering that the orientations of the core spins and the peripheral spins are perpendicular to the plate plane. Even though LTEM images cannot identify the up or down of the out-of-plane magnetization, the in-plane magnetic

components of the 2D skyrmions obtained theoretically by Monte Carlo simulations are in good agreement with our LTEM observations [9], strongly suggesting that the magnetizations at the outer region are expected to be aligned parallel and the core magnetizations aligned antiparallel to the magnetic field. The area of the outer region is larger than that of the core in skyrmions observed by LTEM, in accord with the magnetization data. On the other hand, colors and arrows in TIE image mean the magnitude and orientation of in-plane magnetizations, revealing the counter-clockwise skyrmion helicity. When the magnetic field was further increased to 280 mT, the SkX starts to be disintegrated. Skyrmions and ferromagnetic phases coexist at such higher magnetic fields. Finally, the skyrmions disappear almost completely and a single ferromagnetic domain with a uniform magnetic contrast in LTEM image is formed when the magnetic field is increased over 350 mT [11].

The detailed LTEM measurements for FeGe thin plates with different thicknesses produce the 2D SkX phase diagram in the T-B plane (Fig. 4(c)-4(d)) by systematically varying the magnetic field (B) and temperature (T). Color bar depicts

---

Fig. 4
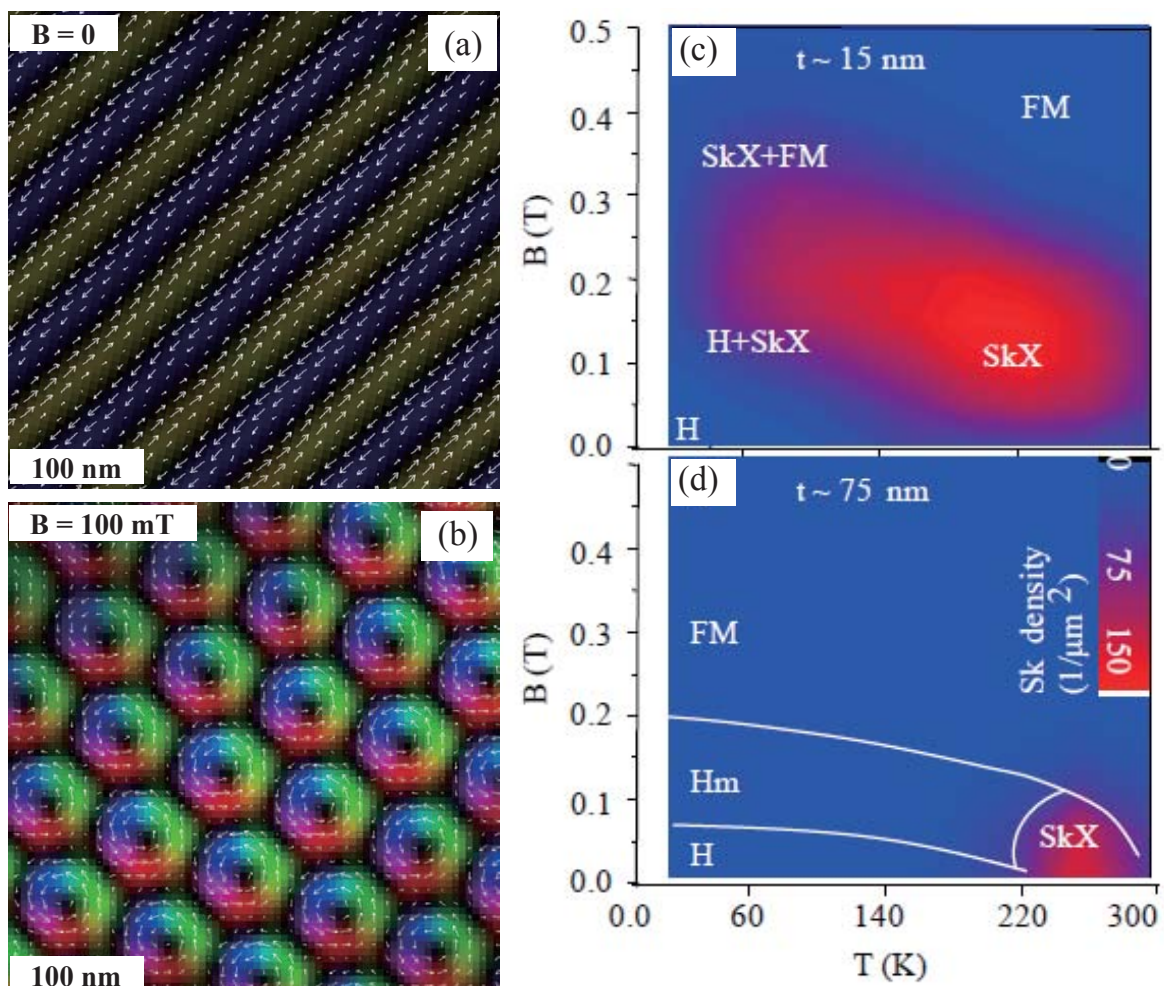
(a-b) Magnetization textures obtained under zero field and under a normal magnetic field of 100 mT in a (001) FeGe thin plate at 260 K. (c-d) Skyrmion crystal (SkX) phase diagrams in FeGe thin samples with different sample thicknesses.

the skyrmion number per 1 μm^2 and the t is the sample thickness. First, we change the magnitude of field at a constant temperature. In a thinner plate with $t \sim 15$ nm, we have observed that 1) the alternative bright and dark stripes indicate a proper screw structure realized under zero field; 2) the stripes change gradually into a mixed structure (denoted as H+SkX) with stripes and partial triangular lattice of skyrmions in over-focused images (the contrast is reversed in under-focused images) upon the application of normal magnetic field; 3) the stripes disappear completely and single-domain SkX with hexagonal symmetry is produced with increasing field to an appreciate value which strongly depends on the temperature; 4) SkX starts to collapse to the partial order of triangular skyrmion lattice accompanied by FM domains; 5) a uniform contrast related to a single-domain FM state with the magnetization along the field direction shows up when the field is above the saturated field which is a function of temperature. In the thicker plate with thickness of ~ 75 nm, we have carried out the similar experiments. In contrast to the results obtained in the thinner sample, no SkX appears at lower temperatures with applications of magnetic field, while the multidomains with random wave vectors have been observed. The magnetic fields for skyrmion formation are lower as a whole than those observed in thinner sample.

Next, we fix the magnitude of field and change temperature. At $T < 30$ K, no SkX emerges for thinner nor for thicker plate; at 30 K $< T < 210$ K, the SkX starts to appear only in the thinner plate; at 210 K $< T < T_N$ (278 K), the stable SkX has been observed in both thinner and thicker plates. Finally, SkX is melted and no magnetic contrast is discerned as expected as the temperature is above the T_N (278 K). These systematic LTEM observations are summarized as the phase diagrams in the T-B plane shown in Fig. 3(c) for a thinner plate and in Fig. 3(d) for a thicker plate. It is clearly discerned that contrary to the narrow window of SkX phase near T_N in the thicker plate or bulk, SkX phase extends to low temperatures in the thinner plate. These results demonstrate that the thinner the plate is the more stable SkX phase is in the plane of vertically-applied magnetic field vs. temperature.

A variety of topological spin textures in uniaxial ferromagnetic thin plates

We have realized SkX not only in helimagnets but also in thin plate samples of uniaxial ferromagnets while the skyrmions in these systems are commonly characterized by the skyrmion number (topological charge). There are discerned important differences as follows: 1) The size of the skyrmions as determined by the ratio of the dipolar and exchange interaction constants in uniaxial FM system is typically 100 nm-1 μm, while the size of the skyrmions induced by the DMI in helimagnetic system is 10-100 nm; 2) The helicity of skyrmions in helimagnets is fixed by the sign of the DMI, while the two states with opposite helicities are degenerate in uniaxial ferromagnet systems, and hence the skyrmion helicity represents an additional degree of freedom, resulting in the fertile spin textures accompanied by the helicity reversals [14]. We introduce here such a variety of topological spin textures realized in thin plates whose normal is parallel to the easy axis of magnetization.

The color panels in **Figs. 5**(a)-5(d) display the TIE results obtained by analyzing the LTEM images of the (001) thin plate of BaFe$_{12-x-0.05}$Sc$_x$Mg$_{0.05}$O$_{19}$ ($x = 1.6$). The in-plane magnetization textures form the complex maze-like spontaneous domain structure (Fig. 5(a)), very different from the simple sine-wave

curve of magnetization in the proper screw structure in non-centrosymmetric helimagnetic system (see Fig. 4(a)). The helicity reversals seem to occur randomly at many places [14]. Figure 5(b) shows the pattern of the lateral magnetizations in the SkX with a hexagonal symmetry at $B = 150$ mT, obtained by the TIE analyses. Contrary to the irregular shapes of the stripes, the regular SkX is built up by skyrmions with random distribution of counter-clockwise (see an enlargement shown in Fig. 5(c)) and clockwise (see an enlargement shown in Fig. 5(d)) helicities. Each skyrmion is composed of three concentric rings. Even the magnetization textures in these skyrmions are complex, the net topological number is the same as one skyrmion, e.g. in FeGe represented above. This is because that the in-plane magnetizations in the inner and outer rings are smaller than in the middle rings and reach maximum at the middle ring. The downward magnetizations at the outside of the skyrmion tilt slightly to the in-plane in the outer ring, then start to twist in the middle ring, and tilt again slightly to the in-plane in the inner ring, and finally reverse to the upward at the core of the inner ring. One triple-ring topological structure is identified as a single skyrmion with the pendulum-like motion accompanied by helicity reversals in the inner and outer rings.

Another novel form of nanoscale topological spin texture is a bound pair of skyrmions, termed biskyrmion. They are created in a thin bilayered manganese oxide La$_{2-2x}$Sr$_{1+2x}$Mn$_2$O$_7$ ($x = 0.315$) that is held at low temperature (~ 20 K) and under an applied magnetic field (~ 0.35 T). The size of the biskyrmions depends on the thickness of the sample and the strength of the external magnetic field. They appear to be relatively stable, although they are destroyed at temperatures > 50 K or at the applied magnetic field exceeding 0.4 T.

Figures 5(e)-5(g) represent an under-focused LTEM image, the corresponding magnetization texture, and its magnified image, respectively. The data demonstrate that the biskyrmion composes two skyrmions with opposite skyrmion helicities (one clockwise and the other counter-clockwise). Accordingly, the biskyrmions have a topological charge of 2, twice that of a single skyrmion. The doubled topological number in the biskyrmion is expected to cause a difference in the dynamics and also modify the skyrmion transport properties compared to the case of the single skyrmion. We have also found that they can be driven with three orders of magnitude lower current density than that for a drive of conventional FM domain walls [15]. These findings will bring about new development in designing novel magnetic memory devices with high-density and low-power consumption.

Current-driven skyrmion motion

A skyrmion carrying a topological charge acts as an effective magnetic flux. As an electron traverses the skyrmion, it should sense the effective Lorentz force, giving rise to the topological Hall effect [6]. As a counteraction of the topological Hall effect related to electron Hall motion, the skyrmion or SkX itself can exhibit a Hall motion. Similarly to the FM domain motion driven by spin-polarized electric current owing to the spin transfer torque (STT) [21], the electric current flowing on the skyrmion drives the skyrmion motion, not only along the electron flow but also the transverse (Hall) motion. The snapshots captured from an *in-situ* LTEM movie with a current flow are displayed in **Fig. 6**: the skyrmions starts to move under current up to 4.4 Acm^{-2} in region A; accompanied by the wobbling motion, skyrmions drag away from the current direction and flow out

of the view area at currents above 4.9 Acm^{-2}. Interestingly, skyrmions appear again in the region B with an increase of current above 9 Acm^{-2}, where skyrmions start to move firstly under a weak current of 4.2 Acm^{-2}. The survived skyrmions ensure that the skyrmion motion is driven by the electric current rather than the melting with possible current-induced heating. Systematic observations also show that, in contrast with the immobile stripe pattern related to the helical structure with current of 10 Acm^{-2}, the SkX flows away under an identical current excitation, indicating that the heat effect on skyrmion motion is negligible. It is observed that the critical current for a drive of SkX decreases with an increase of the temperature toward T_N [22].

## Unidirectional rotation of SkX with the irradiation of electron beam

We have found the electron beam with high energy induces the unidirectional rotation of SkX. **Figure 7**(a) is a schematic of the configuration of a TEM thin sample (light blue block) irradiated by the electron beam. The graded red circle represents the gradual change of local heat in the view area of TEM sample, which is generated by the irradiated beam. The *in-situ* LTEM movie (not shown) and its time-sequence snapshots for the fast Fourier transforms (FFTs) (see Fig. 7(b)) of SkX observed in an insulating helimagnet Cu_2OSeO_3 [23] demonstrate a unidirectional rotation of SkX. The rotation speed has been observed to depend strongly on the irradiation density of the electron beam. Figure 7(c) shows rotation speed of SkX

Fig. 5
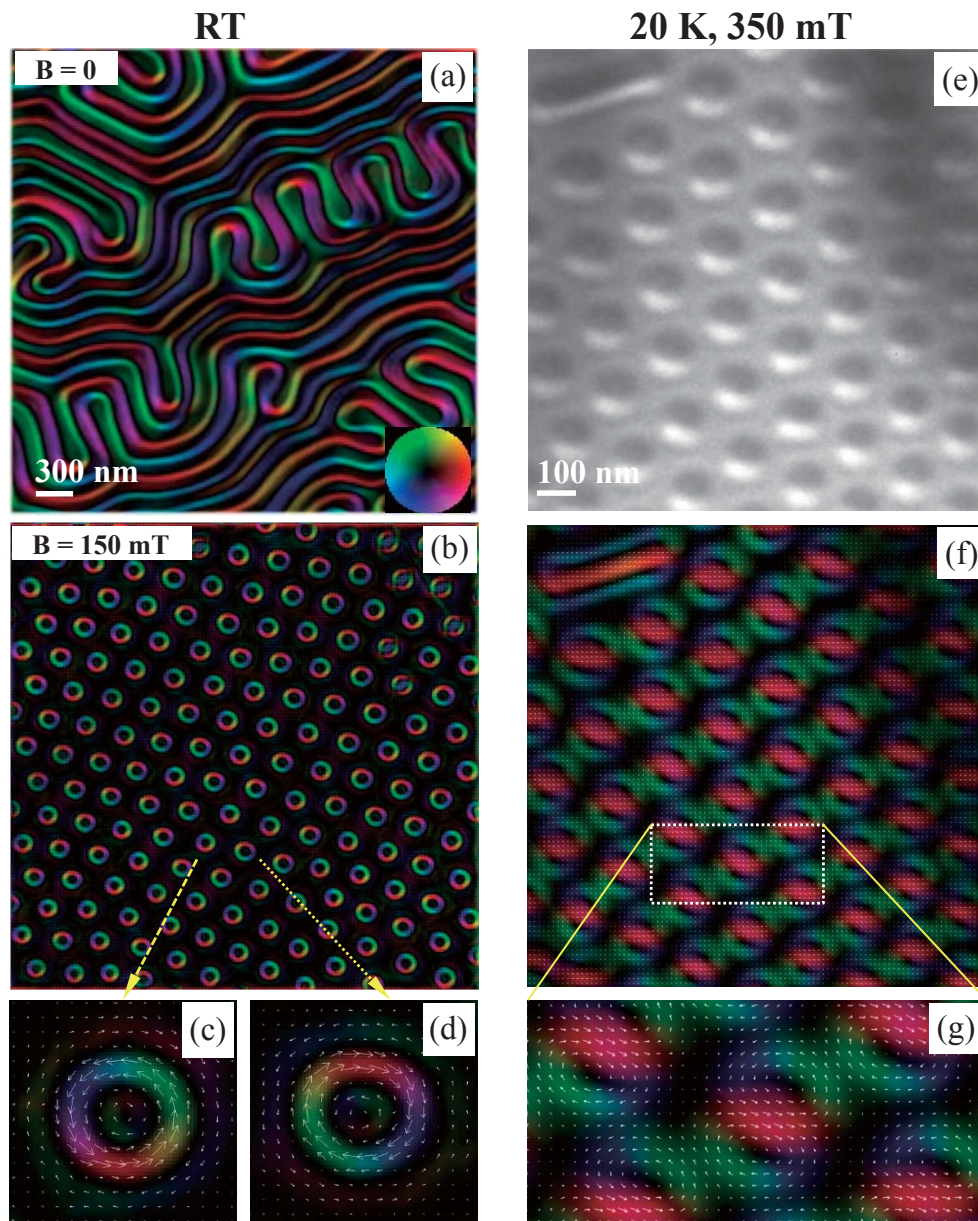
(a-b) Magnetization textures obtained under zero field and under a normal magnetic field of 150 mT in a (001) Ba-ferrite ($BaFe_{12-x-0.05}Sc_xMg_{0.05}O_{19}$ (x = 1.6)) thin plate at room temperature. (c-d) Magnified images of single bubbles shown in (b). The color wheel shown in the inset of (a) indicates the direction of in-plane magnetizations. (e-f) Under-focused LTEM images and the corresponding magnetization textures obtained under a normal magnetic field of 350 mT at 20 K in a bilayered manganite $La_{2-2x}Sr_{1+2x}Mn_2O_7$ (x = 0.315). (g) The magnified image of the boxed area shown in (f).

Fig. 6

273 K, 100 mT

(a) $J = 0$
(b) 4.2 A/cm^2
(c) 4.4 A/cm^2
(d) 4.7 A/cm^2
(e) 4.9 A/cm^2
(f) 9 A/cm^2

moving direction

Current direction

100 nm
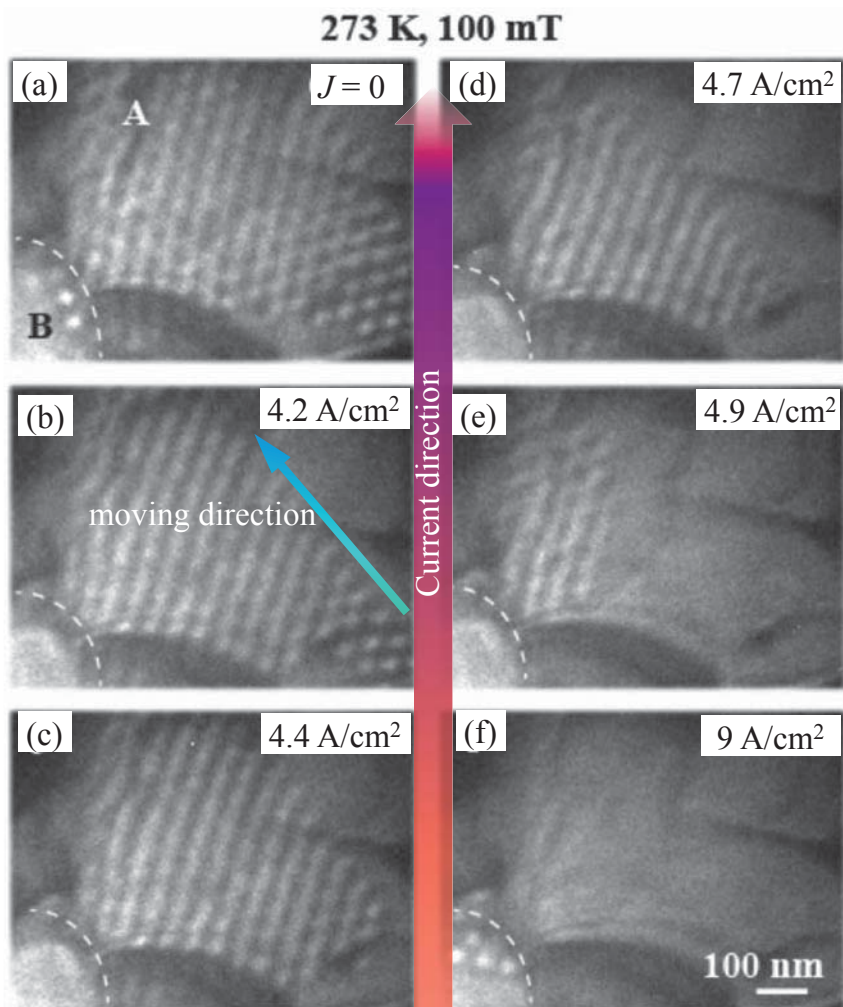
The snapshots of an *in-situ* LTEM movie for a motion of SkX in FeGe thin plate with dc current excitations.

as a function of the irradiation current density of the beam at 44 K near the helimagnetic transition temperature T_N (~ 50 K). Importantly, the rotation of SkX stops below a threshold of irradiation density.

Such unidirectional rotation induced by irradiated electron beam assumes that the local heating for the irradiated sample drives the TEM sample into the non-equilibrium state, e.g. the presence of temperature gradient shown in Fig. 7(a), leading to a Ratchet-like motion for skyrmions [24]. The Ratchet-like motion of SkX has been also demonstrated by numerical simulations based on the stochastic Landau-Lifshitz-Gilbert (LLG) equation, revealing that such unidirectional rotation can be induced by radiating spin current from the center via temperature gradient.

Summary

In addition to the observation of conventional magnetic configurations in FM materials, LTEM method is very effective in analyzing complex spin textures such as helical structure and vortex-like skyrmion, and is expected to contribute significantly to the science and future technology with use of "topological spin texture".

In this study, we have successfully done the LTEM observations of the Bloch-type magnetic skyrmions and their dynamics in chiral and FM thin-plate systems, by controlling the applied magnetic field, the electric current and the strength of the irradiated electron beam. We have found that 2D SkX can be stabilized in thin films and SkX can be driven by ultra-low electric current and thermal current, providing a basis for skyrmionics in future.

Acknowledgements

Fig. 7
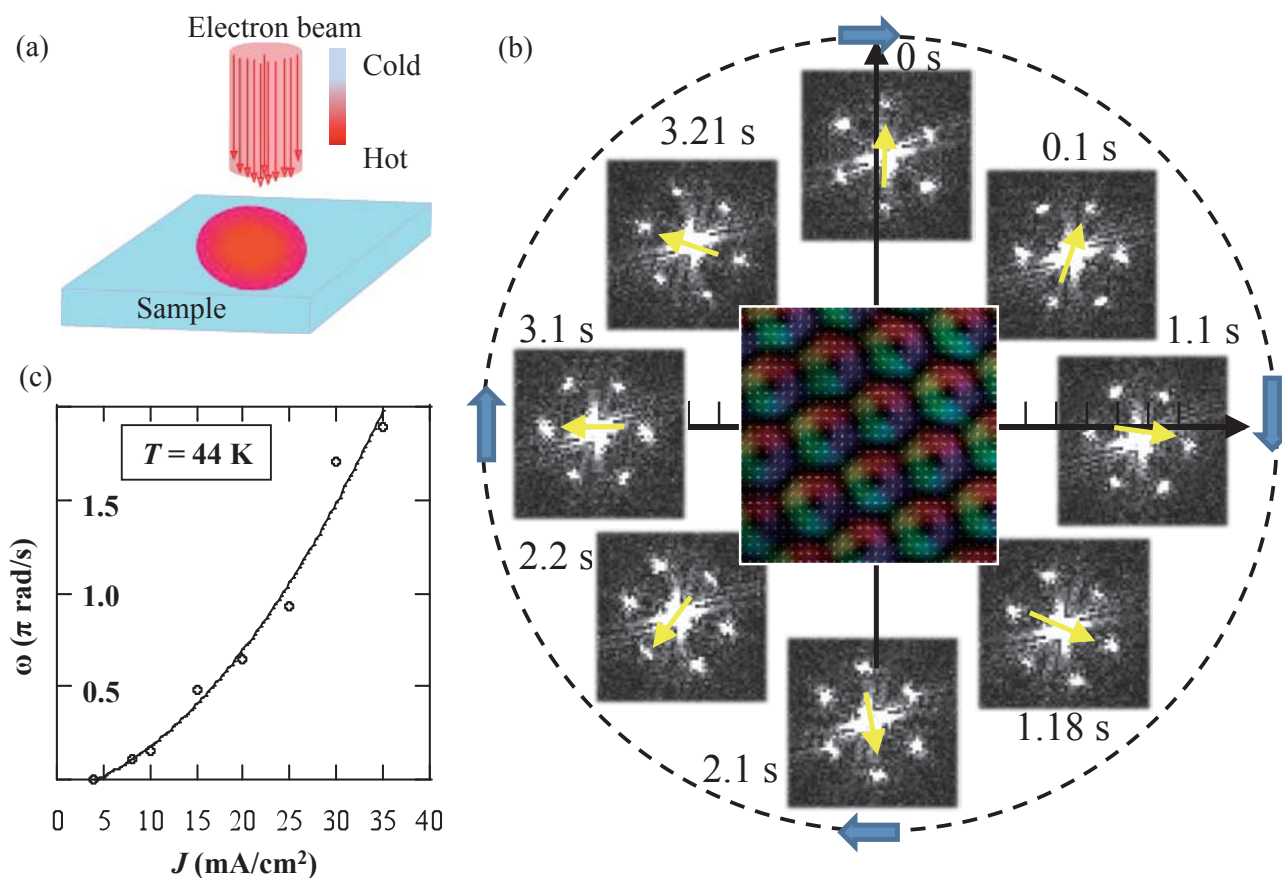
(a) The schematic of the thermal current induced by the electron beam. (b) The fast Fourier transforms (FFTs) of the SkX observed in Cu_2OSeO_3 under a normal magnetic field of 60 mT at 44 K in a time sequence. The central shows the magnetization textures for the SkX. (c) The rotating speed of SkX vs. the intensity of the incident electron beam.

References

[1] J.G. Bednorz and K.A. Muller, *Z. Phys. B* **64**, 189 (1986).
[2] Y. Tokura and N. Nagaosa, *Science* **288**, 462 (2000).
[3] M. Yamanouchi, D. Chiba, F. Matsukura and H. Ohno, *Nature* **428**, 539 (2004).
[4] K. Uchida, *et al., Nature* **455**, 778 (2008).
[5] A. Fert, V. Cros and J. Sampaio, *Nature Nanotech.* **8**, 152 (2013).
[6] N. Nagaosa and Y. Tokura, *Nature Nanotech.* **8**, 899 (2013).
[7] T. Skyrme, *Nuclear Physics* **31**, 556 (1962).
[8] S. Mühlbauer, *et al., Science* **323**, 915 (2009).
[9] X. Z. Yu, *et al., Nature* **465**, 901 (2010).
[10] W. Koshibae, Y. Kaneko, M. Kawasaki, N. Nagaosa and Y. Tokura, *Jpn. J. Appl. Phys.* **54**, 053001 (2015).
[11] X. Z. Yu, *et al., Nat. Mater.* **10**, 106 (2011).
[12] L. Reimer and K. Kohl, *Transmission Electron Microscopy* (Springer, 2008).
[13] X. Z. Yu, *et al., Phys. Rev. B* **91**, 054401 (2015).
[14] X. Z. Yu, *et al., Proc. Natl. Acad. Sci.* **109**, 8856 (2012).
[15] X. Z. Yu, *et al., Nat. Commun.* **5**:3198 (2014).
[16] I. Dzyaloshinsky, *J. Phys. Chem. Solids* **4**, 241 (1958).
[17] T. Moriya, *Phys. Rev.* **120**, 91 (1960).
[18] K. Shibata, *et al., Nature Nanotech.* **8**, 723 (2013).
[19] D. Morikawa, K. Shibata, N. Kanazawa, X. Z. Yu and Y. Tokura, *Phys. Rev. B* **88**, 024408 (2013).
[20] K. Ishizuka and B. Allman: *J. Electron Microsc.* **54**, 191 (2005).
[21] S. E. Barns and S. Maekawa, *Phys. Rev. Lett.* **95**, 107204 (2005).
[22] X. Z. Yu, *et al., Nature Commun.* **3**:988 (2012).
[23] S. Seki, X. Z. Yu, S. Ishiwata and Y. Tokura, *Science* **336**, 198 (2012).
[24] M. Mochizuki, *et al., Nat. Mater.* **13**, 241 (2014).

Quantitative ADF STEM for Catalyst Nanoparticle Metrology

Peter D Nellist[1], Lewys Jones[1], Katherine E MacArthur[1] and Dogan Ozkaya[2]

[1] University of Oxford, Department of Materials
[2] Johnson Matthey Technical Centre

A method to reconstruct the three-dimensional structure of catalyst nanoparticles from single projections is described. The aim is to develop a method by which statistically meaningful measurements of heterogeneous catalyst systems can be made and subsequently related to catalyst properties with goal of assisting with the rational design of new catalysts. A method for the careful calibration of annular dark-field STEM images is described. Use is made of scattering cross-sections to enable comparison with simulation to allow the number of atoms in atomic columns to be determined. Finally, an energy minimization method is used to finalise the three-dimensional structure.

Introduction

Annular dark-field (ADF) imaging in the scanning transmission electron microscope (STEM) is a powerful technique that provides images that are both relatively simple to interpret, due to their incoherent nature, and show strong atomic number, or Z-contrast due to the relatively high angles of scattering collected [1]. Although ADF STEM has been established as a key technique for atomic resolution imaging for more than 20 years [2, 3], it is only recently that there has been a significant effort to make use ADF images in a quantitative way to make physically meaningful measurements of the sample [4, 5]. A possible explanation for this is that the ADF signal is generated by a combination of elastic scattering and thermal diffuse scattering (TDS). Inversion of ADF intensities to sample measurements can only be achieved by matching of forward image simulations to the experimental data. There has been a recent emergence of increasingly accurate simulations [6, 7] due to improvements in computing power, making inversion of ADF images a viable proposition.

Heterogeneous catalysts often consist of nanoparticles of a (often precious) metal species dispersed on a carbon or ceramic support. Such catalysts play an invaluable role across a range of applications including, chemical synthesis, pollution control and hydrogen fuel-cells. Historically, the development of such catalysts has often been via empirical, trial and error methods, with rational design of catalysts being an important goal. Key to rational catalyst design is the ability to accurately characterize the catalyst materials. Because of the large atomic number differences between the metal nanoparticles and the support, ADF STEM has long played an important role in catalyst research [8] (see **Fig 1**). In this paper we describe how quantitative ADF STEM can play a role in determining the three-dimension (3D) structure of catalyst nanoparticles.

In considering how to use ADF STEM to quantitatively characterize nanoparticles, a number of important challenges arise:

(i) The nanoparticles are dispersed on an inherently three-dimensional powdered support, and therefore appear at many different heights in the sample. Any comparison between images and simulation must therefore be robust to uncertainties in defocus. Indeed, because of the difficulties in measuring many instrument parameters, for example the effective source size, we require a comparison to be as robust as possible to instrument parameters.

(ii) The particles and the support material are usually susceptible to damage in the electron beam. Both these effects can cause a particle to rotate or reconstruct under electron exposure. For this reason, we require that all the information about the particle can be retrieved from a single projection of the sample and does not require changing viewing directions that, for example, would be required by a tomographic reconstruction with the associated additional dose for focusing, etc.

(iii) To give a meaningful conclusion about the catalyst sample, a sufficiently large number of nanoparticles should be imaged to give statistically meaningful measurements. A sufficiently fast method for processing the experimental images and comparison with simulations is therefore required.

>> Parks Road, Oxford, OX1 3PH, UK | E-mail: peter.nellist@materials.ox.ac.uk

Here we explore how quantitative ADF STEM can be used for catalyst nanoparticle metrology, and in particular how the twin challenges of reconstructing 3D information of materials can be achieved alongside sufficiently high throughput to provide meaningful information. We start by describing the experimental method we have developed to provide the most parameter robust quantification before going on to discuss how the information provided can be used to provide 3D structures of nanoparticles.

Experimental method

Cross-sections for simulations matching

We wish to make the comparison between experiment and simulation as robust as possible to the many instrument parameters that play a role in high-resolution ADF STEM imaging. There will, however, still be a number of parameters that will need to be accurately known, and these can be identified by first describing our method for comparing simulation to experiment. Rather than relying on making a pixel-by-pixel match between an experimental image and a simulation, we prefer to make use of measured and computed scattering cross-sections. The use of cross-sections in ADF STEM imaging was proposed and implemented by Retsky in 1973 [9], but appears to have been little used since then.

Cross-sections are widely known and used in particle scattering experiments. In the context of ADF STEM, the crucial attribute is that the image can be treated as being *incoherent* [1]. Incoherent imaging means that the image, $I(\mathbf{r})$, can be treated as a convolution between the intensity of the illuminating STEM probe, $P(\mathbf{r})$, and some object function, $O(\mathbf{r})$, that represents the scattering to the ADF detector,

$$I(\mathbf{r}_0) = \int P(\mathbf{r}_0 - \mathbf{r}) O(\mathbf{r}) d\mathbf{r} \quad \cdots\cdots\cdots\cdots (1).$$

We next assume that in an aberration-corrected STEM instrument, the atomic columns in the image are well resolved, and that the intensity associated with a single atomic column can be completely integrated,

$$\int_{\substack{\mathbf{r}_0 \\ atomic \\ column}} I(\mathbf{r}_0) d\mathbf{r}_0 = \int_{\substack{\mathbf{r} \\ all \\ Space}} P(\mathbf{r}_0 - \mathbf{r}) O(\mathbf{r}) d\mathbf{r} d\mathbf{r}_0 \quad \cdots\cdots (2).$$

It is possible to perform the integral over $\mathbf{r}_0$ first in Eq. (2) which essentially leads to the integral over the complete probe intensity. A key step now is to calibrate the ADF image so that the intensity in each pixel of the ADF image represents the fraction of the incident beam that is scattered to the ADF detector when the probe is located at that pixel location. **Figure 2** shows such a calibrated image. It can be seen that the ADF STEM signal rises to around 10% of the incident beam for these imaging conditions. The implication of this type of intensity calibration is that the probe intensity expressed in Eq. (2) must then integrate to unity, leaving.

$$\int I(\mathbf{r}_0) d\mathbf{r}_0 = \int O(\mathbf{r}) d\mathbf{r} = \sigma \quad \cdots\cdots\cdots\cdots\cdots (3).$$

Equation (3) shows that we have derived a quantity, σ, which is independent of the form of the probe intensity. Furthermore, a dimensional analysis of the equations given above shows that the objection function, $O(\mathbf{r})$, is dimensionless, and that therefore σ has units of area leading to its description as a cross-section. Indeed, it can be shown that the value represented by σ, when multiplied by an illuminating current density, gives the total number of electrons scattered to the ADF detector. Typical values for σ, compared with cross-sections for EDX and EELS, are shown in **Table 1** which dramatically illustrates why ADF images can be formed at atomic resolution with much lower pixel dwell times than spectroscopic mapping. We note that the approach described above requires incoherent imaging in order

---
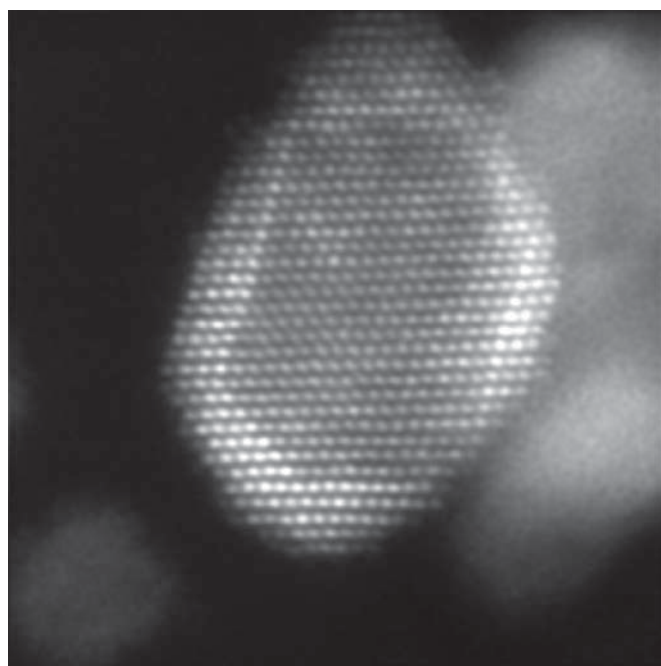
An ADF STEM image of a Pd core, Pt shell bimetallic nanoparticle demonstrating the sensitivity of ADF STEM imaging to thickness and composition changes in a nanoparticle. The image was recorded on the Oxford-JEOL JEM-2200MCO instrument. The particle is viewed along <110> and is approximately 5 nm in diameter in the horizontal direction in this figure.

to even be able to define a cross-section. Since it cannot be used for coherent imaging, such as HRTEM, perhaps explains why cross-sections have not be widely adopted previously in (S) TEM.

Cross-sections for ADF STEM can similarly be simulated using standard STEM simulation software. Because of the independence of the cross-section to the imaging parameters that control the probe shape, cross-sections provide an extremely robust metric for comparing experiment and simulations [10] (**Fig. 3**). The important parameters for cross-sections are the accelerating voltage and the detector angle and efficiency. We now go on to explore how those associated with the detector can be determined.

Calibration of the ADF detector

Clearly the most important parameter associated with the cross-section approach described above is the angular ranges over which scattering is detected by the ADF. Methods to measure this angle are usually based on calibrating the effective camera length of a camera in the STEM detector plane followed by observation of the shadow of the detector, though care must be taken with this approach to take into account the effect of any inactive liner tube in the centre of the detector.

Perhaps more problematic for ADF STEM imaging is the variation of efficiency of the ADF detector across its area [11]. Early approaches to quantitative ADF STEM simply made use of the average response of the ADF, and ignored variations

across the detector. The intensity of the scattering by the sample is, however, inhomogeneously distributed over the detector, and therefore variations in efficiency will be of significance. Experience shows that the detectors provided by JEOL on the JEM-ARM200CF instrument in Oxford are relatively flat compared to many others.

Of importance here is the method used to map the detector. A simple approach is to use the so-called STEM Align mode, in which the post-specimen optics are set to image the probe in the sample plane to the detector plane, along with significant magnification. Performing a STEM scan then effectively scans the probe image over the detector leading to a detector map. In this mode, the post-specimen optics are set differently to how they would be for STEM imaging, for which the post-specimen optics are effectively in diffraction mode and controlling camera length. This means that the outer reaches of the detector can be accessed without high-angle rays having passed through the specimen optics, as illustrated in **Fig. 4**(a). Since high angle rays are likely to be highly distorted due to residual aberrations, there is unlikely to be a linear relationship between the position in this type of detector map and scattering angle of the beam at the sample.

An alternative approach, that has long been established for dedicated STEM instruments and is now being implemented in modern (S)TEM instruments is the use of a parallel beam that is swept in angle at the sample plane (Fig. 4(b)). This can be set up by setting the condenser optics so that there is a beam cross-over in the front focal-plane of the objective lens. The objective

Fig. 2
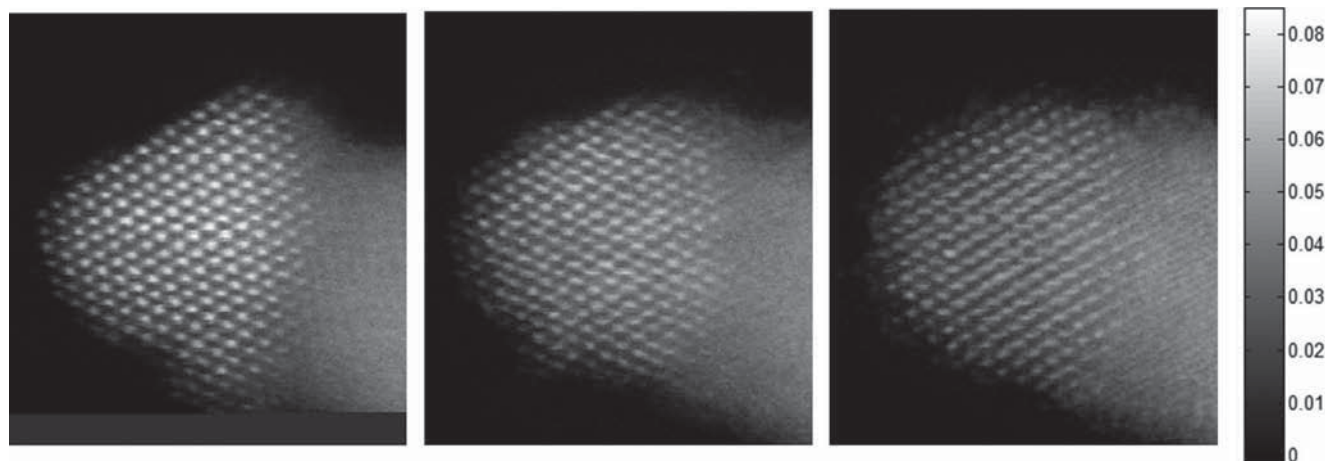
A series of images recorded from a Pt catalyst nanoparticle with the intensity calibrated as the scattered fraction of the incident beam. The images were recorded using a JEOL JEM-ARM200CF instrument. The region with the lattice resolved as viewed along the <110> direction is about 3.5 nm in diameter.

Table 1

| Metal	EDX (b)	EELS (kb)	ADF (Mb)
Pt	5.42	0.323	1.12
Pd	7.41	-	0.515
Co	2.89	1.334	0.204

A comparison of typical cross-sections per atom for ADF, EELS and EDX detection in a STEM instrument. The unit used is the barn (b) = 10^{-28} m^2. Note that the EELS cross sections were calculated using Hartree-Slater models (M edge, 100 eV integration window for Pt and L edge, 40 eV integration window for Co) for comparison purposes.

lens then acts to form a parallel beam, and this beam is swept in angle as the cross-over is scanned across the front focal plane. The maps produced (**Fig. 5**) then accurately represent the mapping of scattering angle to the detector, and distortions or angular cut-offs are clearly apparent.

Comparison with simulations

Accurate ADF STEM image simulations are now well-established [6, 7] and their agreement with experiment demonstrated [12, 13]. For the work presented here, we make use of the µSTEM code developed at the University of Melbourne based on the principle of the quantum excitation of phonons [6]. The calculations can give simulated images calibrated in units

Fig. 3
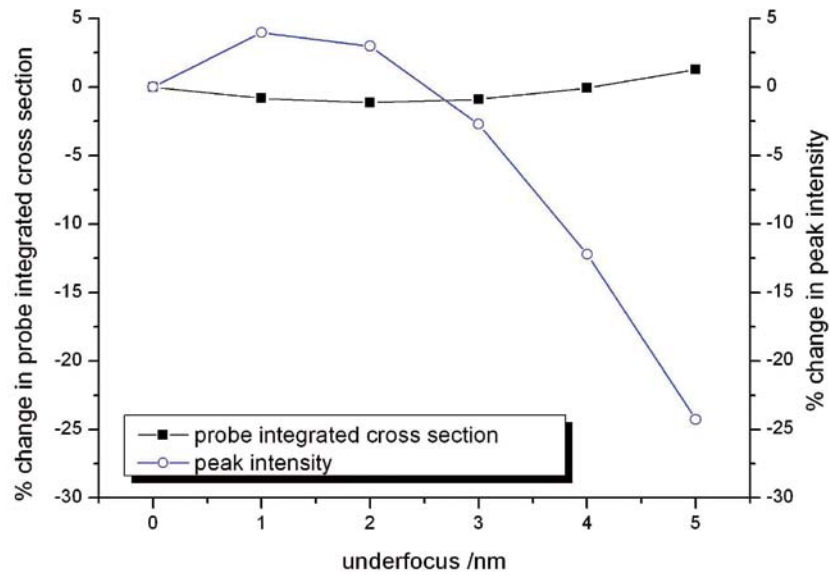
The fractional change in the cross-section for a 5 nm thick Pd nanocrystal as a function of probe defocus compared to the fractional change of peak intensity. The robustness of the cross-section to defocus error can be seen. Taken from Reference [10]. Copyright 2013 Elsevier.

Fig. 4
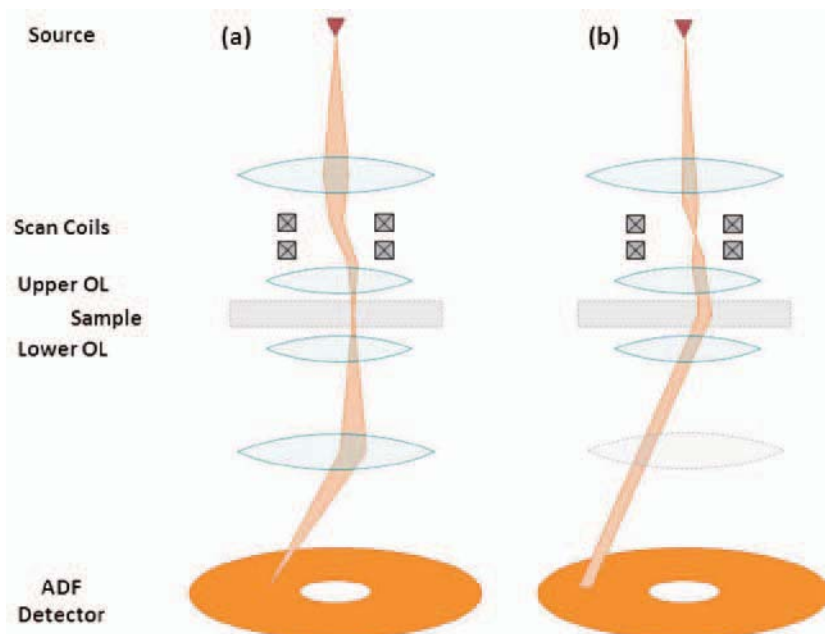
Schematic ray diagrams showing two approaches to mapping the ADF detector. (a) The probe is imaged by post-specimen optics to the detector, but this approach does not measure how high-angle rays are mapped to the detector through the post-specimen optics. (b) Moving a beam cross-over to the front focal-plane of the objective lens creates a parallel pencil-beam that is scanned in angle allowing the mapping of specific scattering angles to the appropriate detector response.

of fractional probe current scattered to the detector, and so from the simulated images, libraries of calculated cross-sections for different column thicknesses and compositions can be generated.

A question that does arise at this point is how to deal with the variation in response of the ADF detector. Ideally, the library of cross-sections would be generated from simulations that take into account the variation in detector response. The frozen phonon approach to STEM imaging simulation does calculate a map of intensity in the STEM detector plane that is then integrated over, and at that point variations in efficiency could be taken into account, as is possible in the STEMsim package [7]. Currently only variations in scattering angle are included in this way. Figure 5 shows that the detector is also has strong variations azimuthally, but taking these into account would require careful calibration of the rotation of the detector relative to the sample, and this rotation can also depend on lens excitations in the column.

An alternative approach is to make an approximation to the angular dependence of scattering and to use this to renormalize the data taking into account variations in detector sensitivity [14].

At this point we should also point out that atom counting need not require an accurate comparison to simulations. Because atoms are discrete entities, and that atomic columns in a nanoparticle must contain a whole number of atoms, the statistical distribution of measured cross-sections should show some modality, ie measurements should cluster around a set of discrete values. By using a Gaussian mixture model combined with a classification cost function, Van Aert [15] have shown that accurate atom counting in a column can be achieved. This approach requires a sufficient number of atomic columns to provide sufficient samples, along with a small variance in cross-section values for columns of the same number of atoms, to

allow modality to be detected. Such variances in measurements may occur simply because of Poisson counting statistics, or because of scan distortions leading to local variations in effective magnification. The latter underlines the need for stable instruments and scans. In situations where either the necessary conditions described above are satisfied, for example a nanoparticle that is too small and contains too few columns to build up enough statistics to identify the modality, then matching cross-sections to simulations is necessary. In counterbalance to this, a statistical approach is robust to errors in detector calibration, for example.

Results and Discussion

Using the method outlined above, we can now convert single images of nanoparticles into maps showing the number of atoms in each column (**Fig. 6**). As a final step to generating full 3D structures of catalytic nanoparticles, we must decide on the z-position of each column relative to the other columns in the image of the nanoparticle. The ADF STEM imaging approach is insensitive to this, and therefore we have two options: either to use a tilt tomography type approach to 3D reconstruction, perhaps making use of discrete tomography [16], or to use prior information. Our constraint that we must only use one image, as described in the introduction, precludes the tomographic approach, so we must seek a reconstruction method based on prior information.

In most cases, we know the bulk crystal structure of the metal nanoparticles in the catalyst sample. For example, Fig. 2 shows Pt nanoparticles. The crystal structure of Pt is cubic close-packed (ccp), and it only infrequently shows twinned domains when pure. We can therefore assume that the atoms

---

Fig. 5
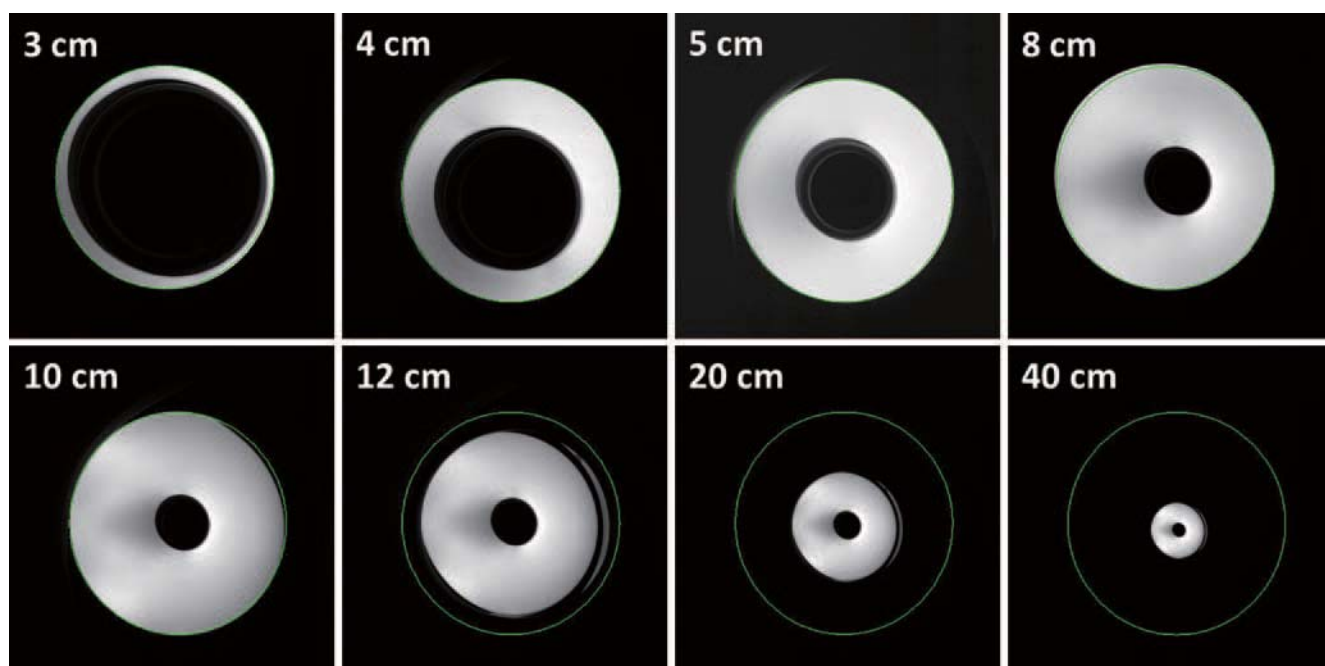
A detector map produced using the method shown in Fig. 4(b) on a JEOL JEM-ARM200CF instrument. The response of the detector shown here is relatively flat compared to many available detectors (see Ref. [10] for a comparison of different detectors). This method reveals that there is an outer cut-off in scattering angle that is not associated with the detector but is imposed elsewhere in the instrument.

in the nanoparticle will sit on ccp sites. In this assumption we are therefore choosing to neglect the effects of strain, the measurement of which is the subject of future work.

The remaining degree of freedom, which we are not able to determine from the experimental data, is the height of each column relative to its neighbours. Here, we now assume that the particle is in a minimum energy configuration. For any individual particle it is, of course, not possible to conclusively state that it has found such a configuration. One aim of using a single particle image, however, was to enable a larger number of particles to be analysed and to thereby improve statistics. Statistically derived values, such as atom coordination numbers, are therefore likely to average over particles that have a range of

non-equilibrium structures.

Because the particles will contain many columns, there is still a large parameter space to explore in order to find the minimum energy configuration. The strategy explained by Jones et al. [17] starts by placing each column with its midpoint on a plane that is common to all columns in the particle. This creates a particle that is effectively symmetric about this midplane. To further refine the particle structure, a Monte Carlo-based energy minimization is used.

Resulting structures from 3 frames of a sequence of images are shown in **Fig. 7**. A detailed discussion about the changes observed is presented in Jones et al. [17]. Briefly, it can be seen from Fig. 7 that the particle is becoming progressively less

---

Fig. 6
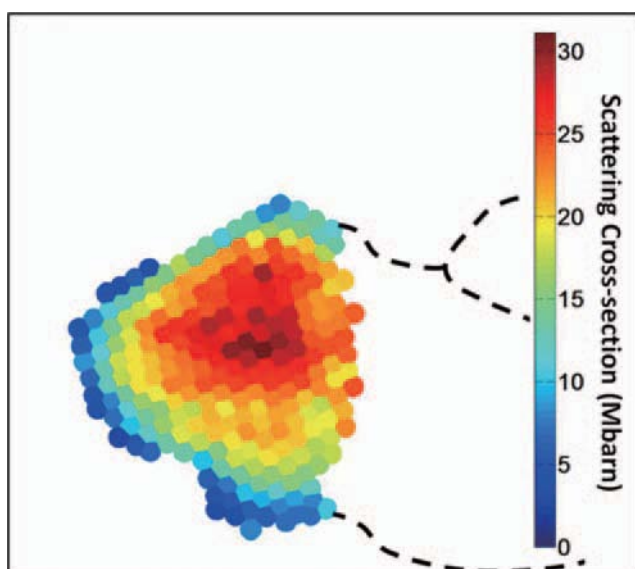
Maps of scattering cross-section for each column of the nanoparticle shown in Fig 2(a). Using the simulations, the cross-sections can be relatively easily converted to the number of atoms in a column.

Fig. 7
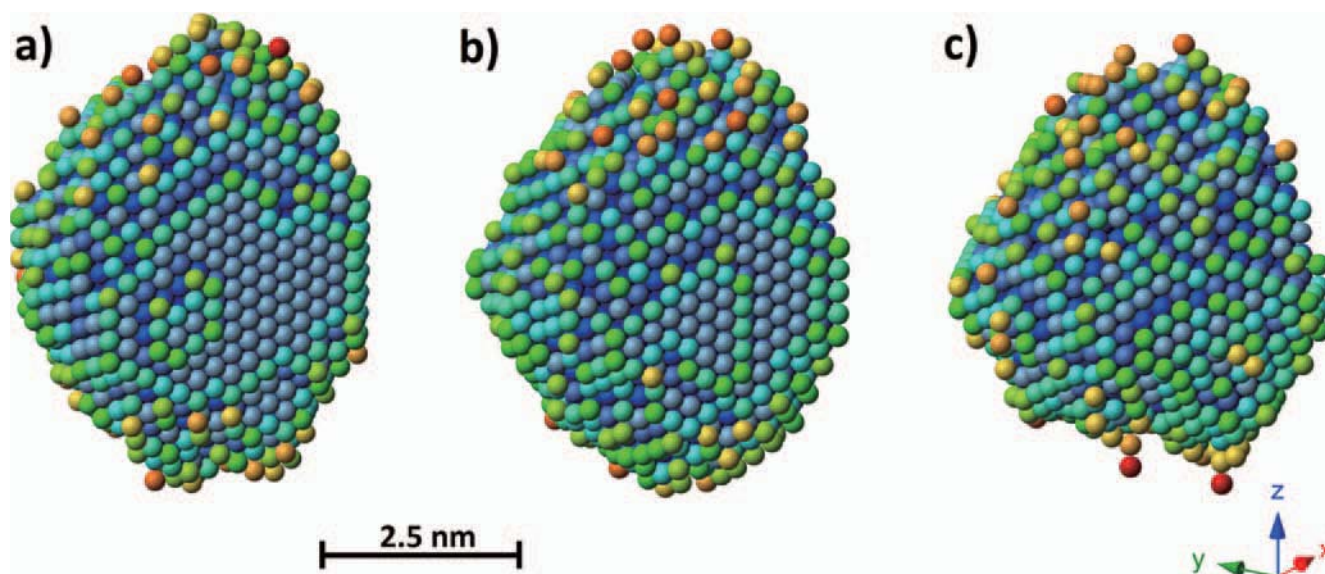
Reconstructed 3D models of the particles shown in Fig. 2. Reprinted with permission from Reference [17]. Copyright 2014 American Chemical Society.

faceted and increasingly spherical in nature. From the three-dimensional reconstruction, useful measurements such as the distribution of atom coordination numbers can be extracted.

Conclusion

In summary, we have described a method by which the 3D structure of nanoparticles can be reconstructed from single ADF STEM images without using multiple exposure methods such as tilt-series tomography. Careful calibration of the ADF intensities, combined with the use of cross-sections as a robust metric to allow comparison with simulations, allows the number of atoms in a column to be determined. Using this measurement, the 3D structure of the nanoparticle is then determined making use of prior information.

The approach taken here is somewhat different approach to that often taken with electron microscopy. It is often assumed that the microscope must provide the maximum amount of information possible, and interpretation of the data should make use of the minimum amount of prior information. The aim of delivering atomic resolution tilt-series tomography is an example of such an approach. The aim of this article is not to criticize this approach, but to demonstrate an alternative approach where the maximum use of prior information is made to minimize the amount of microscopy required. This approach helps to minimize the electron exposure of the sample, and allows many nanoparticles to be analyzed leading to more meaningful statistics. In the case of the study of supported heterogeneous catalyst systems, we believe that the latter approach is more meaningful in the quest to relate the distribution of catalyst nanoparticle structures to catalytic activity.

It must be appreciated that there is a level of risk associated with the approach presented here. The quality of the data now depends more critically on the quality of the prior information. For example, it may be unreasonable to assume that the particles are on average at thermal equilibrium, and their structures may be controlled by kinetics. Future work may include more detailed analysis of a sub-set of nanoparticles to validate the prior information which can then be applied to a wider ensemble.

Acknowledgments

References

[1] P.D. Nellist, S.J. Pennycook, The Principles and Interpretation of Annular Dark-Field Z-Contrast Imaging, *Advances in Imaging and Electron Physics*, **113** (2000) 148-203.

[2] S.J. Pennycook, D.E. Jesson, High-Resolution Incoherent Imaging of Crystals, *Physical Review Letters*, **64** (1990) 938-941.

[3] D.H. Shin, E.J. Kirkland, J. Silcox, Annular dark field electron microscope images with better than 2Å resolution at 100kV, *Applied Physics Letters*, **55** (1989) 2456-2458.

[4] J.M. LeBeau, S.D. Findlay, L.J. Allen, S. Stemmer, Quantitative atomic resolution scanning transmission electron microscopy, *Physical Review Letters*, **100** (2008) 206101.

[5] C. Dwyer, C. Maunders, C.L. Zheng, M. Weyland, P.C. Tiemeijer, J. Etheridge, Sub-0.1 nm-resolution quantitative scanning transmission electron microscopy without adjustable parameters, *Applied Physics Letters*, **100** (2012) 191915.

[6] B.D. Forbes, A.V. Martin, S.D. Findlay, A.J. D'Alfonso, L.J. Allen, Quantum mechanical model for phonon excitation in electron diffraction and imaging using a Born-Oppenheimer approximation, *Physical Review* **B, 82** (2010) 104103.

[7] A. Rosenauer, M. Schowalter, STEMSIM—a New Software Tool for Simulation of STEM HAADF Z-Contrast Imaging, in: A.G. Cullis, P.A. Midgley (Eds.) Microscopy of Semiconducting Materials 2007, Springer Netherlands, 2008, pp. 170-172.

[8] A. Howie, L.D. Marks, S.J. Pennycook, New Imaging Methods For Catalyst Particles, *Ultramicroscopy*, **8** (1982) 163-174.

[9] M. Retsky, Observed Single Atom Elastic Cross Sections in a Scanning Electron Microscope, *Optik*, **41** (1974) 127-142.

[10] H. E, K.E. MacArthur, T.J. Pennycook, E. Okunishi, A.J. D'Alfonso, N.R. Lugg, L.J. Allen, P.D. Nellist, Probe integrated scattering cross sections in the analysis of atomic resolution HAADF STEM images, *Ultramicroscopy*, **133** (2013) 109-119.

[11] K.E. MacArthur, L.B. Jones, P.D. Nellist, How flat is your detector? Non-uniform annular detector sensitivity in STEM quantification, Journal of Physics: Conference Series, 522 (2014) 012018.

[12] J.M. LeBeau, S.D. Findlay, L.J. Allen, S. Stemmer, Standardless Atom Counting in Scanning Transmission Electron Microscopy, *Nano Letters*, **10** (2010) 4405-4408.

[13] J.M. LeBeau, S. Stemmer, Experimental quantification of annular dark-field images in scanning transmission electron microscopy, *Ultramicroscopy*, **108** (2008) 1653-1658.

[14] G.T. Martinez, L. Jones, A. De Backer, A. Beche, J. Verbeeck, S. Van Aert, P.D. Nellist, Quantitative STEM normalisation: the importance of the electron flux, *Ultramicroscopy*, to be submitted (2015).

[15] S. Van Aert, A. De Backer, G.T. Martinez, B. Goris, S. Bals, G. Van Tendeloo, A. Rosenauer, Procedure to count atoms with trustworthy single-atom sensitivity, *Physical Review* **B, 87** (2013) 064107.

[16] S. Van Aert, K.J. Batenburg, M.D. Rossell, R. Erni, G. Van Tendeloo, Three-dimensional atomic imaging of crystalline nanoparticles, *Nature*, **470** (2011) 374-377.

[17] L. Jones, K.E. MacArthur, V.T. Fauske, A.T.J. van Helvoort, P.D. Nellist, Rapid Estimation of Catalyst Nanoparticle Morphology and Atomic-Coordination by High-Resolution Z-Contrast Electron Microscopy, *Nano Letters*, **14** (2014) 6336-6341.

Application of Atomic-Resolution Energy-Dispersive X-ray Spectroscopy to the Study of Structures of Decagonal Quasicrystals

Kenji Hiraga[1] and Akira Yasuhara[2]

[1] Institute for Materials Research, Tohoku University
[2] EM Business Unit, JEOL Ltd.

We give an overview of recent studies for chemical ordering in Al-Co-Ni crystalline phases related to Al-Co-Ni decagonal quasicrystals (DQCs), and Al-Mn-Pd DQC, by atomic-resolution energy-dispersive X-ray spectroscopy (EDS) combined with Cs-corrected scanning transmission electron microscopy (STEM). In order to avoid the electron damage by the strong electron beam in a field-emission gun installed to a Cs-corrected STEM and long exposure times required to obtain high-resolution EDS maps, atomic-resolution EDS maps were obtained by integrating many sets of EDS data taken from fresh areas at each time by shifting the sample so that the same structure unit is always placed at the definite position on the STEM monitor. On the observed EDS maps, Co and Ni atomic positions in the Al-Co-Ni phases, and Mn- and Pd-enriched positions in the Al-Mn-Pd DQC can be clearly detected.

Introduction

The appearance of new experiment techniques or ones with the performance conspicuously improved sometimes overturns the ideas and models proposed from conventional methods from the root. Modern spherical aberration (Cs)-corrected scanning transmission electron microscopes (Cs-corrected STEM), which have an enough resolution to represent individual atoms as separate bright or dark dots in observed STEM images taken with the incident beam parallel to the periodic axis of decagonal quasicrystals (DQCs), have driven us re-examinations of Al-transition-metal (TM) DQCs and crystalline approximants by a full use of STEM with high-angle annular dark-field (HAADF) and annular bright-field (ABF) techniques [1-8]. As a result, we have produced new structural models formed by bond-orientational ordered (BOO) arrangements of TM atoms, as opposed to the cluster-based models, which have been widely accepted for a long time, characterized as BOO arrangements of large clusters, for example, with 2 nm in diameter [9-11]. Also, the recent development of an X-ray detector together with the strong electron beam of a field-emission gun (FEG) installed to a Cs-corrected STEM has led to the opportunity to study atomic arrangements under which the kind of atoms was classified, by atomic-resolution energy-dispersive X-ray spectroscopy (EDS) [12]. Thus, the atomic-resolution EDS combined to STEM observations certainly gives us new and valuable information about the structures of DQCs. However, the atomic-resolution EDS method is difficult to apply to most materials, which are easily damaged by the strong electron beam in the FEG microscopes and the long exposure times required to obtain high-resolution EDS maps. In order to avoid the electron damage, we have tried to obtain high-resolution EDS maps by integrating many sets of EDS data taken from fresh areas at each time by shifting the sample so that the same structure unit is always placed at the difinite position on the STEM monitor [13-15]. This technique can apply to most of materials and is a new way with a possibility to get valuable information on crystal structures, which is difficult to be obtained by conventional methods. In this paper, we give an overview of our recent results of the atomic-resolution EDS obtained by the special technique for two Al-Co-Ni crystalline approximants [13, 14] and Al-Pd-Mn DQC [15]. It should be noticed that structure models mentioned in the present paper are slightly different from those in the previous papers [13-15]. In particular, arrangements of Al atoms are not mentioned at all in this paper, because of paying attention to chemical ordering of Co and Ni atoms in the Al-Co-Ni crystalline phases, and Mn and Pd atoms in the Al-Mn-Pd DQC.

Experimental procedures

All STEM images shown in this paper are original ones

〉〉 2-1-1 Katahira, Aoba-ku, Sendai, 980-8557, Japan | E-mail: hiraga@imr.tohoku.ac.jp

without any processing, taken with the incident beam parallel to pseudo-tenfold rotational axes for crystalline approximates or the periodic axis for DQC using a *Cs*-corrected STEM (JEM-ARM200F). EDS maps were taken with a newly developed silicon drift detector (SDD), installed on the JEM-ARM200F STEM, and the EDS maps shown in this paper were obtained by the integration of 60 data-sets for the two Al-Co-Ni crystalline phases [13, 14], 31 data-sets for the Al₃ (Mn, Pd) and 34 data-sets for the Al-Mn-Pd DQC [15], taken from fresh areas by shifting the sample each time so that an unit cell or a structure unit is placed at the same position on the STEM monitor.

Two Al-Co-Ni crystalline approximants related to Al-Co-Ni DQCs [13, 14]

Six types of DQCs and some crystalline approximants have been found in Al-Co-Ni alloys with different Ni/Co composition ratios from 8 to 25.5 at%Co and from 20 to 5 at%Ni on a nearly constant Al content from 70 to 72 at% [16-20], and so the stability of these DQCs and crystalline approximants has been considered to be affected by chemical ordering of Co and Ni. However, the study of the chemical ordering of Co and Ni in the Al-Co-Ni DQCs and their approximants has never been performed, because it has been difficult, if not impossible, to distinguish between neighboring elements Co and Ni, by electron microscopy and X-ray diffraction. Here, we report on the chemical ordering of Co and Ni in two crystalline phases in $Al_{71.5}Co_{16}Ni_{12.5}$, and $Al_{72.5}Co_{20}Ni_{7.5}$ alloys, which are called the PD_{3c} [19, 20] and W-(AlCoNi) phases [21], respectively. The W-(AlNiCo) crystalline phase is an important approximant for understanding the structures of Al-Co-Ni DQCs formed with four quasiperiodic planes along the periodic axis. The structure of the W-(AlCoNi) phase was determined by single-crystal X-ray diffraction, but it was impossible to reveal the ordered arrangement of Co and Ni atoms in the determined structure [21]. On the other hand, the PD_{3c} phase is an approximant closely related to Al-Co-Ni DQCs formed with two quasiperiodic planes along the periodic axis, and its structure was determined by HAADF- and ABF-STEM observations [13].

Figure 1 shows an HAADF-STEM image (a) of the W-(AlCoNi) phase in an $Al_{72.5}Co_{20}Ni_{7.5}$ alloy annealed at 900 °C for 280 h, taken with the incident beam parallel to the *b*-axis (pseudo-tenfold rotational axis), and arrangements of TM atoms and mixed sites (MSs) of Al and TM atoms in the W-(AlCoNi) structure (b, c), which were derived from the arrangement and intensity of bright dots in (a) on the basis of the structure model determined from single-crystal X-ray


Fig. 1
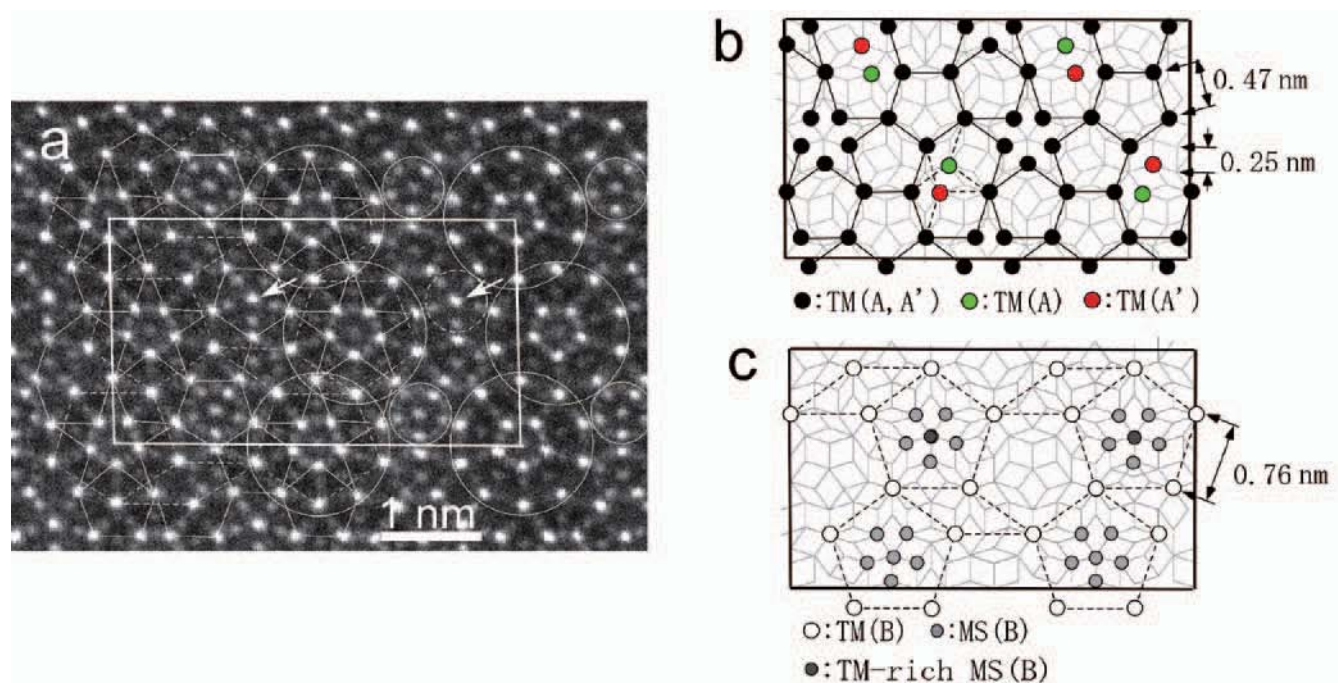
HAADF-STEM image (a) of the W-(AlCoNi) phase and arrangements of TM atoms and MSs in the A (A') and B planes (b, c) of the W-(AlCoNi) crystalline phase. Bright dots located at vertices of pentagonal tilings with bond-lengths of 0.47 and 0.76 nm in (a) correspond to TM atoms on the A (A') and B planes, respectively, as shown in (b) and (d). An arrangement of the TM atoms indicated by green and red circles on the A and A' planes, respectively, produces the structure consisting of four layers in the W-(AlCoNi). The 1.2 nm clusters indicated by lar ge circles in the right region of (a) are formed by TM atoms at vertices of a star-shaped pentagonal tile with an edge-length of 0.47 nm in (b) and pentagonal tile with an edge-length of 0.76 nm in (c). Two types of pentagonal MSs with a central TM-rich and TM-poor MS, indicated by small circles with broken and solid lines, respectively, in the right region of (a) are placed in upward pentagonal tiles in the B plane (c). The TM atoms and MSs on the A and B planes are located at vertices of rhombic Penrose tilling with a bond-length of 0.25 nm. The deformed rectangle of the unit cell in (a) results from the sample drift during beam scanning.

diffraction [21]. In the HAADF-STEM image with the contrast being proportional to Z^2 (Z: atomic number) [22], visible bright dots are considered to correspond to projected positions of TM atoms and MSs, whereas some Al atom positions are observed as faint bright dots. The structure of the W-(AlCoNi) phase, which has the space group of Cm (No.8) and lattice parameters of $a = 3.9668$ nm, $b = 0.8158$ nm and $c = 2.3392$ nm, can be described as a layer structure perpendicular to the b-axis, consisting of four layers of ABA'B stacking, but in the present paper it is mentioned as a two layer AB stacking, because of a small difference between arrangements of TM atoms on the A and A' planes, as shown in Fig.1(b). Clearly visible bright dots located at vertices of two types of pentagonal tilings with bond-lengths of 0.47 nm and 0.76 nm, which are indicated by solid and broken lines, respectively, in the left part of Fig. 1(a), correspond to TM atoms on the A and B planes, respectively, as can be seen in Figs. 1(b) and 1(c). In an arrangement of the bright dots in Fig. 1(a), one can recognize clusters formed by ten bright dots surrounding five dots with pentagonal symmetry, as indicated by large circles in the right part of Fig. 1(a). The cluster, which is formed by TM atoms located at the vertices of a star-shaped pentagon with an edge-length of 0.47 nm on the A plane and at the vertices of a pentagon with an edge-length of 0.76 nm on the B plane, is a common structural unit in some

Al-TM DQCs [1, 2, 4], and is called an 1.2 nm cluster with a diameter of 1.2 nm. The 1.2 nm clusters are located at the lattice points of a rhombic lattice formed by the periodic array of acute rhombuses with an edge-length of 2 nm. It should be noted that pentagonal arrangements of bright dots around the centers of all 1.2 nm clusters have the same orientation. Also, pentagonal arrangements of relatively weak dots, which correspond to MSs on the B plane, are observed in upward pentagonal tiles with an edge-length of 0.76 nm, and the pentagonal MSs are divided into two types by intensity distributions of bright dots, i.e. with strong and weak bright dots of central MSs, as indicated by small circles of broken and solid lines in the right part of Fig. 1(a), respectively. Those MSs are hereafter called pentagonal MSs with a central TM-rich MS and TM-poor MS, respectively. It should be noted that the structure of the two types of pentagonal MSs in Fig. 1(c) are different from that determined from single-crystal X-ray diffraction [21]. The TM atoms and MSs on the A and B planes are exactly located at vertices of Penrose rhombic tiling with a bond-length of 0.25 nm.

Figure 2 shows an HAADF-STEM image (a), atomic-resolution EDS color maps (b, c) of the W-(AlCoNi) phase, and a superimposed map (c) of (b) and (c). In Figs. 2(a) and 2(d), the 1.2 nm clusters are drawn by large circles, and pentagonal MSs with a central TM-poor MS are indicated by small circles.

Fig. 2
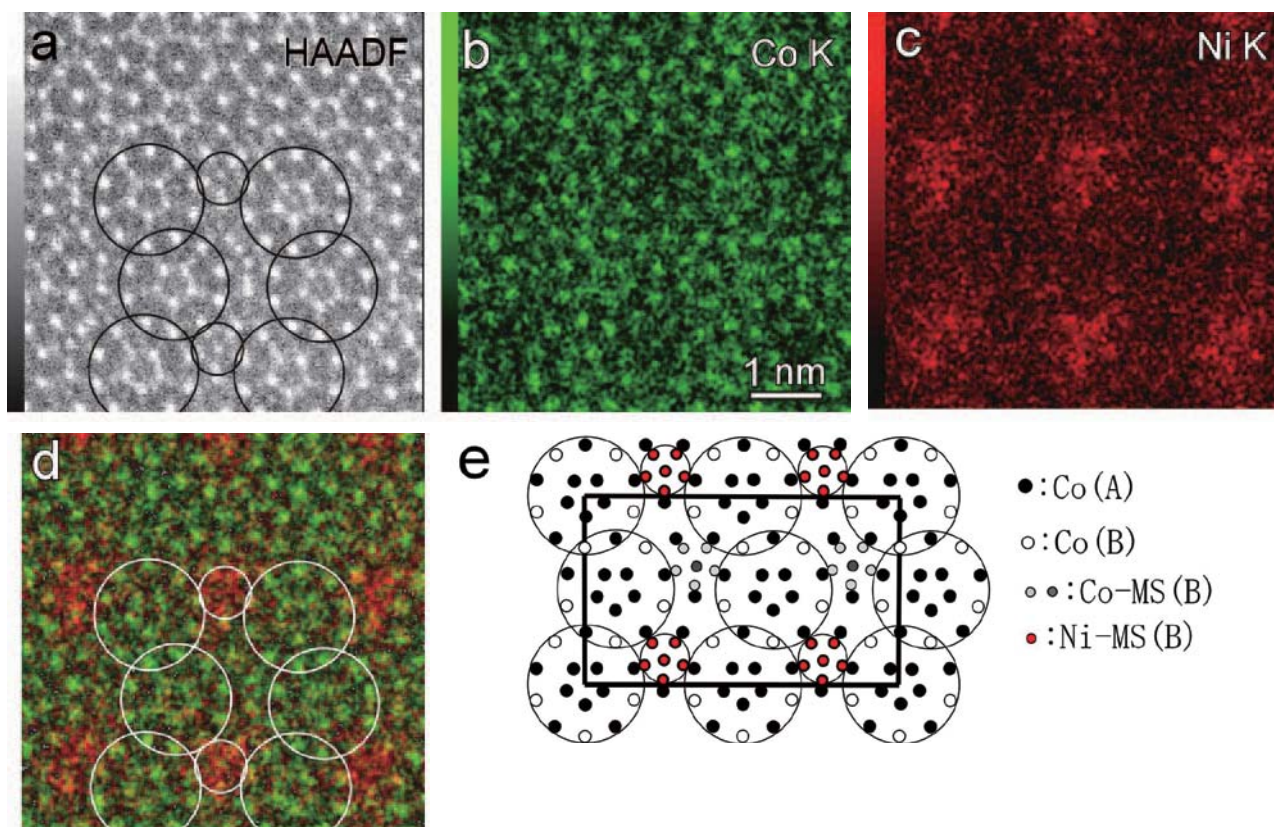
HAADF-STEM image (a), atomic-resolution EDS color maps (b, c) of the W-(AlCoNi) phase, and (d); the superimposed image of the two maps of (b) and (c). The 1.2 nm clusters and pentagonal MSs with central TM-poor MS are indicated by large and small circles, respectively. (c) and (d) show that Ni is enriched in the pentagonal MSs with a central TM-poor MS, as shown in (e).

Figure 2(d) shows that the TM atoms in the 1.2 nm cluster and pentagonal MSs with a central TM-rich MS are Co atoms (green), and the pentagonal MSs with a central TM-poor MS are occupied by Ni atoms (red).

The structure of the PD_{3c} phase in an $Al_{71.5}Co_{16}Ni_{12.5}$ alloy annealed at 900 °C for 120 h was determined from the HAADF- and ABF-STEM observations [13]. **Figure 3** shows an HAADF-STEM image of the PD_{3c} phase, taken with the incident beam parallel to the *b*-axis (pseudo-tenfold axis), and arrangements of TM atoms and MSs in the PD_{3c} structure. The crystalline phase has an orthorhombic unit cell with lattice parameters *a*=5.2 nm, *b*=0.4 nm and *c*=3.7 nm, and its structure is formed by two planes with A and B stacking along the *b*-axis. Thus, it can be concluded that the bright dots located at vertices of two types of pentagonal tilings with a bond-length of 0.76 nm, indicated by solid and broken lines in the left part of Fig. 3(a) correspond to the TM atoms in the A and B planes, respectively, as shown in Figs. 3(b) and 3(c). Also, pentagonal MSs are observed in upward pentagonal tiles with solid lines and downward ones with broken lines in Fig. 3(a) are located on the A and B planes, as shown in Figs. 3(b) and 3(c), respectively. The 1.2 nm clusters, which are indicated by large circles in the right part of Fig. 3(a), are located at lattice points of a rhombic lattice formed by the periodic array of obtuse and acute rhombuses with an

edge-length of 2 nm. It should be noticed that two types of the 1.2 nm clusters with opposite orientations of the pentagonal arrangements of bright dots at their centers are arranged in an ordered manner in such a way that two clusters connected by a bond of 2 nm are always different.

Figure 4 shows an HAADF-STEM image (a), atomic-resolution EDS color maps of (b, c) of the PD3c approximant, and a superimposed map (d) of (b) and (c). In Figs. 4(a) and 4(d), the 1.2 nm clusters are drawn by circles. Figure 4(d) clearly shows the Co- and Ni-rich areas, i.e. the TM atoms arranged with the 0.76 nm pentagonal tiling are Co atoms, and pentagonal MSs located in pentagonal tiles are occupied by Ni atoms. Thus, it can be concluded that the chemical ordering of Co and Ni occurs between the TM sites arranged with the 0.76 nm pentagonal tiling and pentagonal MSs in the A and B planes, as shown in Figs. 4(e) and 4(f).

Al$_3$Mn-type Al$_3$(Mn, Pd) crystalline approximant and Al-Mn-Pd DQC [15]

An Al-Mn-Pd DQC with a 1.2 nm periodicity along the periodic axis has been found as a stable phase in a wide composition region around $Al_{70}Mn_{10}Pd_{20}$ [23, 24]. The structure of the Al-Mn-Pd DQC can be characterized
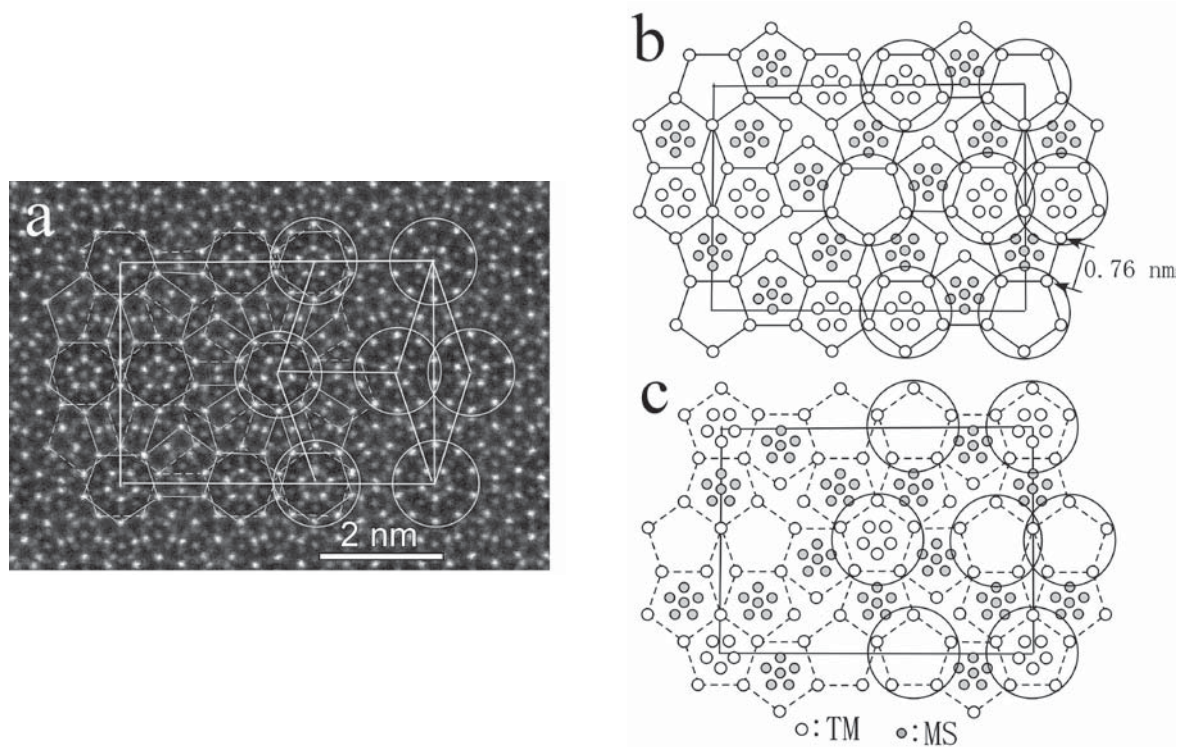
HAADF-STEM image (a) of the PD_{3c} approximant and arrangements of TM atoms and MSs on the A (b) and B (c) planes, derived from (a). Strong bright dots corresponding to projected positions of TM atoms are located at vertices of two types of 0.76 nm pentagonal tiling, as can be seen in the left region of (a). The 1.2 nm cluster indicated by circles in the right region of (a) is located at lattice points of a rhombic lattice formed by the periodic array of obtuse and acute rhombuses with an edge-length of 2 nm. It should be noticed that two types of the 1.2 nm clusters with opposite orientations of the pentagonal arrangements of bright dots at their centers are arranged in an ordered manner in such way that two clusters connected by a bond of 2 nm are always different.

by a BOO arrangement of columnar atom clusters with a decagonal section of 2 nm in diameter (hereafter referred to as decagonal cluster) from high-resolution transmission electron microscopic observations [23-25]. Further, it has been found that the formation of the decagonal clusters occurs in the Al_3Mn crystalline matrix by annealing at 800 °C, and that a re-arrangement of the decagonal clusters leads to the BOO arrangement of decagonal clusters in the DCQ [26]. Therefore, the Al_3Mn phase is considered to be an important crystalline approximant related to the Al-Mn-Pd DQC, and consequently the atomic arrangement of the Al-Mn-Pd DQC has been studied using the Al_3Mn structure model [27]. Additionally, the positions of Pd atoms within the crystal, which are considered to have a strong effect on the stability of the DCQ phase, were determined by X-ray analysis of an Al_3Mn-type $Al_3(Mn, Pd)$ crystal with a composition of approximately $Al_{75}Mn_{20}Pd_5$ [28. 29]. In this paper, HAADF-STEM images and EDS maps of the $Al_3(Mn, Pd)$ crystalline phase and Al-Mn-Pd DQC, which were obtained in an as-melted and annealed (at 800 °C for 3 h) $Al_{70}Mn_{20}Pd_{10}$ alloys, respectively, will be presented.

Figure 5 shows a structural model of the $Al_3(Mn, Pd)$ crystal, which was determined by X-ray diffraction [28, 29]. The $Al_3(Mn, Pd)$ structure, which has the space group of *Pnma* and the lattice parameters of $a = 1.4727$ nm, $b = 1.2509$nm and $c =$

1.2600 nm, can be described as a layer structure consisting of ten layers with a stacking sequence of A B C C' B' A' B' C' C B perpendicular to the *b*-axis, where A and A', B and B', and C and C' have a twofold rotationally symmetric relationship to each other [29]. There are mixed sites (MSs) of Al and Mn atoms, and of Pd and Al atoms in the structure, and these Al-rich and Pd-rich MSs are indicated as Al and Pd/Al sites in Fig. 1, respectively. The structure is described as an arrangement of squashed hexagonal tiles with a side-length of 0.65 nm, indicated by broken lines, with two different orientations. At the corners of the hexagonal tiles, two types of pentagonal columns, which are formed by stacking of pentagonal arrangements of Al and Mn atoms, and central atoms in the pentagonal arrangements, are located, as indicated by circles with solid and broken lines. Mn atoms on the A and A' planes are arranged with pentagonal tilings with a bond-length of 0.47 nm (hereafter referred to as 0.47 nm pentagonal tiling), as indicated by the solid lines, and the pentagonal columns are located in pentagonal tiles with one orientation in the A plane and ones with the opposite orientation in the A' plane.

Figure 6 shows an HAADF-STEM (a) image of the $Al_3(Mn, Pd)$ crystal, taken with the incident beam parallel to the *b*-axis, and a schematic illustration of bright dots in the image (b). Three types of bright dots with different levels of brightness, which

Fig. 4
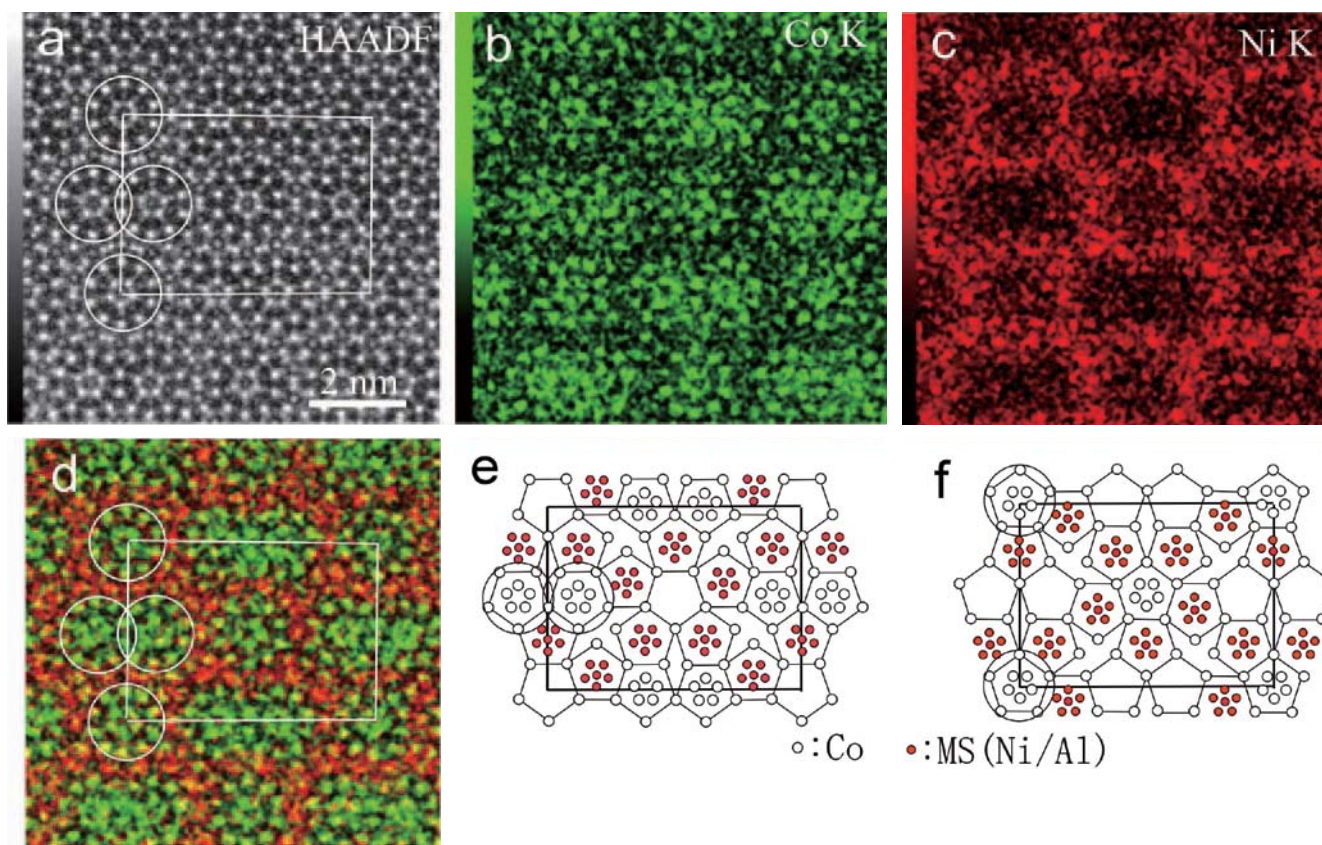
HAADF-STEM image (a), atomic-resolution EDS maps (b, c) of the PD3c approximant for the same area, and (d); the superimposed image of the two maps, (b) and (c). The 1.2 nm clusters are indicated by circles in (a) and (d), and rectangles in (a) and (d) are the unit cell. Note that the chemical ordering of Co and Ni occurs between the TM positions arranged in the 0.76 nm pentagonal tilings and pentagonal MSs, as shown in (e) and (f) of the A and B planes.

Fig. 5
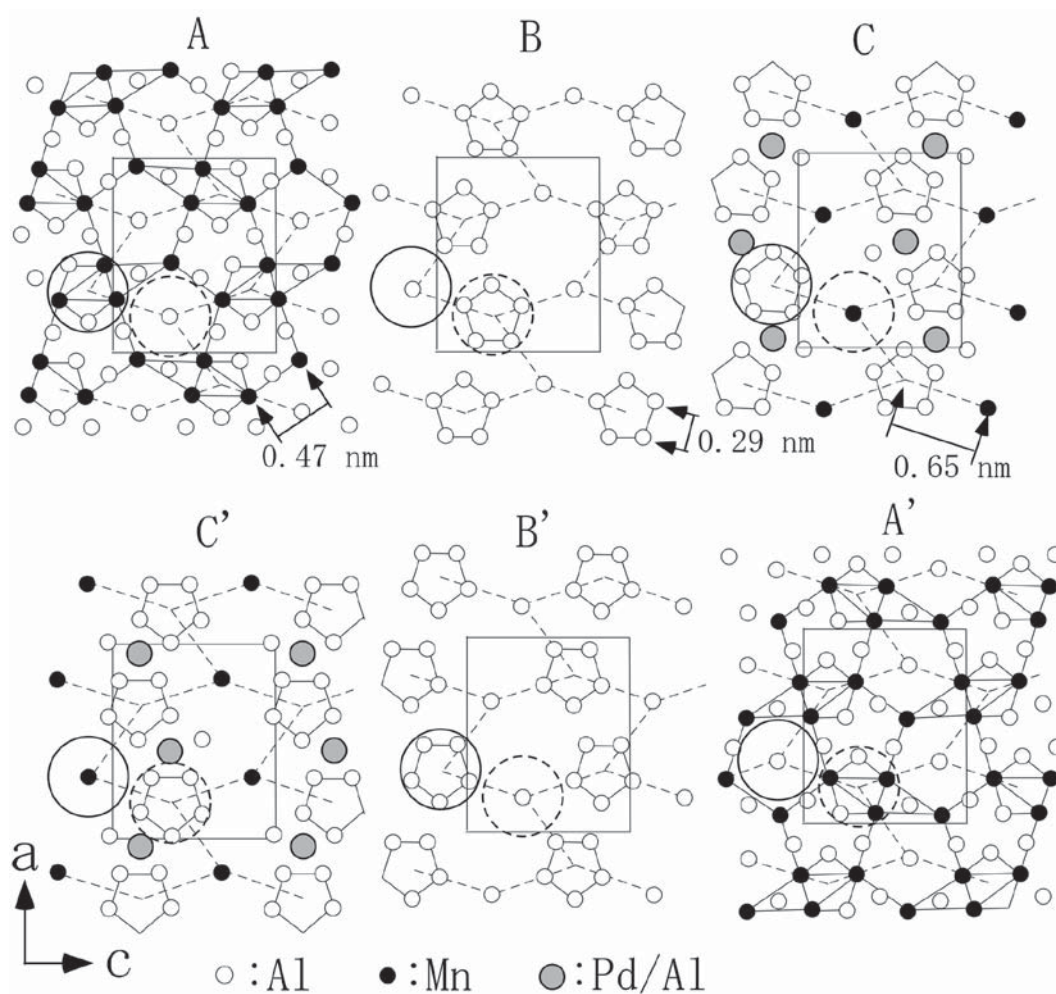
Atomic arrangements of the six layers, A, B, C, C', B' and A', in the Al$_3$(Mn, Pd) structure with a stacking sequence of A B C C' B' A' B' C' C B, where A and A', B and B', and C and C' have a two-fold rotationally symmetric relationship to each other. Note that the two types of pentagonal columns, consisting of stacking of pentagonal arrangements of Al and Mn atoms, and also the central atoms, are located at the corners of the hexagonal tiles, as indicated by circles with the solid and broken lines. Mn atoms on the A and A' layers are arranged in pentagonal tilings with a bond-length of 0.47 nm. Mixed sites of Pd and Al atoms are indicated by Pd/Al sites.

Fig. 6
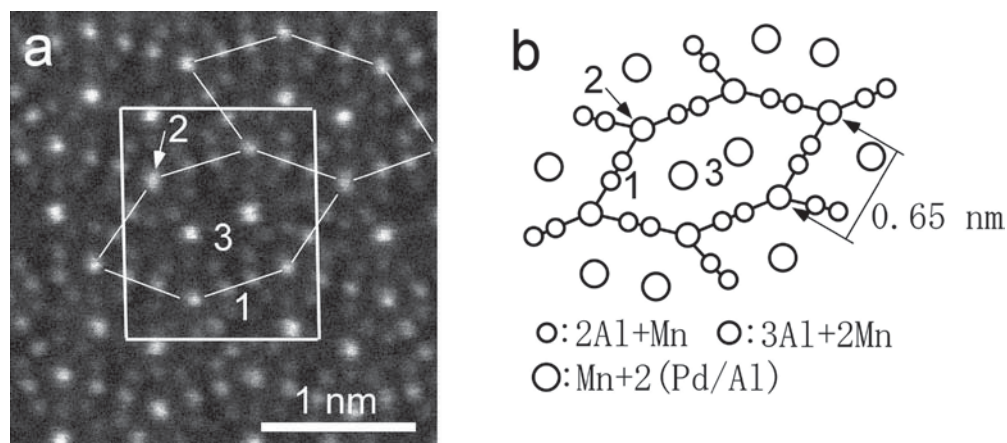
HAADF-STEM image (a) of the Al$_3$(Mn, Pd) crystal, taken with the incident beam parallel to the b-axis, and schematic intensity distribution (b) derived from the structure of Fig. 5. Three types of bright dots with different contrasts, numbered by "1," "2," and "3" in (a, b), can be understood to be projected positions of two Al atoms and one Mn atom, three Al and two Mn atoms, and one Mn and two Pd/Al atoms, respectively, in the unit cell.

JEOL NEWS │ Vol.50 No.1 (2015)

are numbered "1," "2," and "3" in the HAADF-STEM image (Fig. 6(a)), can be understood by the projective atomic positions of two Al atoms and one Mn atom, three Al and two Mn atoms, and one Mn and two Pd/Al atoms, respectively, in the unit cell, as can be seen from Fig. 5.

Figure 7 shows an HAADF-STEM image (a) and the corresponding EDS maps (b-d) for Mn, Pd and Al elements in the Al$_3$(Mn, Pd) crystal. In the EDS map of Fig. 7(b), the projected positions of the Mn atoms at corners and around the centers of the hexagonal tiles with two orientations can be clearly seen. Further the projected positions of the two Pd/Al MSs have been detected inside the hexagonal tiles in Fig. 7(c). On the other hand, the Mn positions on sides of the hexagonal tiles, numbered as "1" in Fig. 6(a), cannot be clearly observed, because these positions have a short interval, compared with the other positions of Mn atoms. The observed STEM images and atomic-resolution EDS maps of the Al-Mn-Pd DQC have been interpreted in this paper using the above knowledge of the Al$_3$(Mn, Pd) study.

Figure 8 shows an HAADF-STEM of the Al-Mn-Pd DQC, taken with the incident beam parallel to the periodic axis. In the image, decagonal (D-), star-shaped pentagonal (P-), and squashed hexagonal (H-) units with an edge-length of 0.65 nm can be drawn according to Figs. 6(a). All the D-units are joined with an edge-sharing linkage and gaps in the arrangement of the D-units are completely filled with P- and H-units. This characteristic structural feature has already been reported in a previous paper [25]. Thus, the determination of atomic arrangements in the three polygonal units leads to a model for the structure of the Al-Mn-Pd DQC.

Figure 9 shows enlarged HAADF-STEM images of a segment of Fig. 8. The bright dots in the image are connected by the two types of the 0.47 nm pentagonal tilings being similar to those on the A and A' planes in the Al$_3$(Mn, Pd) structure, as shown in Figs. 9(b) and 9(c).

Figure 10 shows an HAADF-STEM image (a) and EDS maps (b-d) of the Al-Mn-Pd DQC, taken with the incident beam parallel to the periodic axis. The EDS maps show that the central region of the D-units, which is represented as brighter spots in Fig. 10(a), correspond to Pd-rich and Mn-poor area. This result suggests that the brighter dots around the centers of the D-units in Fig. 10(a) are produced mainly by the projection of Pd atoms. The enrichment of Pd around the centers of the D-units was already postulated by Abe from observation of a Cs-corrected

Fig. 7
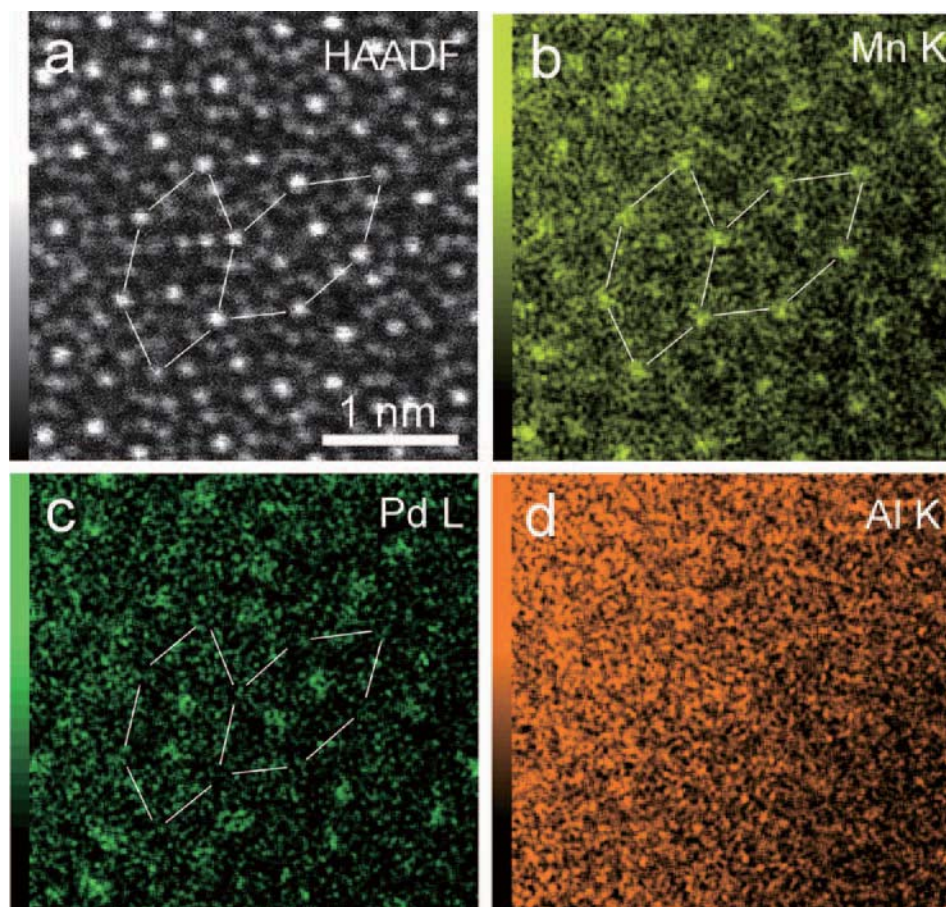

HAADF-STEM image (a) and atomic-resolution EDSs (b,c,d) of the Al$_3$(Mn, Pd) crystal. In (b), the projected positions of Mn atoms at the corners and around the centers of the hexagonal tiles with two orientations can be clearly seen, and also Pd/Al MSs has also been detected around the centers of the hexagonal tiles in (c).

24

Fig. 8
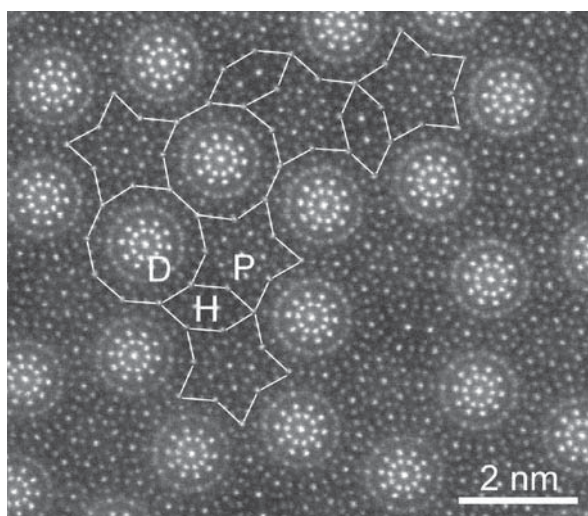
HAADF-STEM image of the Al-Mn-Pd DQC, taken with the incident beam parallel to the periodic axis. In the image, lines with a length of 0.65 nm form decagonal (D-), star-shaped pentagonal (P-), and squashed hexagonal (H-) units. Note that all the D-units are joined with an edge-sharing linkage and gaps in the arrangement of the D-units are completely filled with the P- and H-units.

Fig. 9
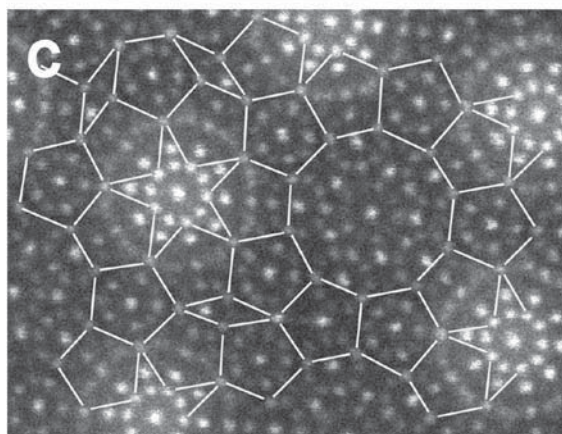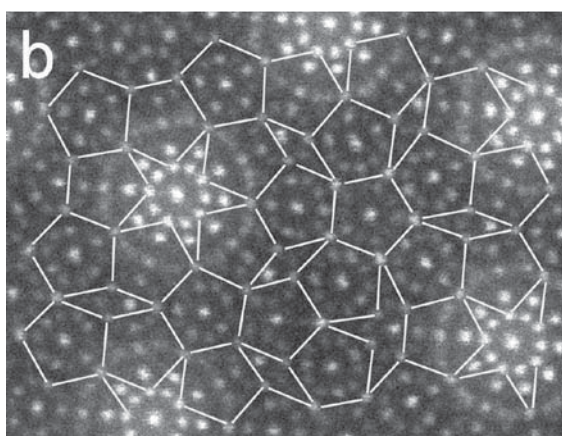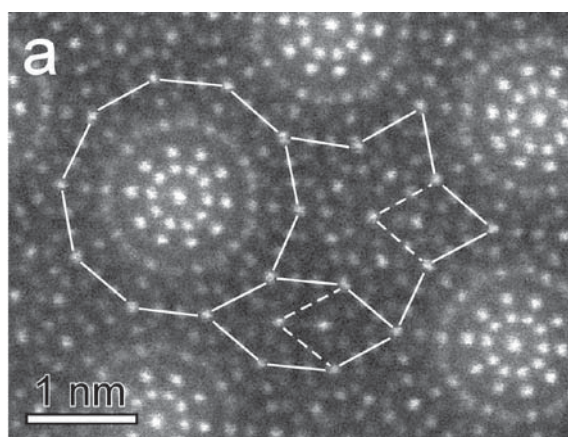
Enlarged STEM images of a section of Fig. 8. One can see from a comparison with Fig. 6 that the structure of the H-unit is exactly the same as that of an Al_3(Mn, Pd) hexagonal tile, and the contrast distributions in the rhombus, which forms the structure of the P-unit, indicated by broken lines in (a), are similar to those in the H-unit. The bright dots in the image are connected by two types of 0.47 nm pentagonal tilings, which are expanded from those of the A and A' planes in the Al_3(Mn, Pd) structure, as indicated in (b) and (c).

Fig. 10
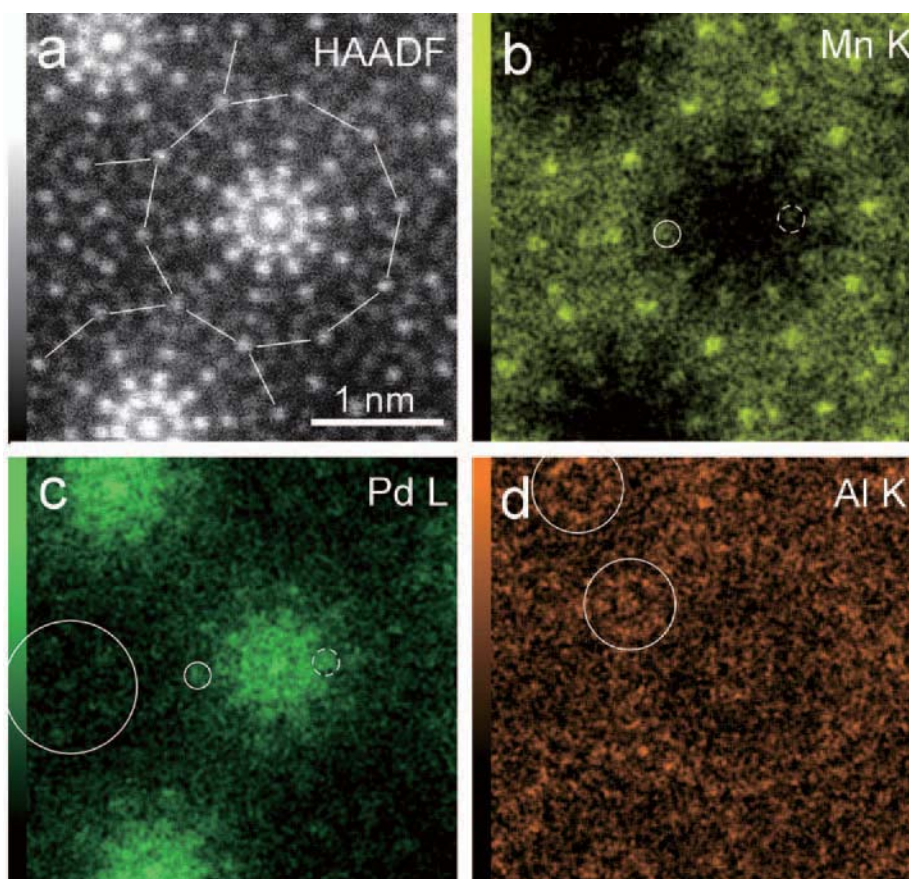
HAADF-STEM image (a) and atomic-resolution EDSs (b,c,d) of the Al-Mn-Pd DQC. The EDS maps show that the central regions of the D-units, which are formed by brighter spots in (a), correspond to Pd-rich and Mn-poor areas. Note the pentagonal arrangement of weak dots in a large circle of (c), and Mn-rich Mn/Pd and Pd-rich Pd/Mn MSs indicated by small circles with solid and broken lines, respectively. Also, it should be noticed in the EDS map of Al (d) that a donut-like shaped intensity distribution in the D-unit are observed, and that annular intensity distributions indicated by circles correspond to the projection of the pentagonal columns.

HAADF-STEM image [30]. Further, a pentagonal arrangement of weak dots around the center of the P-unit can be seen, as indicated by a large circle in Fig. 10(c), and mixed sites of Mn and Pd indicated by small circles with solid and broken lines can be recognized. Also, it should be noticed in the EDS map of Al that donut-like shaped intensity distribution in the D-unit are observed. The intensity distribution can be considered to correspond to the projection of the pentagonal columns, which are located at vertices of the D-unit, as indicated by circles in Fig. 10(d).

Figure 11 shows atomic arrangements of Mn and Pd atoms, and these mixed sites on the A and A' planes (a), and C and C' planes (b) in the D-, P- and H-units of the Al-Mn-Pd DCQ structure, which are derived from the observed STEM images and EDS maps. The atomic arrangements of the P- and H-units are directly determined from the observed STEM images and EDS maps on the basis of the $Al_3(Mn, Pd)$ structure. An arrangement of Mn and Pd atoms, and the MSs of Mn and Pd atoms in the D-unit can be determined most directly from the observed STEM image and EDS maps. In Fig. 11, the Mn-rich and Pd-rich MSs of Mn and Pd atoms are indicated by Mn/Pd

and Pd/Mn sites, respectively. Steurer et al. [31], and Weber and Yamamoto [32] proposed a structural model of an Al-Mn-Pd DCQ by X-ray diffraction analysis using a single quasicrystal, but they did not find the enrichment of Pd around the centers of the D-unit. Therefore, it can be said that the combination of atomic-resolution EDS mapping with STEM observations gives us valuable information about the structure of DCQs, which cannot be obtained by conventional methods.

Summary

Atomic-resolution EDS maps obtained by integrating many sets of EDS data taken from fresh areas at each time by shifting the sample clearly represents chemical ordering of Co and Ni atoms in the crystalline approximants related to the Al-Co-Ni DQCs, and Mn and Pd atoms in the Al-Mn-Pd DQC. This method is a powerful technique to overcome the electron damage by the strong electron beam in the FEG microscopes and the long exposure times required to obtain high-resolution EDS maps, and the combination of the atomic-resolution EDS mapping with high-resolution STEM observations using *Cs-*

Fig. 11
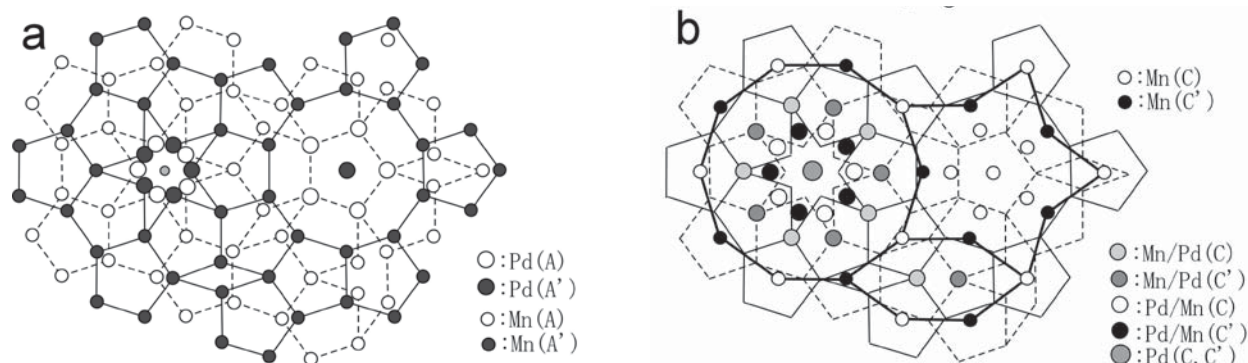
Arrangements of Mn and Pd atoms in the A and A' planes (a), and C and C' planes (b), in the D-, S- and H-units of the Al-Mn-Pd DCQ structure, derived from the observed STEM images and EDS of Figs. 9 and 10. The atomic arrangements of the P- and H-units are directly determined from the observed STEM images and EDS maps on the basis of the Al$_3$(Mn, Pd) structure. Mn-rich and Pd-rich MSs of Mn and Pd atoms are indicated by Mn/Pd and Pd/Mn sites, respectively.

corrected STEM indicates a possibility as a new and powerful technique of structural analysis. We would like to expect that accumulation of the data performed manually at present will be computerized in the future.

References

[1] A. Yasuhara, K. Saito and K. Hiraga, *Aperiodic Crystals*, ed. By S. Schmid, R. L. Withers and R. Lifshits (Springer Netherlands, 2013) p.219.

[2] K. Yubuta, A. Yasuhara and K. Hiraga, *Aperiodic Crystals*, ed. By S. Schmid, R. L. Withers and R. Lifshits (Springer Netherlands, 2013) p.225.

[3] K. Sugiyama, A. Yasuhara and K. Hiraga, *Aperiodic Crystals*, ed. By S. Schmid, R. L. Withers and R. Lifshits (Springer Netherlands, 2013) p.237.

[4] K. Hiraga and A. Yasuhara, *Mater. Trans*. **54** (2013) p.493.

[5] K. Hiraga and A. Yasuhara, *Mater. Trans*. **54** (2013) p.720.

[6] K. Yubuta, K. Yamamoto, A. Yasuhara and K. Hiraga, *Mater. Trans*. **55** (2014) p.866.

[7] A. Yasuhara, K. Yamamoto, K. Yubuta and K. Hiraga, Acta Physica Polonica (Proc. of 12th Inter, Conf. on the quasicrystals (ICQ12)) A**126** (2014) p.637.

[8] K, Hiraga, A. Yasuhara, K. Yamamoto and K. Yubuta, *Philo. Mag*. **95** (2015) p.1524.

[9] K. Saitoh, K. Tsuda, M. Tanaka, K. Kaneko and A. P. Tsai, *Jpn. J. Appl. Phys*. **36** (1997) p.1400.

[10] K. Hiraga, *Advances in imaging and electron physics* (Elsevier Science (USA)) vol. 122 (2002) p.1.

[11] S. Deloudi and W. Steurer, *Philo. Mag*. **87** (2007) p.2727.

[12] M. Watanabe, *X-ray energy-dispersive spectrometry in scanning transmission electron micro-scopes, in Scanning Transmission Electron Microscopy, Imaging Analysis*, S.J. Pennycook and P.D. Nellist, eds., Springer, New York Dordrecht Heidelberg London, 2011, p.291.

[13] A. Yasuhara, K. Yubuta and K. Hiraga, *Philo. Mag*. Lett. **94** (2014) p.539.

[14] A. Yasuhara and K. Hiraga, *Philo. Mag*. **95** (2015) p.52.

[15] A. Yasuhara and K. Hiraga, *Philo. Mag*. **95** (2015) p.1511.

[16] K. Edagawa, M. Ichihara, K. Suzuki and S. Takeuchi, *Phil. Mag. Lett*. **66** (1992) p.19.

[17] A. P. Tsai, *Phil. Mag. Lett*. **74** (1996) p.233.

[18] S. Ritsch, C. Beeli, H. U. Nissen, T. Gödecke, M. Scheffer and R. Lück, *Phil. Mag. Lett*. **78** (1998) p.67.

[19] B. Grushko, D. Holland-Moritz, R. Wittmann and G. Wilde, *J. Alloys Comp*. **280** (1998) p.215.

[20] S. Hovmoller, L. Hovmoller Zou, X. Zou and B. Grushko, *Phil. Trans. R. Soc*. A **370** (2012) p.2949.

[21] K. Sugiyama, S. Nishimura and K. Hiraga, *J. Alloys Comp*. **342** (2002) p.65.

[22] S. J. Pennycook, *A scan through the history of STEM, in Scanning Transmission Electron Mi-croscopy, Imaging Analysis*, S.J. Pennycook and P.D. Nellist, eds., Springer, New York Dordrecht Heidelberg London, 2011, p.1.

[23] C. Beeli, H. -U. Nissen and J. Robadey, *Philo. Mag. Lett*. **63** (1991) p.87.

[24] K. Hiraga, W. Sun, J. Lincoln. M. Kaneko and Y. Matsuo, *J. Appl. Phys*. **30** (1991) p.2028.

[25] K. Hiraga and W. Sun, *Philo. Mag. Lett*. **67** (1993) p.117.

[26] W. Sun and K. Hiraga, *Philo. Mag. Lett*. **73** (1996) p.395.

[27] K. Hiraga, M. Kaneko, Y. Matsuo and S. Hashimoto, *Philo. Mag*. B **67** (1993) p.193.

[28] H. Klein, M. Boudard, M. Audier, M. De Boisssieu, H. Vincent, L. Beraha and M. Duneau, *Philo. Mag. Lett*. **75** (1997) p.197.

[29] Y. Matsuo, M. Kaneko, T. Yamanoi, N. Kaji, K. Sugiyama and K. Hiraga, *Philo. Mag. Lett*. **76** (1997) p.357.

[30] E. Abe, *JEOL News* **45** (2010) p. 20.

[31] W. Steurer, T. Haibach, B. Zhang, C. Beeli and H. -U. Nissen, *J. Phys.: Condens. Matter*. **6** (1994) p.613

[32] S. Weber and A. Yamamoto, *Philo. Mag*. A **76** (1998) p.85.

Dressing Living Organisms in the NanoSuit® for FE-SEM Observation

Takahiko Hariyama and Yasuharu Takaku

Departments of Biology, Hamamatsu University School of Medicine

Scanning electron microscopy (SEM) has made remarkable progress, and has become an essential tool for observing biological materials. However, they are required to be completely dry, since the specimen chamber is at high vacuum. The living soft-bodied organisms require chemical fixation and following various complex procedures to preserve and stabilize their structure. In this article, we demonstrate a new method with which living organisms can be observed by a field emission (FE) SEM. Using this method, active movements of living animals were observed in *vacuo* (10^{-3}-10^{-5} Pa) by protecting them with a coating of thin polymer membrane, the NanoSuit®, and it was found that the surface fine structure of living organisms is very different from that of traditionally treated samples. After observation of living organisms, despite the high vacuum it was possible to rear many of them subsequently in normal culture conditions. This method will be useful for numerous applications, particularly for electron microscopic observations in the life sciences.

Introduction

Soon after the first scanning electron microscopic observation was performed using non-organic materials by Knoll [1], biological observations began and the fine structure of many organisms was investigated. Because the electron microscope uses a beam of electrons to illuminate the specimen, it is necessary to evacuate the specimen chamber in order to prevent scattering by molecules in the air. All biological samples routinely require sacrifice and dehydration before observation, because approximately 70 to 80 percent of all living organisms are water, which rapidly evaporates under high vacuum, and consequently leads to disruption and collapse of structure. To preserve and stabilize biological structure for conventional SEM observations, complex treatments are required; chemical fixation and careful drying procedures, such as critical point drying [2]. Furthermore, non-conductive materials are difficult to be imaged in a conventional SEM, because when non-conductive materials are directly illuminated with an electron beam, electrons with a negative charge collect locally (specimen charge-up), thus preventing normal emission of secondary electrons. This charge-up causes some unusual phenomena such as abnormal contrast and image deformation and shift. Therefore, samples usually require an ultrathin coating of electrically conducting materials [3]. Consequently, many and time-consuming procedures were required to observe biological samples, and no living samples were observed by SEM with some exceptions [4]. These various procedures preclude observation of living organisms.

A new method is here presented to observe living organisms by a field emission scanning electron microscope (FE-SEM). We have previously reported that a simple surface modification by electron beams or plasmas can equip some multicellular organisms with a thin extra layer, coined the "NanoSuit", and hence can keep them alive under the high vacuum (10^{-3}-10^{-5} Pa) conditions of a FE-SEM [5, 6, 7]. In this article, we summarize the role of the NanoSuit, various living specimens were simply protected by the NanoSuit, during FE-SEM observations. From the success of this technique, it is anticipated that this could be the epoch-making discovery for more sophisticated observation of living organisms with the electron microscope and for the creation of new areas of biology, chemistry and physics in order to explain how the thin polymer membrane forms a gas and/or liquid barrier based on the Surface Shield Effect (SS-effect) to preserve life *in vacuo*.

Experimental

Experimental living organisms

Third-instar larvae (ca. 3 mm in body length) of the fruit fly *Drosophila melanogaster* (Oregon-R) were used. These dipteran larvae possess a soft cuticle covered by extracellular substances (ECSs) [8]. To exclude any effects of culture medium, the larvae were washed at 24 ± 1 °C with distilled water several times before the experiment. Fourth-instar larvae of the mosquito *Aedes albopictus* (ca. 5 mm in body length) and fourth-instar larvae of the mosquito *Culex pipiens molestus* (ca. 6 mm in

〉〉 1-20-1 Handayama, Higashi-ku, Hamamatsu 431-3192, Japan │ E-mail: hariyama@hama-med.ac.jp

body length), collected from puddles and maintained in the same water in which they were found, were also used. These larvae have a soft cuticle not covered by ECS. To exclude any effects of the water, they were transferred to distilled water at 24 ± 1 °C for 2 d before the experiment, with distilled water changes every 12 h. The larvae were rinsed thoroughly in distilled water 1 h before experiments began. The initial weights of single *Drosophila* and *Culex* larvae were about 1.2 mg and 2.2 mg, respectively. Five larvae were measured for each trial, and five trials (n = 25) were performed for each species under each condition.

The larvae of a chironomid midge, *Chironomus yoshimatsui*, were collected from the mud of a rice paddy, and then cultured in the muddy water brought from the same paddy. The fourth larval instar (ca. 4 mm in body length) was used. In order to exclude any effects of the water, they were transferred to distilled water at 24 ± 1℃ for two days prior to the experiment, with distilled water changes every 12 h. The larvae were rinsed thoroughly in distilled water one hour before experiments began.

Specimens of the amphipod sandhopper, *Talitrus saltator*, were collected on a sandy beach in southern Tuscany, transported to the laboratory in plastic boxes containing wet sand, and maintained in an aquarium containing sand moistened with artificial seawater at 20 ± 1℃. They were fed weekly with dry fish food placed on blotting paper. The experimental animals were rinsed thoroughly in distilled water one hour before experiments began.

Preparation of Tween 20 solutions and sample preparation for FE-SEM to observe living specimens

The amphiphilic surfactant compound polyoxyethylene (20) sorbitan monolaurate (Tween 20; Wako Pure Chemical Industries) was used for all the experiments to mimic natural extracellular substances (ECS) [8]. To form the NanoSuit, the organisms were dipped into 1% (v/v) Tween 20 solution dissolved in distilled water for 1 min, blotted briefly on a dry filter paper to remove excess solution. Then the living specimen was introduced into the SEM to construct a Tween 20 film, without performing any traditional treatments such as chemical fixation or dehydration.

Preparation for standard scanning electron microscopy.

For standard SEM observation, animals were prefixed with 2% glutaraldehyde and 2% paraformaldehyde in 0.1 M cacodylate buffer (pH 7.4) and postfixed in 1% OsO_4 in the same buffer. The specimens were then dehydrated, freeze dried (JFD-300, JEOL), and ultra-thin coated with Osmium Tetroxice (PMC-5000, Meiwa).

Microscopy

For FE-SEM observations, we used a JSM-7100F (JEOL) operated at acceleration voltages of 1.0 kV. The vacuum level of the observation chamber was 10^{-3} to 10^{-5} Pa. Images are captured using a lower electron detector (LED) which is located under the objective lens. Other details in conditions were as follows: working distance, 8 mm; scan speed, each beam is 10-15 frames per second. To record the dynamic movements of animals, imaging data from the SEM were directly transferred to a Hi-band digital-formatted video recorder (SONY, BDZ-EW500).

Transmission electron microscopy (TEM) observations were carried out using a JEM-1220 (JEOL).

Results

High vacuum tolerant animal

In order to find the nature tolerance of living organisms to high vacuum condition, we introduced numerous living organisms belonging to various taxa directly into the SEM to see how long they survived under high vacuum (10^{-3} to 10^{-5} Pa). Almost all of their structural integrity was completely destroyed by rapid evaporation under high vacuum (**Fig. 1**(a-c)). We, however, found that *Drosophila* larvae tolerated the high vacuum well. Although they have a soft cuticle covered by extracellular substances (ECSs) [8] they continued to actively move around for 60 min under the SEM (n = 25) (Fig. 1(d)) and

Fig. 1

Living organisms were introduced directly into a FE-SEM. Many of them were destroyed (a-c) except the *Drosophila* larva (d).
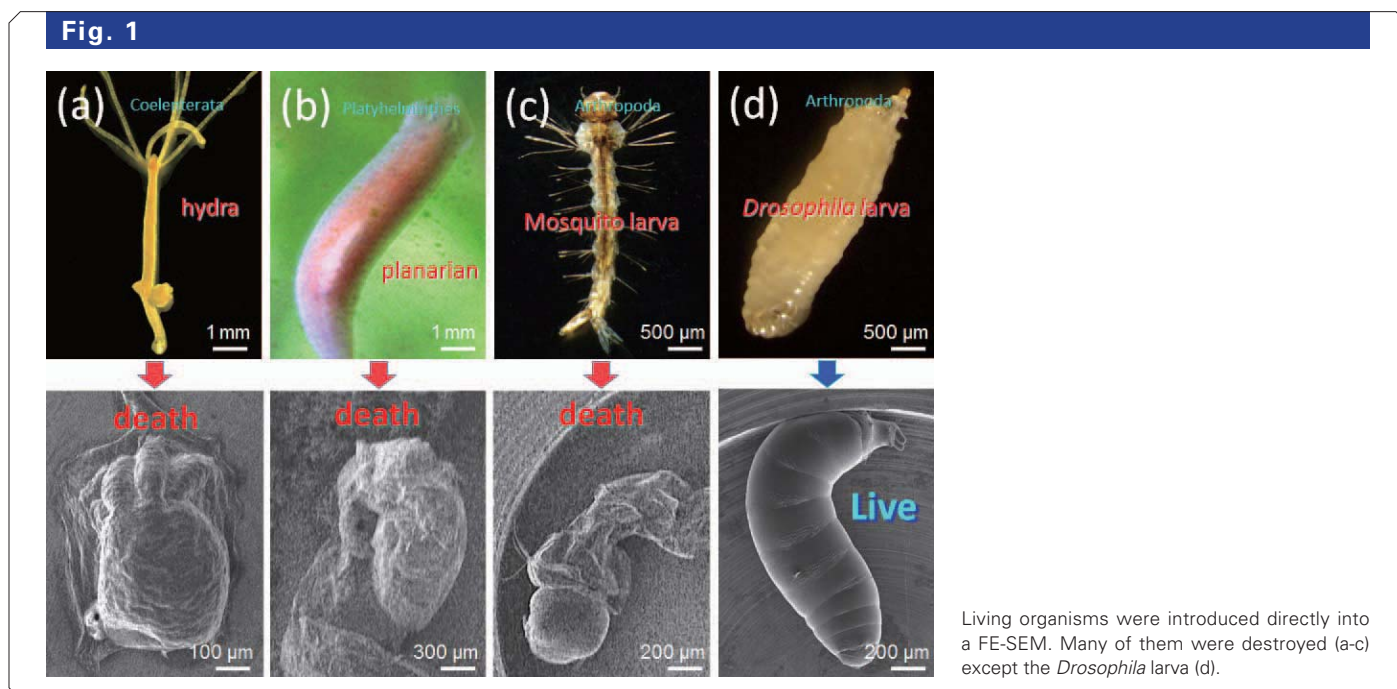
subsequently some of them (n=18) developed normally.

Using *Drosophila* larva, no apparent structural changes occurred (**Fig. 2**(a-c)). However, when control larvae (Fig. 2(f)) were placed in the SEM observation chamber for 60 min at an identical vacuum level, but without concurrent electron-beam radiation (Fig. 2(e)), subsequent SEM observations revealed they were all dead and structurally badly distorted (Fig. 2(g)). Transmission electron microscopy (TEM) showed that animals subjected to SEM electron bombardment immediately produce an extra thin layer (ca.50 to 100 nm thickness) over their surface (Fig. 2(d)). No such layer was detected in animals that had been exposed *in vacuo* for the same time but without electron bombardment (Fig. 2(h)).

Electron-beam and/or plasma irradiation

Those results described above led to the hypothesis that electron-beam irradiation [9] enhanced cross-linking within the ECS to form a durable polymer on the surface and that this polymer increased resistance to vacuum conditions. To test this hypothesis, surface polymerization was achieved by a plasma irradiation. The ionized particles of plasma provide the energy necessary to initiate polymer formation, enabling uniform coating of surfaces with solvent-insoluble polymers [10]. Although plasma polymerization so far has been used only in creating new inert industrial materials or modification of their surfaces [11], we applied this technique to the ECS of living animals to construct a protective surface barrier referred to as the NanoSuit. Plasma-irradiated specimens left *in vacuo* for 60 min before SEM observation clearly showed features similar to specimen electron-beam irradiation by SEM *ab initio*: *Drosophila* larvae moved continuously, seemingly unharmed without problems of electrical charging. The weight of each larva was measured just before the experiment and 60 min later following exposure to high vacuum. Non-irradiated control larvae and larvae pretreated by plasma radiation showed mean body weight decreases of 56.3 $\pm$ 6.0% and 8.7 $\pm$ 3.8%, respectively (n = 25), demonstrating the effectiveness of the surface shield effect by the surface membrane formed by plasma irradiation.

Mimicking ECS for other animals

To mimic the ECS which could create the NanoSuit, solutions including amphiphilic molecules were then tested. One of the best results obtained at the first stage was a solution of Tween 20, a nontoxic compound commonly used in biological experiments [12]. To test the barrier properties of the NanoSuit made by this solution, the surfaces of a certain animals previously unable to survive SEM exposure were provided exogenous materials by immersing them in 1% Tween 20 solution before electron or plasma irradiation. **Fig. 3**(a-c) show typical results obtained with larvae of the Asian tiger mosquito, *Aedes albopictus*. The larvae of the mosquitoes are aquatic and possess a soft bodied cuticle with no apparent ECS. When live larvae of *A. albopictus* were observed under the SEM without any additional treatment, they quickly shrank and ceased to move (Fig. 1(c)). Larvae treated with a 1% Tween 20 solution but not irradiated in the SEM showed the same collapsed structure when observed 30 min later. However, living larvae (Fig. 3(a)) covered with 1% Tween 20 and observed by SEM *ab initio* retained their morphology and exhibited active movements for 30 min (Fig. 3(b)). After rearing the latter for 3-4 days, ca. 80% pupated and developed successfully into adult mosquitoes (n = 25) (Fig. 3(c)).

We also investigated the larvae of other mosquito species, the northern house mosquito, *Culex pipiens molest*. The animal which was irradiated by plasma alone and observed under SEM without any additional treatment (untreated specimens) quickly shrank and ceased to move with electrostatic charging beginning after about 30 min. However, larvae briefly immersed in 1% Tween 20 solution before plasma irradiation formed the NanoSuit (treated specimens), showed rapid movements during 30 $\pm$ 10 min of SEM observation, and suffered no observable morphological change. Untreated and treated specimens showed decreases in weight of 70.3 $\pm$ 4.6% and 11.3 $\pm$ 2.7%, respectively, after 30 min *in vacuo* (n = 25). These results strongly suggest that the artificial ECS played a significant role as an extra barrier, the NanoSuit, ameliorating the effects of high vacuum.

Larvae of *C. pipiens molestus* irradiated by plasma alone and observed under SEM without any additional treatment (**Fig. 4**(a)) quickly shrank and ceased to move (Fig. 4(b)), with electrostatic charging beginning after about 30 min (Fig. 4(c)). However, larvae briefly immersed in 1% Tween 20 solution before plasma irradiation formed the NanoSuit (treated specimens), showed rapid movements during 30 $\pm$ 10 min of SEM observation, and suffered no observable morphological change (Fig. 4(g), (h)). In addition, we found that the fine structure of the surviving larvae was completely different from that of untreated specimens and traditionally prepared specimens (Fig. 4(d) cf. Fig. 4(i)). Each segment of the living animal seemed perfectly preserved and complete (Fig. 4(g-i)), with ample body fluid (haemolymph) apparently retained inside. There were many wrinkles in the furrows in the control treatment (Fig. 4(d) arrowheads), but such wrinkles were completely absent in the treated specimen (Fig. 4(i)). TEM images clearly showed that the surface of the treated specimen was covered with the NanoSuit of from 50 to 100 nm thickness (Fig. 4(j)), whereas no NanoSuit was observed at the surface of the untreated specimen (Fig. 4(e)). Although high-magnification imaging ($\times$200,000) of treated specimens was possible only when the living animals remained motionless during scanning, the observation of neatly ordered structure suggests that the natural surface structure of the animal is conserved and strongly supports our notion that the NanoSuit can preserve the "real-life appearance" down to microscopic details.

The NanoSuit® for other living organisms

As described above, when living organisms are covered with either a layer of natural extracellular substance (ECS), or an artificial substance that mimics ECS), subsequently polymerized by plasma or electron beam irradiation, organisms are covered by the NanoSuit, and have the potential to tolerate high vacuum environments without any electric charges [5]. We extended to a variety of living organisms in a FE-SEM to investigate the role of the NanoSuit. All tested animals survived, including the larva of a chironomid, *Chironomus yoshimatsui*, the flatworm *Dugesia japonica*, the ant *Pristomyrmex punctatus*, and the amphipod. *Talitrus saltator*.

Figure 5(a) shows the overall shape of a midge larva. When observed in the SEM sample chamber, slight shrinkage was already detectable (Fig. 1(b)) but the specimen showed slight movements and no apparent electrostatic charging. Subsequently, the larva quickly shrank along its entire length and all movements had ceased within 5 minutes (Fig. 5(c)). Charging commenced about 10 minutes after movements had ceased. On the other hand, those washed by distilled water and subsequently dipped in Tween 20 showed no observable change in their feature, but remained alive and showed rapid movement

Fig. 2
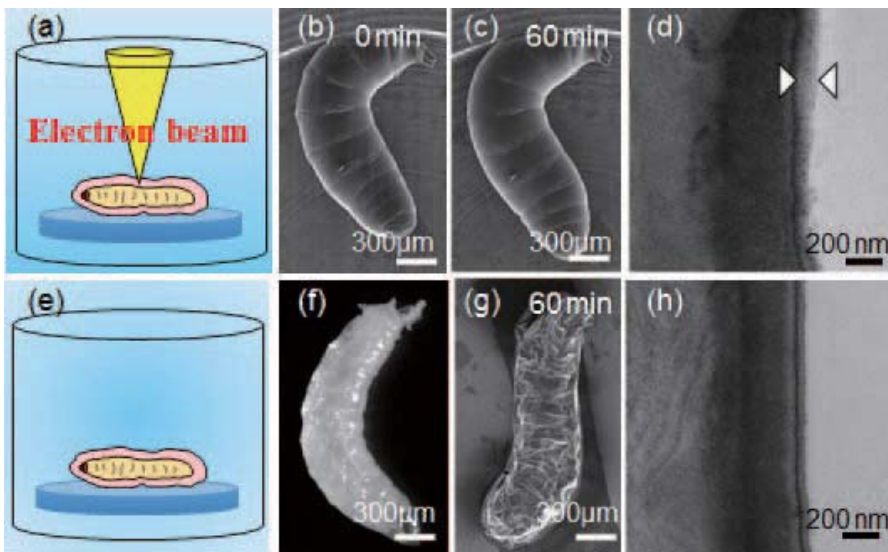
A living *Drosophila* larva was exposed *in high vacuo* and showed active movement for 60 min (a-c). Before SEM observation, a different larva (light micrograph in (f)) was introduced into the observation chamber without electron-beam irradiation. It was collapsed thoroughly when observed by SEM subsequently (g). TEM images of vertical sections through the surface of each animal are shown in (d) and (h). The layer between the arrowheads in (d) shows the newly formed outer membrane, not present in (h).

Fig. 3

A living *A. albopictus* larva (a) was exposed to electron bombardment after the quick immersion using Tween 20 solution. It moves *in high vacuo* for 60 min. The blur of the photo observed at tail was caused by its fast movement (b). 80 % of larvae observed in a SEM developed into adult mosquitoes (c).

Fig. 4
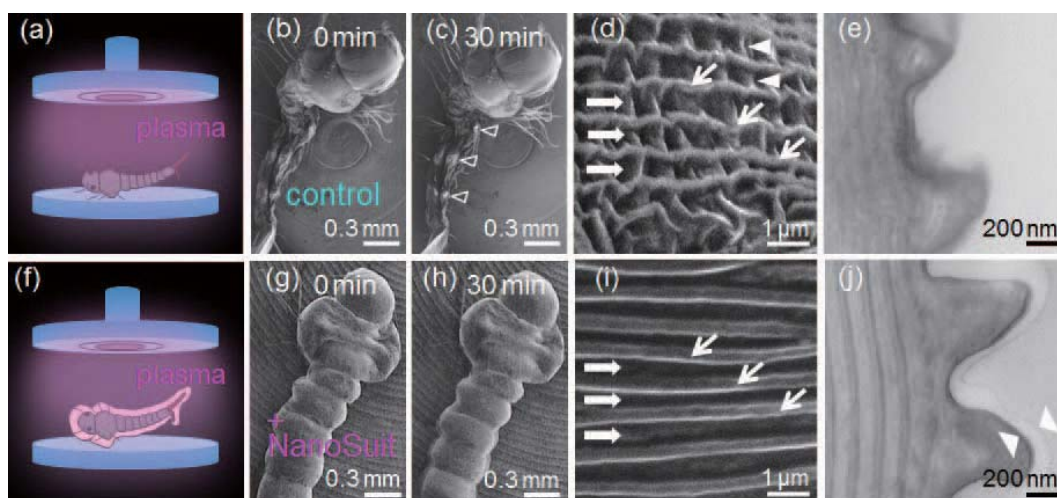
A living larval mosquito *Culex pipiens molestus* (which has no natural ECS layer) treated by plasma irradiation for 3 min (a) and observed by SEM for 30 min (b, c). Images of the larval mosquito, following early electron irradiation, protected by NanoSuit (g, h). High-magnification image of the body surface of each animal (d, i). Arrowheads in (c) indicate areas of electrostatic charging. In (e) and (j), TEM images of the surfaces of each animal are shown. Layers in j between the arrowheads indicate the newly formed NanoSuit.

(Fig. 5(d), (e)). Even after active movement ceased, the specimens showed no electrostatic charge for at least one hour.

To investigate what happens to fine structure when an organism is covered with a Tween 20 NanoSuit, conduct careful observations were made (**Fig. 6**). With the conventional method, nonconductive specimens tend to be charged when scanned by the electron beam, especially at steep edges. In contrast, with the newly developed method the tip of an antenna showed no electrostatic charge (Fig. 6(a)). Even when observed at high magnification, structural detail was clearly observed without any charging (Fig. 6(b)). No collapse was observed in any part of the soft body (Fig. 6(c)) and the large bore of the stigma located at the tail seems to have been preserved completely (Fig. 6(d)). These results indicate that the NanoSuit maintains neatly ordered structures on the surface and greatly reduces electrostatic charging.

After SEM observation of those larvae, control specimens treated in distilled water alone did not survive. However, when larvae protected by the NanoSuit were returned to the muddy water under atmospheric pressure, all the animals were found to be still alive and recovered original movements within a few minutes. After rearing these survivors for 3 to 4 days, around 70% of them pupated and developed successfully into adult mosquitoes (*N*=25).

Those results described above indicate that the NanoSuit plays an important role both in keeping the animals alive in the SEM and no electrostatic charge, presumably because it acts as a barrier against gas and liquid release from the organism and keep the organism wet: a property which is here called the "Surface shield (SS) effect". To investigate the "SS-effect" morphologically, a comparison was made between specimens treated by traditional methods (**Fig. 7**(a-d)) and those coated with the NanoSuit (Fig. 7(e-h)) [6]. The sandhopper *T. saltator* is abundant on sandy beaches around the Mediterranean and has been used in many scientific investigations, in particular concerning the mechanisms of orientation on land, in which evaporative water loss is an important issue for such a semi-

terrestrial amphipod [13, 14]. In the lateral view of the animal at low magnification, the outline of each scutum appears more clearly defined following preparation by traditional methods (Fig. 7(a)) compared with those coated by the NanoSuit (Fig. 7(e)), where the appearance is much smoother. Note also the presence of indentations indicating shrinkage in the head and anterior segments in Fig. 7(a), whereas no such shrinkage is apparent in Fig. 7(e). Considering the tip of the antenna at higher magnification, clear morphological differences are apparent. Each antennary segment has protrusions consisting of setae which are seen to be separated when prepared by traditional methods (Fig. 7(b), (c)) but neatly straight and aligned following preparation with the NanoSuit® (Fig. 7(f), (g)). The tip of the antenna similarly has a much neater appearance when protected by the NanoSuit (Fig. 7(h); cf. Fig. 7(d)).

Transparency of the NanoSuit® for the observation

To investigate how the NanoSuit allows visualization of fine structures with good resolution in the SEM, we prepared NanoSuit of varying thickness and compared the SEM images with cross sections of the NanoSuit in TEM images. **Figure 8** shows results of individual *Culex pipiens molestus* larvae treated with Tween 20. When the surface of the animal was covered by the NanoSuit®, the fine structure was visible (Fig. 8(b)), even the thickness of the NanoSuit® was about 100 nm and sometimes it fully filled between the ridges (Fig. 8(c)). However, when the surface of the NanoSuit® was covered with gold by sputtering, the fine structure of ridges disappeared (Fig. 8(e)). It must be the reason that the electrons cannot penetrate through the thin layer of gold (Fig. 8(f)).

To investigate the suitable concentration of Tween 20, we compared the visualization of fine structures covered by the NanoSuit of different thickness using the SEM images and the cross sections of the NanoSuit in TEM images [7]. The results of individual mosquito larvae treated with different concentrations of Tween 20 showed the different visualization. The images


Fig. 5
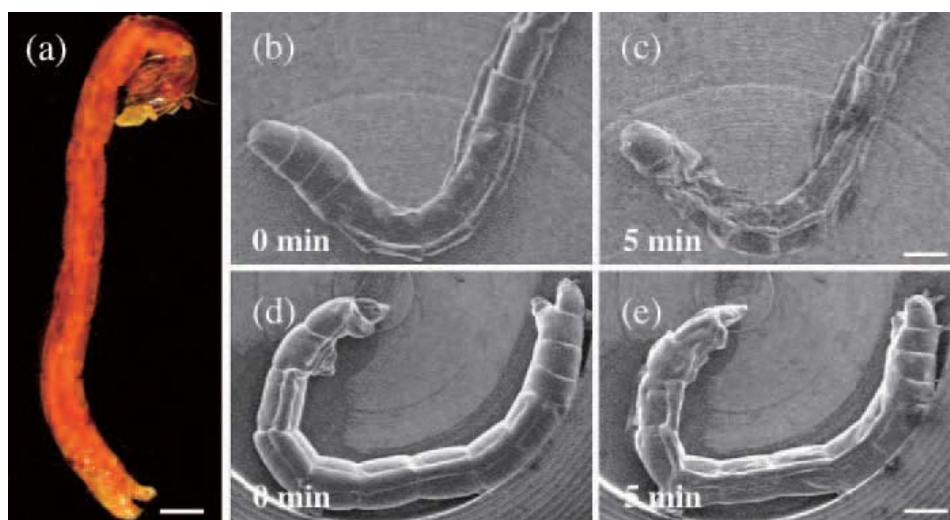
Binocular wide-field dissecting microscopic observation for a larva of a chironomid, *C. yoshimatsui* (a). The effect of distilled water and Tween 20 solution. The larva cultured in distilled water showed a quick shrinkage during SEM observation (b, c). The larva treated with Tween 20 solution kept its feature and moved actively (d, e). Scale bar, 300 μm.
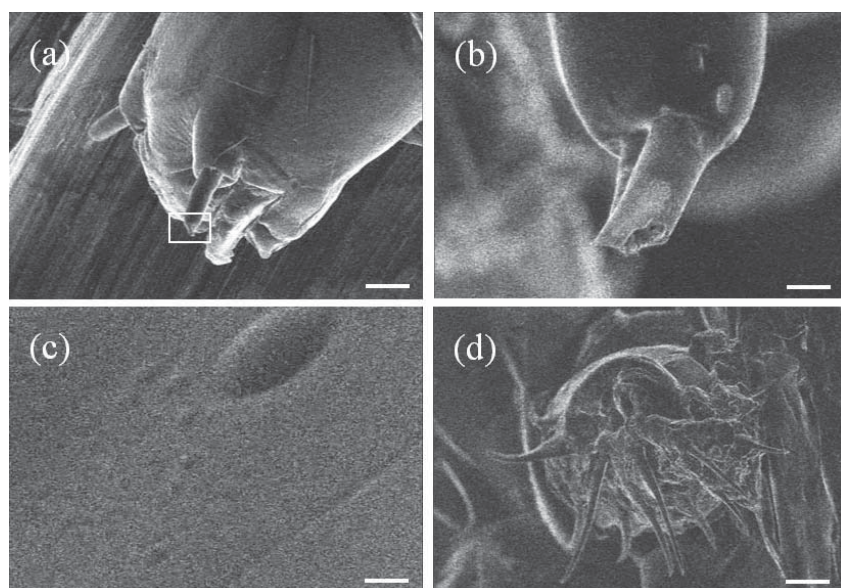
SEM observation of fine structure in a living *C. yoshimatsui*. (a) The antenna on the tip of the head. (b) White square shown in A at a higher magnification. (c) The surface of a body segment and (d) the stigma located posteriorly. Scale bars, 50 μm (a, d), 3 μm (b), 1 μm (c).
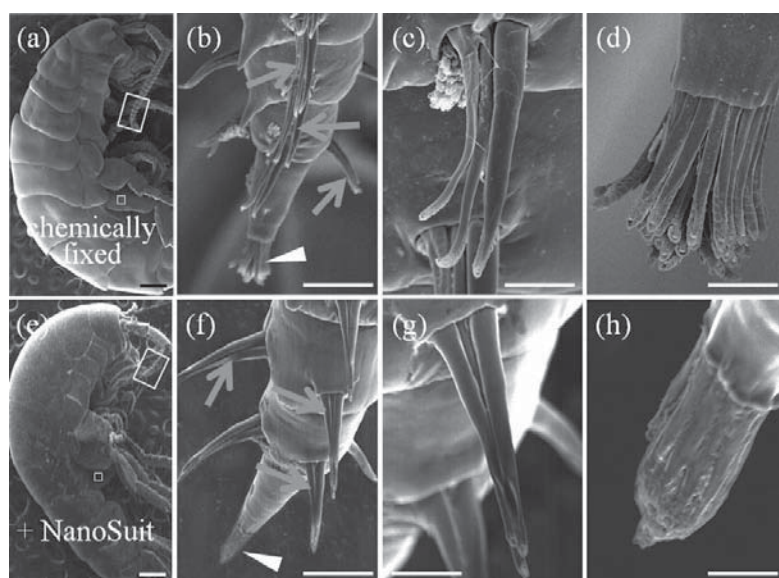
Scanning electron micrographs comparing treatments by traditional methods (a-d) and when protected by a NanoSuit (e-h). The tip of the antenna, indicated by a large square in (a) and (e), is enlarged in b and f, respectively. Each segment of the antenna tip possesses long protrusions composed of three setae (arrows). These setae appear separated (b, c) using traditional methods, but show consistent neat alignment in specimens coated with a NanoSuit (f, g). The antenna tip (arrow heads in (b) and (f)) has a bundled structure which is splayed when viewed following traditional treatment (d) but is aligned straight when the specimens is protected by a NanoSuit (h). Scale bars 0.2 mm (a, e), 20 μm (b, f), 10 μm (c, g), 5 μm (d, h).

indicate that a low concentration of Tween 20 (0.01%) is not sufficient to protect surface structures and specimens dehydrate rapidly. Higher concentrations of Tween 20 (0.1 and 1.0%) yield thin NanoSuit, which prevent dehydration and preserve the underlying structure as shown in figure 7b. Even higher concentrations of Tween 20 (10 and 50%) result in thick NanoSuit and prevent imaging of the surface fine structure.

The biomimetic ECS films made by other chemical compounds.

Covering the living organisms with a layer of the mimicked ECS, 1% Tween 20, polymerized by plasma or electron beam irradiation made the organisms highly tolerant to high vacuum. Can other biocompatible chemical compound fabricate the NanoSuit® to the living organisms? We investigated biomimetic ECS films made by plasma polymerization from surfactants, water-soluble polymers, monosaccharides, polysaccharides, lipids, amino acids, and ionic liquids [15].

Figure 8(a) shows the preparation of the biomimetic ECS films for conventional structural analysis. The monomer layer was spin-coated on a glass substrate, and then placed in an irradiation chamber. The water-soluble layer, which consisted of the monomer and water, remained wet even under vacuum (0.13 Pa). Thin films were formed on the outermost surface of the monomer layer after plasma irradiation. The unreacted monomer was removed by immersing the plasma-irradiated films in a large volume of pure water and ethanol (**Fig. 9**(a)). The insoluble plasma-irradiated films were transferred to a substrate and allowed to dry under ambient conditions, demonstrating they were free standing (Fig. 9(b-c)). The thickness of the insoluble

Fig. 8
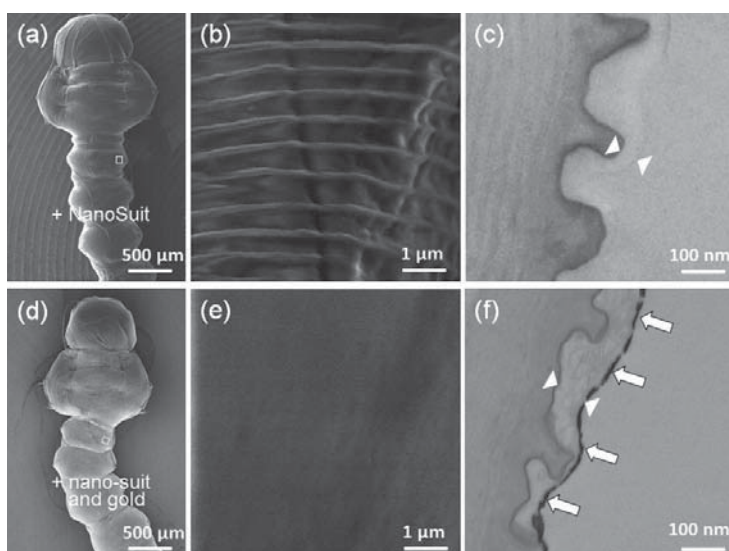
SEM and TEM images for larvae covered with a 1% Tween 20 NanoSuit (a-c), and those were spattered with Gold (d-f). The TEM image shows that the surface of the specimen was covered with a NanoSuit less than 100 nm thick (c). The alternating pattern of furrows and ridges detected by TEM under the NanoSuit appears to closely correspond to the SEM image (b, c). These results suggested that the electron beam is able to penetrate the NanoSuit and reveal the surface fine structure under it. When the surface of 1% Tween 20 NanoSuit were covered with a thin layer of gold by spattering, which interfered with the electron beam penetration, drastically changed the high magnification image (e). The alternating pattern of furrows and ridges was no longer visible in SEM, although in TEM images the ridges were still clearly present (f). Arrows indicate the presence of gold.

Fig. 9
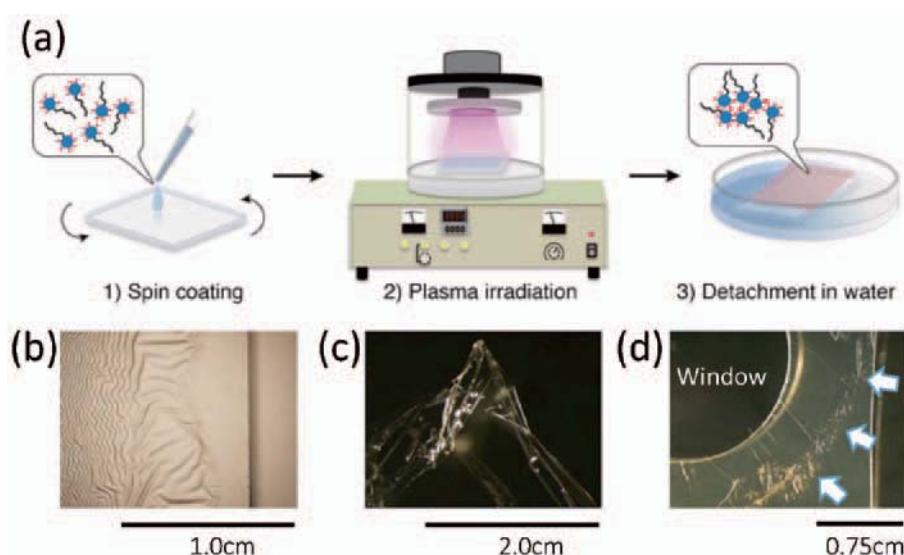
Preparation of the free-standing biomimetic ECS film by plasma irradiation. Schematic illustration of the preparation method (a). A water-soluble layer onto a glass substrate becomes a water-insoluble film upon plasma irradiation. Photographs of the plasma- treated film (b), the free-standing film removed from glass substrate (c) and the self-standing film on a plastic window after natural drying (d). Arrows indicate the end of the self-standing film.

film was controlled by adjusting several points; the electrical potential, the irradiation time, the distance to the irradiated surface, the concentration of the solution, and the spin-coating conditions.

These films showed both typical polymer properties and a unique out-of-plane molecular density gradient from the irradiated to the unirradiated film surface. Thin sections stained with toluidine blue revealed that the thickness of the freestanding film was approximately 10 μm. The staining was localized strongly at the plasma irradiated surface, because toluidine blue has a positive charge and binds selectively to negatively charged sites. It has been proposed that because air-derived plasma contains oxygen, negatively charged carboxyl and hydroxyl groups are localized on the irradiated surface. This was confirmed by X-ray photoelectron spectroscopy, suggesting that the irradiated surface was caused by the generation

of carboxyl groups by surface oxidation. The freestanding films exhibited other typical properties, such as pH stability, transparency, a pinhole-free surface, and flexibility. The film was insoluble in solutions across a pH range of 3-10, although it dissolved in strong acids or bases, because the covalent bonds of the polyethylene glycol chains decomposed. The transparency of the Tween 20 film was greater than 95%. In addition, these films exhibited a unique structural feature. The atomic force microscopic images show that the irradiated surface of the Tween 20 film was uniform and smooth (**Fig. 10**(a)), whereas the unirradiated surface of the film was rough (Fig. 10(b)). The TEM images confirmed these morphological features, and also revealed an electron density gradient from the irradiated to the unirradiated surface (Fig. 10(c)). Energy dispersive X-ray (EDX) spectroscopy also showed an osmium concentration gradient between the irradiated and the unirradiated surfaces (Fig. 10(d)).

Fig. 10
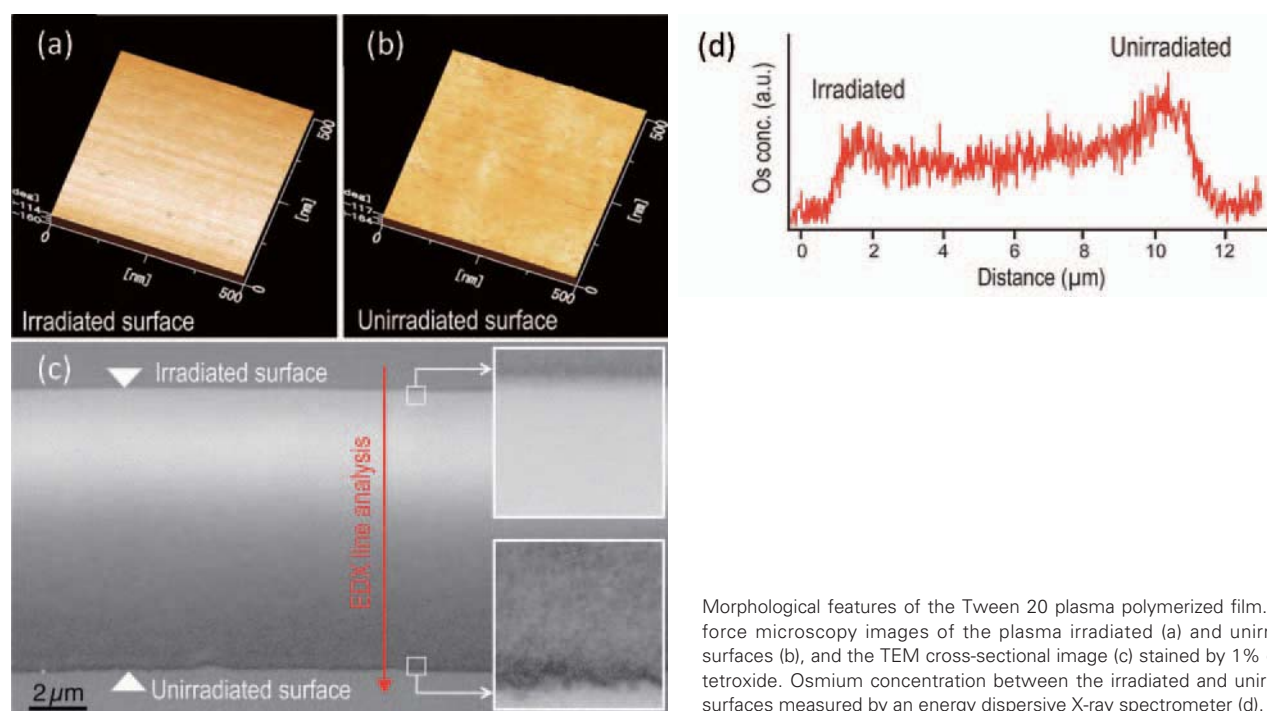
Morphological features of the Tween 20 plasma polymerized film. Atomic force microscopy images of the plasma irradiated (a) and unirradiated surfaces (b), and the TEM cross-sectional image (c) stained by 1% osmium tetroxide. Osmium concentration between the irradiated and unirradiated surfaces measured by an energy dispersive X-ray spectrometer (d).

This may be because the OsO_4 stain, which binds strongly to the low-density polymerized domains, accumulated toward the unirradiated surface of the film. The difference was enhanced by the extent of the polymerization, particularly the cross-linking of the polyethylene glycol chains. Thus, the freestanding thin films showed an out-of-plane molecular density gradient from the irradiated surface to the unirradiated surface. The fabrication of freestanding films has so far remained complex and challenging. Most methods involve the secondary processing of polymers, such as layer-by-layer (LBL) absorption of polyelectrolytes [19, 20], or filtration of nanofibrous materials [21-23]. Our freestanding thin films were formed by a simple one-step polymerization, and showed both typical polymer properties and a unique out-of-plane molecular density gradient from the irradiated to the unirradiated film surface.

Table 1 summarizes the freestanding films prepared from precursors with Polyethylene glycol chains (1-9); multiple hydrophilic groups (10-28); a single hydrophilic group (29-34); several double bonds (35-41); and an imidazolium ring typical of ionic liquids (42-46). All the freestanding films were insoluble in both water and ethanol. These results suggest that the radicals generated by the plasma promoted polymerization of both the common polymerizable functional groups, such as alkenes, and the hydrophilic groups, such as Polyethylene glycol chains, carboxyl, and hydroxyl groups, on the irradiated surface.

To investigate the surface-shielding effect of those films for organisms in high vacuum, we fabricated various biomimetic ECS films on the surface of mosquito larvae (*A. albopictus*). These organisms normally collapse and die from rapid dehydration under high vacuum conditions (10^{-3}-10^{-5} Pa) in an FE-SEM (Fig. 1(c)). The films made the larvae highly tolerant to the high vacuum. In addition, as in the case of Tween 20, high-resolution images of the film-coated living organisms were obtained when we use the chemical compound shown in Table 1 (see, **SEM

observation of living organisms). Other compound could not observe the fine structures or keep the life of the animal.

Discussion

In order to observe living organisms by conventional SEM in high vacuum, there are two major problems to solve: how to produce a sufficiently thin barrier of gas and/or liquid through which to observe surface fine structure; and how to increase the electric conductivity of the surface of the animal, without any toxicity or damage to the living tissues. Recent research to improve techniques such as low-vacuum scanning electron microscopy [21] and use of an environmental scanning electron microscope (ESEM) have been developed [22]. However, although both are elegant techniques, low-vacuum SEMs allow semi-wet samples to be imaged without coating but are unable to attain the resolution of conventional SEMs. ESEMs, being wet or contained in low vacuum or gas, also can be used to observe specimens without coating and produce better images than a low-vacuum SEM. However, it is not reliable enough to investigate the movements of living organisms at this level of resolution. We previously found that, with the assistance of a polymerized thin film NanoSuit, organisms possess the potential to tolerate high vacuum environments without any electrical charges [5]. The advance that we have made is to preserve life in high vacuum long enough to observe active movements of living specimens and at good resolution. The reason for improved clarity in fine structure seen with living specimens is due to a surface shield effect (SS-effect) caused by the thin NanoSuit® film on the surface of the animal *in vacuo*.

In the present research, in addition to the apparent barrier effect, no electrostatic charging was observed on any of the animals during their active movements. Animals treated in distilled water alone showed electrostatic charge build-

Table 1

Sample	Monomer	Polymerization site	Solvent	State*
1	Tween 20** a)	PEO chain	Water	◎
2	Tween 40 a)	PEO chain	Water	◎
3	Tween 60 b)	PEO chain	Water	◎
4	Tween 80 a)	PEO chain	Water	◎
5	Brij 35** a)	PEO chain	Water	◎
6	Triton X-100** c)	PEO chain	Water	◎
7	Poly(ethylene oxide) c)	PEO chain	Water	◎
8	Pluronic F-127** c)	PEO chain	Water	◎
9	Pluronic F-68 c)	PEO chain	Water	◎
10	Lecithin (from soy bean) d)	Multiple OH	Ethanol	◎
11	Tannic acid c)	Multiple OH	Ethanol	◎
12	Tetraethoxysilane b)	Multiple OH	Ethanol	◎
13	Span 20 b)	Multiple OH	Ethanol	◎
14	D-Maltose b)	Multiple OH	Water	◎
15	Trehalose C12 e)	Multiple OH	Water	◎
16	D-Glucose a)	Multiple OH	Water	◎
17	n-Dodecyl-β-D-maltoside** c)	Multiple OH	Water	◎
18	MEGA-8** c)	Multiple OH	Water	O
19	CHAPS** c)	Multiple OH	Water	O
20	D-Trehalose b)	Multiple OH	Water	O
21	Sodium cholate** e)	Multiple OH	Water	O
22	n-Octyl-β-D-glucoside** c)	Multiple OH	Water	O
23	Inulin b)	Multiple OH	Water	△
24	Pullulan b)	Multiple OH	Water	△
25	D-Sorbitol b)	Multiple OH	Water	△
26	L-Tyrosine a)	Multiple OH	Water	△
27	L-Glutamic acid a)	Multiple OH	Water	△
28	L-Aspartic acid a)	Multiple OH	Water	△
29	Lauric acid b)	Single OH	Ethanol	O
30	Stearic acid n-dodecyl ester b)	Single OH	Ethanol	O
31	Docosanoic acid b)	Single OH	Ethanol	O
32	L-Proline a)	Single OH	Water	△
33	L-Lysine a)	Single OH	Water	△
34	L-Histidine a)	Single OH	Water	△
35	Linolenic acid b)	OH & C=C double bond	Ethanol	◎
36	Linoleic acid b)	OH & C=C double bond	Ethanol	◎
37	Oleic acid b)	OH & C=C double bond	Ethanol	◎
38	Erucic acid b)	OH & C=C double bond	Ethanol	◎
39	Methacroylcholine chloride b)	OH & C=C double bond	Ethanol	◎
40	L-Glutamine a)	OH & C=C double bond	Water	O
41	L-Arginine a)	OH & C=N double bond	Water	O
42	1,3-Diallylimidazolium bromide d)	C=C double bond	Ethanol	◎
43	1,3-Diallylimidazolium tetrafluoroborate d)	C=C double bond	Ethanol	◎
44	1,3-Diallylimidazolium bis(trifluoromethanesulfonyl)imide d)	C=C double bond	Ethanol	◎
45	1-Butyl-3-methylimidazolium tetrafluoroborate d)	C=C double bond	Ethanol	O
46	1-Butyl-3-methylimidazolium bis(trifluoromethanesulfonyl)imide b)	C=C double bond	Ethanol	O

* ◎: Large, thick, stable film O: Small, thin, stable film, △: Unstable film   ** SEM observation of living organisms
a) Wako Pure Chemical Co., b) Tokyo Kasei Kogyo Co., c) Sigma-Aldrich Japan Co., d) Kanto Chemical Co., e) Dojindo Co.

The summary of the freestanding films prepared from precursors with PEO chains (1-9); multiple hydrophilic groups (10-28); a single hydrophilic group (29-34); several double bonds (35-41); and an imidazolium ring typical of ionic liquids (42-46). All the free-standing films were insoluble in both water and ethanol. These results suggest that the radicals generated by the plasma promoted polymerization of both the common polymerizable functional groups, such as alkenes, and the hydrophilic groups, such as PEO chains, carboxyl, and hydroxyl groups, on the irradiated surface.

up quickly after they ceased moving. In contrast, charging commenced about an hour after movements ceased under NanoSuit® protection. Traditionally, biological samples are coated with ultrathin electrical conductors such as gold, palladium, platinum, or osmium, to prevent the accumulation of electrostatic charge at the surface [3]. The living specimens in the present study were observed at good resolution and with no electrostatic charging, which suggests that living organisms would have their own electrical conductors and/or possess certain properties on the surface which inhibit charging while they are good condition. The NanoSuit® seems somehow able to preserve life and to prolong the charge-free condition.

Until our discovery, most scientists believed that traditional viewing with the SEM is close to the true appearance of the surface of living animals. However the structures used NanoSuit® showed many differences from the images of the living specimens as shown in Fig. 6. These morphological differences apparently result from the presence of the NanoSuit® on the surface of the living animal providing the SS-effect. However, the differences suggest that, in the method presented here, the natural surface structure of the living organism is conserved and strongly supports the hypothesis that the NanoSuit® is able to preserve the "real life appearance" down to electron microscopic details.

At present, however, the NanoSuit component Tween 20 is not omnipotent. It is obvious that, other than the Tween 20 solution, much more suitable components must be found for each species to live longer in high vacuum. In the next paper, we

will show the suitable combination of chemical compounds for each living organisms.

It is also necessary to investigate whether or not the SS-effect is accomplished by a combination of different substances including unknown compounds which might be produced by the living animal itself. Nevertheless, it is apparent that the NanoSuit preserves the morphology of the living animal, decreasing the evaporation rate of gas and/or liquid and facilitate electrical conductivity in the electron beam. When the many intriguing aspects of the SS-effect have been resolved, it is easy to predict that this may be the start of a new era of improvement in the depth of our understanding not only in biology but also in many other fields of science.

Conclusion

We demonstrated here that the NanoSuit® plays an important role in keeping animals alive in the FE-SEM, a new method permitting the use of high vacuum and high resolution of innate fine structure with living specimens at high magnification imaging and no electrostatic charging in the SEM. This suggests that living organisms have the potential to tolerate high vacuum environments and possess their own electrical conductors and/or rely on certain properties on their surfaces to inhibit electrostatic charging. The NanoSuit prolongs the charge-free condition and increases survival time under vacuum. Since the NanoSuit® holds the organism surface faithfully intact with high resolution imaging, such a life barrier technique will be a desirable tool for all future work with SEMs to observe real images of living organisms with simpler, less time-consuming procedures, and should be suitable for numerous applications, especially in the biological sciences.

Acknowledgements

References

[1] Knoll M.; Aufladepotentiel und Sekundäremission elektronenbestrahlter Körper. *Z. Tech. Physik* **16**, 467 (1935).

[2] Small E. B. and Marszalek D.S.; Scanning electron microscopy of fixed, frozen, and dried protozoa. *Science* **163**(3871), 1064-1065 (1969).

[3] Suzuki E.; High-resolution scanning electron microscopy of immunogold-labelled cells by the use of thin plasma coating of osmium. *J. Microscopy* **208 (3)**, 153-157 (2002)

[4] Pease R.F., Hayes T.L., Camp AS, and Amer N.M.; Electron microscopy of living insects. *Science* **154**(3753), 1185-1186 (1966).

[5] Takaku Y., Suzuki H., Ohta I., Ishi D., Muranaka Y., Shimomura M. and Hariyama T.; A thin polymer, nano-suit, enhancing survival across the continuum between air and high vacuum. *Proc. Natl. Acad. Sci. USA* **110**(19), 7631-7635(2013).

[6] Ohta I., Takaku, Y., Suzuki H., Ishii D., Muranaka Y., Shimomura M and Hariyama T.; Dressing living organisms in a thin polymer membrane, a NanoSuit, for FE-SEM observation. *Microscopy* **63**(4), DOI: 10. 1093/jmicro/dfu015 (2014).

[7] Takaku, Y., Suzuki H., Ohta I., Tsutsi T., Matsumoto H., Shimomura M and Hariyama T.; A 'NanoSuit' surface shield successfully protects organisms in high vacuum: observations on living organisms in an FE-SEM. *Proc. R. Soc. B* **282**, 20142857 (2014).

[8] Chambers L., Woodrow S., Brown A.P., Harris P.D., Phillips D., Hall M., Church J.C. and Prichard D.I.; Degradation of extracellular matrix components by definedproteinases from the greenbottle larva Lucilia sericata used for the clinical debridementof non-healing wounds. *Br J Dermatol* **148**(1), 14-23 (2003).

[9] Sun K.H.; Effects of atomic radiation on high polymers. *Modern Plastics* **32**(1), 141-238 (1954).

[10] Yasuda H.; Glow discharge polymerization. *J Membr Sci* **16**(1), 199-293(1981).

[11] Friedrich J.; Mechanisms of plasma polymerization – Reviewed from a chemical point of view. *Plasma Process Polym* **8**, 783-802 (2011).

[12] FAO Toxicological evaluation of some food additives including anticakingagents, antimicrobials, antioxidants, emulsifiers and thickening agents. *FAO Nutr Meet Rep Ser* **53A**, 1-520 (1974).

[13] Morritt D.; Evaporative water loss under desiccation stress in semiterrestrial and terrestrial amphipods (Crustacea: Amphipoda: Talitridae). *J. Exp. Mar. Bio. Ecol*. **111**, 145-157 (1987).

[14] Ugolini A., Borgiolii G. Galaniti G., Mercatelli L. and Hariyama T.; Photoresponses of the compound eye of the sandhopper Talitrus saltator (Crustacea, Amphipoda) in the ultraviolet-blue range. *Biol. Bull*. **219**, 72-79 (2010).

[15] Suzuki H., Takaku Y., Ohta I., Ishii D., Muranaka Y., Shimomura M. and Hariyama T.; In Situ preparation of biomimetic thin films and their surface-shielding effect for organisms in high vacuum. *Plos One* **8**(11), e78563 (2013).

[16] Jiang C,, Markutsya S. and Tsukruk V.V.; Compliant, robust, and truly nanoscale free-standing multilayer films fabricated using apin-assisted layer-by-layer assembly. *Adv Mater* **16**, 157-161 (2004).

[17] Mitzi D.B., Kosbar L., Murray C.E., Copel M. and Afzali A.; High-mobility ultrathin semiconducting films prepared by spin coating. *Nature* **428**, 299-303 (2004).

[18] Decher G. and Schlenoff J.; Multilayer thin films: Sequential assembly of nanocomposite materials; Wiley-VCH: Weinheim, Germany (2011).

[19] Decher G. Fuzzy Nanoassemblies: Toward layered polymeric multicomposites. *Science* **277**, 1232-1237 (1997).

[20] Quinn J.F., Pas S.J., Quinn A., Yap H.P., Suzuki R., Tuomisto F., Shekibi B.S., Mardel J.I., Hill A.J. and Caruso F.; Tailoring the chain packing in ultrathin polyelectrolyte films formed by sequential adsorption: Nanoscale probing by positron annihilation pectroscopy. *J Am Chem Soc* **134**, 19808-19819 (2012).

[21] Symondson W. O. C. and Williams I. B.; Low-vacuum electronmicroscopy of carabid chemoreceptors: a new tool for the identification of live and valuable museum specimens. *Entomol. Exp. Appl*. **85**, 75-82 (2003).

[22] Danilatos G. D.; Review and outline of environmental SEM at present. *J. Microsc*. **162**, 391-402 (1991).

Serial Block Face Scanning Electron Microscopy Using the JEOL JSM-7100F with Gatan 3View 2XP at King's College London –UK

R. A. Fleck[1], G. Vizcay[1], G. Neves[3], F. W. Grillo[3], J. Burrone[3], M. Green[4], A. Bullen[2]

[1] Centre for Ultrastructural Imaging, King's College London
[2] Centre for Auditory Research, UCL Ear Institute
[3] MRC Centre for Developmental Neurobiology, King's College London
[4] Department of Physics, King's College London

In this article, we describe recent progress implementing serial block face scanning electron microscopy (SBF-SEM) using a Gatan 3View system on a JEOL Field Emission Scanning Electron Microscope. We show the versatility of the system and discuss best practice in preparing tissues for this technique and for post processing of data. Moreover, we describe a number of important technical improvements in the performance of the SBF-SEM, which we have implemented in partnership with JEOL and Gatan.

Introduction

High resolution imaging of cellular and molecular structure plays a critical role in biomedical research with transmission and scanning electron microscopy essential tools in the imaging arsenal. A cornerstone of recent advances in imaging has been to access three-dimensional (3D) structural information on many length scales. This is of central importance in biological research and has been accessible via established methods to resolve structures, which are in themselves defined by instrument resolution limits, e.g., molecules at atomic, organelles at electron microscopic (EM), tissues at light-microscopic and whole organisms at resonance tomography (e.g., MRI, PET-CT) scales.

However, a gap exists, when a 3D-tissue structure needs to be understood and reconstructed over hundreds of micrometres with a resolution sufficient to follow the thinnest cellular processes and to identify small organelles such as synaptic vesicles. That is to say EM resolution and EM ultrastructural detail over a spatial volume more commonly associated with low-resolution tomography (MRI, PET-CT) or intermediate-resolution 2-photon microscopy. Such 3D-data are, however, essential to understanding cellular networks. For example in the nervous system, tissue models of skin disease, models of invasion of pathogenic fungi in human tissue and models of complex multicellular tissues where changes act cumulatively across a wide spatial area to affect the performance of an organ or tissue (e.g., the auditory system). For these questions to be addressed and answered tissues need to be completely reconstructed throughout a substantial spatial volume.

3D Electron Microscopy for Large Volumes

Traditional methods of three dimensional electron microscopy for large volumes (greater than 200-300 nm), serial section electron microscopy and serial section electron tomography, require highly time and labour intensive preparation methods that are prone to loss of data through the loss of individual sections in preparation and imaging process. This has to date been performed almost exclusively by highly skilled operators, where sectioning and collecting serial sections of tissue with the number of sections (directly translating to resolution and size of the final 3D volume) being a measure of the operators skill and dedication.

Leighton proposed in the early 1980's that large volumes of sections may be obtained by sequential scanning electron microscopy (SEM) imaging of block faces, cut by a miniature microtome within the SEM (Leighton, 1981). However, despite discussing the potential of 3D information over extended scales and describing the use of such a miniature microtome able to function within the SEM specimen chamber to show successive cut faces of an Epon block of squid (*Loligo pealei*) fin nerve (Leighton, 1981), the computer processing power necessary for automation of the technique and reconstruction of the 3D volumes together with the available SEM technology at the time limited the practicality of the approach.

In recent times, building on the pioneering work of Leighton, serial block face scanning electron microscopy (SBF-SEM), has fast become established as a robust technique for the automated 3D imaging of large tissue volumes at high spatial resolutions.

>> London SE1 1UL, UK | E-mail: roland.fleck@kcl.ac.uk

SBF-SEM eliminated problems of traditional techniques by sequentially sectioning and imaging a sample block within the microscope (**Fig. 1**). This is achieved by placing a specially adapted stage incorporating an ultramicrotome inside the microscope chamber, and imaging the face of the block by secondary electron or backscatter detection methods. The technique as implemented currently was developed by Denk and Horstmann (2004) and was adapted into a commercial product by Gatan Inc., who market it as the 3View system. One of the key improvements which allowed Denk and Horstmann to establish the technique was the availability of variable pressure SEM's which allowed charge built up in the otherwise nonconductive block to be managed to the degree necessary to allow for distortion free imaging.

Other techniques have also been developed for automated large volume imaging in the SEM, of the most common and well-developed techniques are Array Tomography (AT) and Focused Ion Beam (FIB) milling. AT allows samples to be sectioned by ultramicrotomy and the sections, collected in order as a ribbon mounted on a conductive silicon-wafer, the ribbons are then viewed by SEM (Hayworth *et al.*, 2014). AT has been enhanced by the ATUMtome (RMC, USA) which employs a tape system to automate the serial sectioning process (**Fig. 2**), although it is still time consuming to section and to mount by hand large numbers of sections onto silicon wafers for SEM. Image acquisition must also be automated and for the SEM sophisticated software is required to track a common area across multiple sections and to control a number of the key SEM operations allowing programmed, sequential (in focus) imaging of serial sections coupled to a high precision x-y-z sample stage. JEOL support such automation via SEMSupporter (https://www.u-inspector.com/ System In Frontier, Japan).

FIB milling of material in a SEM equipped with a conventional electron imaging source and a second ion milling source can also be used to generate 3D ultrastructural data over extended scales. This approach uses a focused beam of gallium ions to cut (mill) away layers of material (see; JEOL JIB-4600F). After each cut, the surface is imaged and progressively a stack of 2D images is acquired which can be aligned to generate a 3D volume. Although, offering high levels of spatial resolution, FIB is limited in the volume which can be realistically sectioned. In addition, challenges exist in registry between slices (affecting post processing of data), the contribution of gallium contamination of the sample and damage to structural information from the milling process.

SBF-SEM offers a technique which combines both the total automation of sectioning and imaging, as is found in FIB milling, and the ability to image very large volumes of data, similar to traditional serial sectioning and AT. In this paper, we discuss some of the improvements in SBF-SEM imaging we have made in collaboration with JEOL and Gatan Inc. on a JEOL 3View system, and the methods for reconstruction of 3D datasets post imaging with reference to a model tissue that produces particular challenges for SBF-SEM imaging, the organ of Corti of the mammalian cochlea.

Experimental
Animal tissue

Cochleae were obtained from C57/Bl6 and CBA/Ca mouse strains. All animal work was carried out in accordance with procedures licensed by the British Home Office and approved by University College London Animal Ethics committee.

Neural tissues were obtained from the hippocampus of C57BL/6J mouse strains (post-natal day 21). All animal work was carried out in accordance with procedures licensed by the British Home Office and approved by King's College London Animal Ethics committee.

Plant tissue

*Allium cepa* L. roots were obtained from cultivated onion bulbs grown for 7d in darkness.

Sample Processing

To prepare samples for SBF-SEM sufficient heavy metal contrast must be provided for the block surface to be imaged in

---

Fig. 1 JEOL JSM-7100F with Gatan 3View 2XP system.
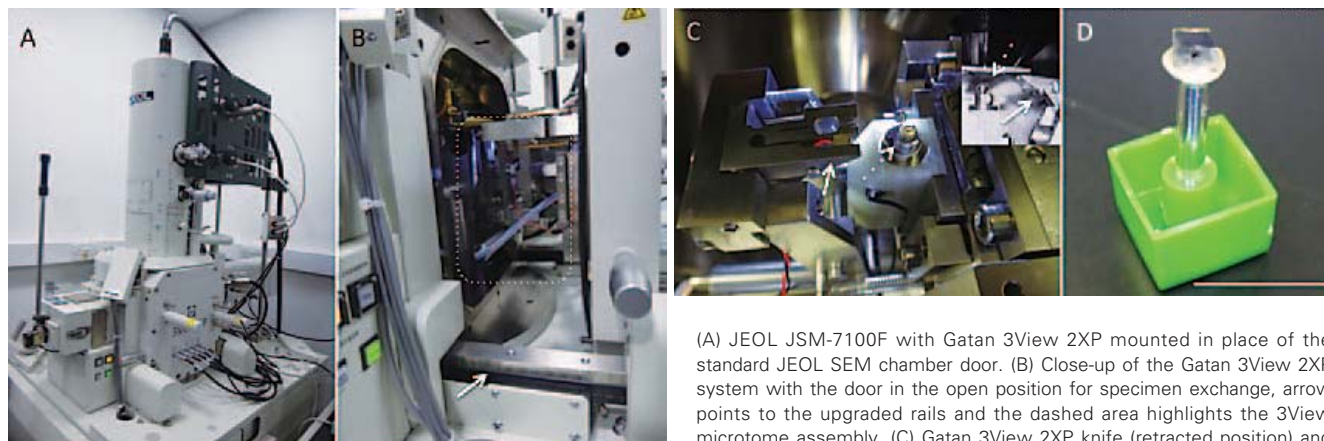
(A) JEOL JSM-7100F with Gatan 3View 2XP mounted in place of the standard JEOL SEM chamber door. (B) Close-up of the Gatan 3View 2XP system with the door in the open position for specimen exchange, arrow points to the upgraded rails and the dashed area highlights the 3View microtome assembly. (C) Gatan 3View 2XP knife (retracted position) and sample, solid arrow shows the knife, dashed arrow the sample, insert shows the knife and sample below the SEM pole piece. (D) 3View sample mounted on a specimen pin, scale bar represents 10 mm.

Fig. 2 RMC ATUMtome.
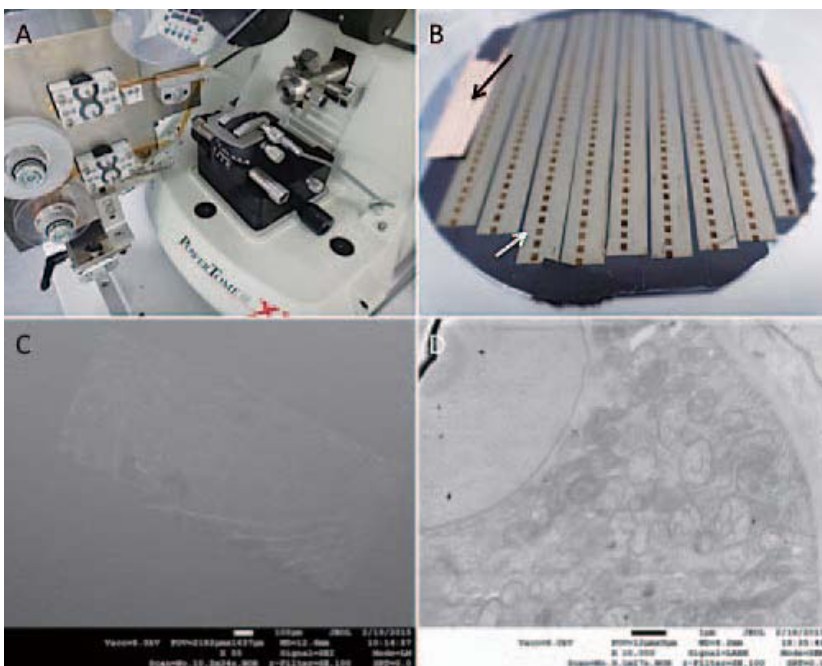
(A) ATUMtome tape automated serial section device mounted on an RMC PowerTome. (B) Sections collected in Kapton tape and mounted on a silicon wafer, black arrow highlights conductive tape added to improve conductivity of the surface, white arrow points to sections on a length of Kapton tape. (C) Secondary electron image of a single section on Kapton tape, scale bar represents 100 µm. (D) Backscattered electron image of tissue within a section mounted on Kapton tape showing multiple mitochondria and part of a nucleus defined by nuclear membrane, scale bar represents 1 µm. Images acquired using a JEOL JSM-7610F.

the SEM. One of the most commonly used protocols for SBF-SEM preparation is that of Deernick et al. (Deernick et al., 2010) in which the tissue is prepared following an OTO staining protocol (reduced osmium tetroxide-thiocarbohydrazide (TCH)-osmium tetroxide, Seligman et al., 1960) followed by en bloc staining with uranyl acetate and Walton's lead aspartate (Walton 1970). In addition for staining of mammalian tissue samples we have found the addition of the mordant tannic acid (Caceci and Frankum, 1987) either during or after fixation improves the contrast of membranous structures. Once suitably stained tissue is embedded in plastic resin following conventional protocols, SBF-SEM requires even fixation, contrasting and embedding throughout the large volume of tissue prepared for analysis. Precision and reproducible control of sample processing is key. To tightly and reproducibly control the physical dimensions of tissue with minimal mechanical damage to tissue, we use a Vibratome (VT 1200S, Leica-microsystems, Austria) with stereo magnification (×0.6-×4) to trim tissue where required prior to embedding.

Microscope System

The Gatan 3View 2XP system is installed in a JEOL JSM-7100F scanning electron microscope capable of variable pressure operation (30-300 Pa) in the laboratories of Dr Fleck at King's College London. This instrument has several unique features to aid SBF-SEM imaging. The standard JSM-7100F has been modified by JEOL to provide an improved door rail to support the additional weight of the 3View SEM chamber door and microtome (65 kg) permitting precise withdrawal and insertion of the 3View microtome and greater clearance between the SEM specimen chamber to provide more space for the operator to mount specimens and to aid door exchange. The JSM-7100F vibration isolation air bench can also be bi-passed to

lock the SEM column during specimen exchange.

Data collection by SBF-SEM is principally constrained by two opposed requirements: minimal exposure of sample to damage by the electron beam, against the need for better signal-to-noise provided by higher voltage and current. Physical as well as instrumental factors (working distance as well as aperture/beam/detector characteristics) affect the resolution obtained in practice.

Our laboratory has worked with JEOL and Gatan to further optimise variables within the microscope's sample chamber, in particular:

a) Improved detectors: we tested modified back-thinned PN-junction backscatter detectors with significantly improved signal-to-noise at low kV. Greater sensitivity combined with increased imaging speed improves data throughput when matched to an SEM able to deliver sufficient current at low kV. The JEOL FEG-SEMs deliver small probe diameter at high beam current (~2 nA in SBF-SEM conditions) at low kV (1-2 kV) by the use of an in-lens Shottky (FEG source) emitter and an angle control lens. Increasing probe current from 50 pA to 450 pA decreases dwell time from 5 µs to 0.5 µs while reducing image acquisition time from 84 s.image^{-1} to 8 s.image^{-1}.

b) Charge-suppression (in essence, biasing to reduce the interaction of the electron beam on the specimen) has been implemented in FEG-SEM's for a number of years, but not with SBF-SEM. We have completed initial testing of JEOL charge-suppression that demonstrates the feasibility of using such approaches to decrease beam-induced damage to the specimen whilst retaining sufficient beam energy to allow for high signal-to-noise data collection. We have shown reduction in charging and specimen damage during acquisition of a SBF-SEM

volume.

c) Shorter working distance (WD): reducing WD imparts an improvement in signal detection with a net improvement in signal to noise. It requires delicate adjustment of the SBF-SEM knife assembly with respect to the backscatter detector and SEM pole-piece. With Gatan and JEOL WD is now reduced from 6 mm to ~4 mm.

d) In-lens detectors which are common in high-specification FEG-SEM's, although are not available on the JSM-7100F at King's, offer significant benefits (improved signal-to-noise and remove the beam dwell time constrains of PN-junction type detectors) for SBF-SEM. They require and improve with shorter WD. Thus, combined improvements in SBF-SEM integration tested at King's offer considerable benefit to in-lens imaging of SBF-SEM samples.

The 3View 2XP system, under the control of the digital micrograph software, is capable of both montage and multiple Region of Interest (ROI) imaging so maximum information may be gathered for each cut made by the apparatus. The upwards movement of the stage into the imaging position after each cut ensures that the face of the block remains at the point of focus, so once aligned and focused on the block face the microscope can run without user interactions for potentially thousands of sections.

Results and Discussion

To illustrate the impressive imaging of the JEOL 3View system, a variety of cells and tissues have been used, prepared using optimised tissue processing procedures described above (**Fig. 3**). For 3D reconstruction, we show examples from recent work carried out on the organ of Corti, the sensory organ of the mammalian cochlea. The organ of Corti is a highly organised structure consisting of rows of sensory hair cells, which detect incoming sound vibrations. Vibrations cause movements of the Organ of Corti, which are detected by two classes of sensory hair cells; three rows of outer hair cells, which form part of an active amplifier in the cochlea, and the inner hair cell, which encodes the incoming sound as impulses at the auditory nerves, with extraordinary spatial and temporal fidelity. Surrounding these cells are several classes of supporting cells, which maintain the structure of the organ of Corti (**Fig. 4**). The images in this article are drawn from a collaboration between our laboratories to use SBF-SEM imaging to map the architecture of cells and other structures in the organ of Corti, and to understand how these highly specialised cells are adapted to their tasks.

Imaging

SBF-SEM requires samples to be embedded in plastic resin and mounted on metal pins designed for use with the 3View stage. The use of plastic resin in SBF-SEM has its own attendant difficulties, because the plastic acts as an insulator between the electron beam and grounded stage. Charging artifacts are therefore often problematic in SBF-SEM imaging, particularly when embedding complex tissue structures that may contain considerable voids filled with resin. The organ of Corti is a particularly good example of this; the tissue contains large fluid filled spaces, which when embedded form significant areas of 'blank' resin. In order to overcome the problems of charging, it is important that tissue is present throughout the block from the surface to the face of the block contacting the pin, to provide a conductance path through the block. Deernick et al. recommend painting a thin layer of silver paint around the base of the block and coating the block with a suitable thin metal coat before imaging (Deernick et al., 2010) and in our laboratory both gold and platinum coats have been used with success. The coating on the block's surface is removed by the microtome before imaging begins. Charging may also be improved by using a conductive epoxy to affix the block to the

Fig. 3 Images (various) from SBF-SEM.

Images of an outer hair cell (A) and detail from an inner hair cell (B) from the mouse organ of Corti. (C) hippocampus, neural tissue. (D) *Allium* root.
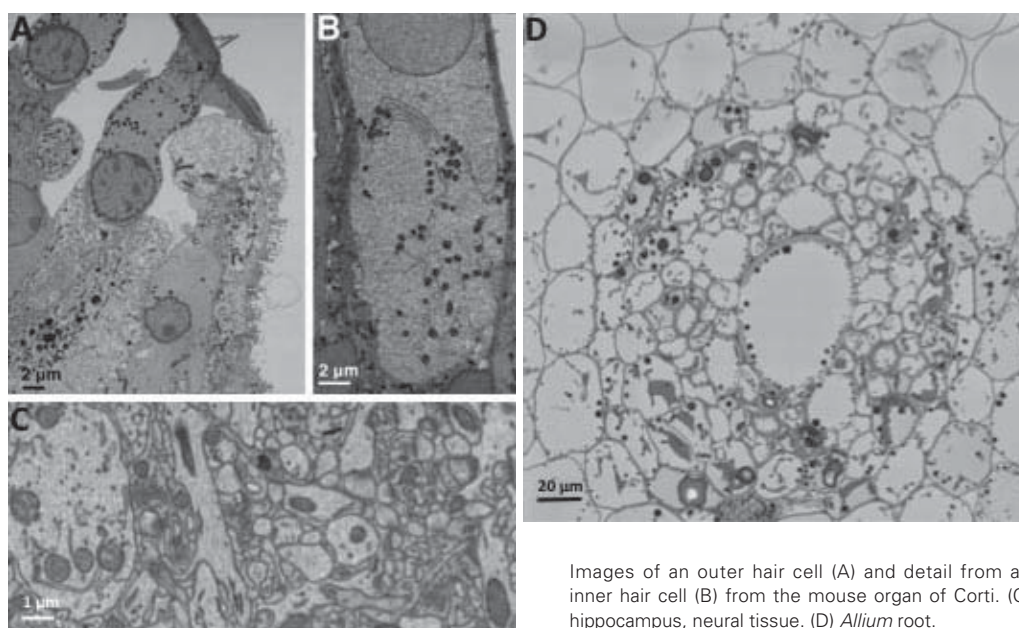
specimen-supporting pin. However, sample charging is likely to remain one of the most significant challenges in SBF-SEM imaging until the development of practical conductive resins for electron microscopy. In a recent patent application by Ellisman et al., (WIPO Patent Application WO/2015/009941) a highly conductive nanocomposite material is described (a polymer resin stabilized for conductivity with a conductivity stabilizer), which is compatible with SBF-SEM.

Charging may also be controlled by controlling imaging conditions, specifically the accelerating voltage, probe size and pixel dwell time of the beam. The modifications made to the JEOL 3View system are particularly advantageous in this respect. The higher signal to noise ratios conferred by decreasing the working distance and increasing the sensitivity of the backscatter detector, as well as the FEG-SEMs ability to deliver high beam current and small probe size at low voltages allow a reduction in accelerating voltage and pixel dwell time that decrease the energy put into the block by each imaging cycle leading to high resolution imaging. The charge suppression (bias) technology available in our system also improves the signal to noise ratio and allows imaging of samples where charging effects could not be ameliorated by other means (**Fig. 5**).

3D Reconstruction

Once images have been collected, they must be aligned before 3D reconstruction can begin. Hypothetically, SBF-SEM imaging should require no or minimal alignment, as the block remains stationary throughout the imaging process. However, effects of charging, and thermal changes to the block, can cause shifts in imaging position that require alignment. This may be achieved through several software solutions. The Gatan digital micrograph software that controls the 3View contains its own tools for image alignment and drift measurement, or external software packages may be used. For our images, we use the serial section alignment tools included in etomo, part of the IMOD package developed for electron tomography by The Boulder Laboratory for 3-D Electron Microscopy of Cells at the University of Boulder, Colorado (Kremer et al., 1996). This package allows for automated section alignment with manual control and fine tuning (via the programme MIDAS) and allows the user extensive control over the methods used for image alignment, making it a highly adaptable solution for SBF-SEM images. Once alignment is completed, 3D models of the sample may be generated in a variety of ways. For fast visualisation of the sample, where detailed analysis is not required, a minimum intensity projection (MIP) of the image stack may be sufficient (**Fig. 6**), this method will produce an overview of the complete stack, and is particularly useful when broad tissue architecture encompassing very large areas must be examined. It is also useful for assessing the quality of a sample before proceeding to more time intensive reconstruction methods. MIP may be generated using a number of image processing software suites, we currently use Imaris (Imaris 8.1, Bitplane, Switzerland). However MIP projections are less informative when tissue is particularly dense, or when high resolution information is required.

The standard method of 3D reconstructions of such image stacks is by segmentation, that is defining objects either manually or automatically by drawing lines around them on the 2D XY images. These lines or 'contours' are then used to generate 3D meshes representing the objects in question. This produces 3D models from which quantitative information on shape, size and orientation can be drawn, however the process of producing such models can be highly time consuming. In recent years efforts have been directed towards increasing the automation of image segmentation, in both light and electron microscopy. These efforts have now produced several tools in standard use, however electron microscopy poses particular problems for the automatic segmentation of volumes, due to the relatively low signal to noise ratio (compared to fluorescence imaging) and the high information content of EM images. Despite this, several tools have been developed and incorporated into IMOD and other image analysis software packages. Much segmentation is still carried out in a manual or semi-automated manner however, and with the use of tools to speed drawing and

Fig. 4　Diagram of the organ of Corti.

Tectorial Membrane

Inner hair cell

Outer hair cells

Afferent nerve fibres

Tunnel fibres

Supporting cells

Habenula perforata
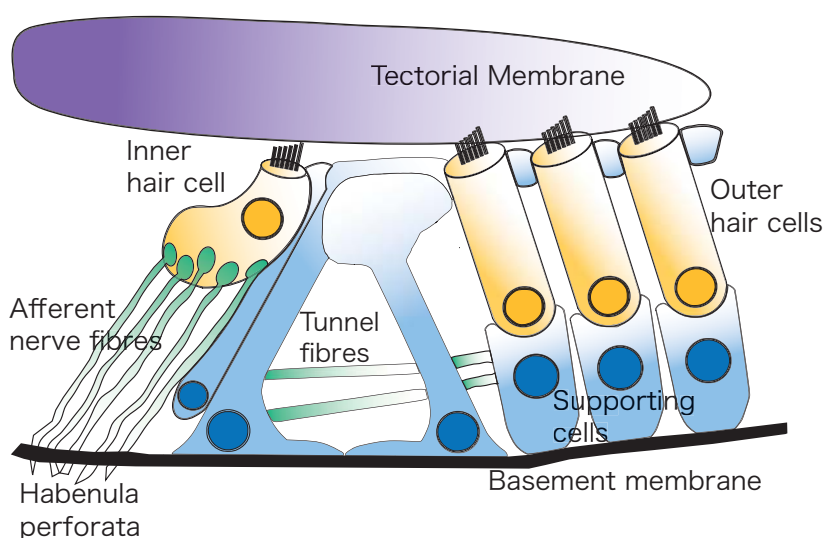
Basement membrane

Diagrammatic view of a longitudinal section of the organ of Corti. Three rows of outer hair cells and one row of inner hair cells are shown. The structure is supported by several classes of supporting cells. Movement of the basement membrane caused by sound vibrations moves the organ of Corti, creating shear stresses between the cells and the overlying tectorial membrane. These forces move the mechanosensitive stereocilia at the apex of the hair cells. The inner hair cells translate these movements into impulses at the afferent nerve fibres, which carry signals to the auditory nerves. The nerve fibres pass through the basement membrane at the habenula perforata region. Outer hair cells are also innervated, nerve fibres cross the organ of Corti as the tunnel fibres.

Fig. 5 Initial testing and evaluation of charge reduction with JEOL/ Gatan.
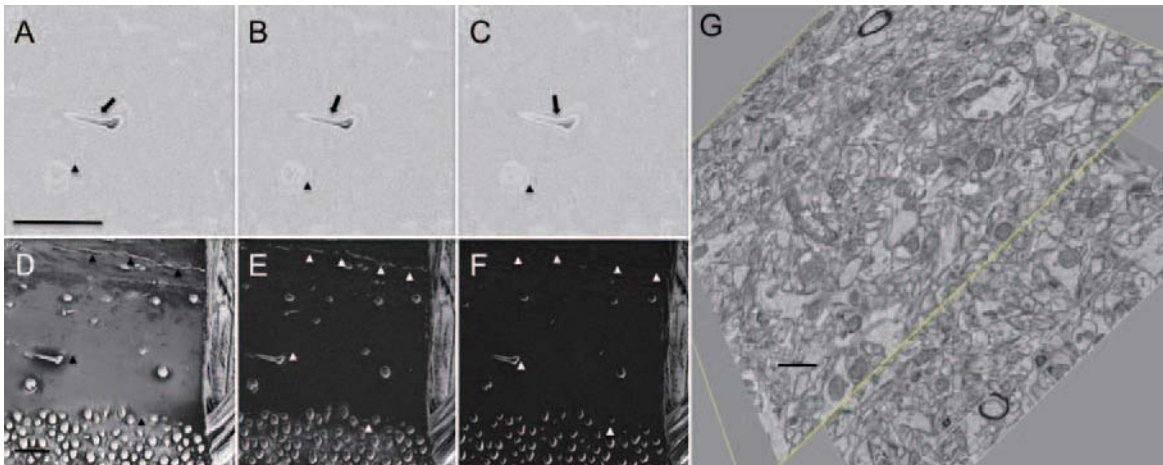
Backscattered electron detector signals showing decreased charge in resin voids at (A) No Charge Suppression, (B) Low Charge Suppression, (C) High Charge suppression. Arrows pointing to resin void in sample and progressive reduction in charge. Triangles indicate areas with reduced charge and improved signal to noise. Secondary electron detector signal showing decreased charge at (D) No Charge Suppression, (E) Low Charge Suppression, (F) High Charge suppression, Triangles highlight resin voids showing marked and progressive reduction in charge. The whole field of view is markedly less charged and more evenly contrasted (G) 200 section SBF-SEM stack was acquired at 2 kV under high charge suppression conditions with no beam induced damage or distortion visible in the 3D volume. Scale bars A-F = 40 μm, G = 1 μm.

Fig. 6 Minimum intensity projection of the inner hair cell region of the mouse organ of Corti.
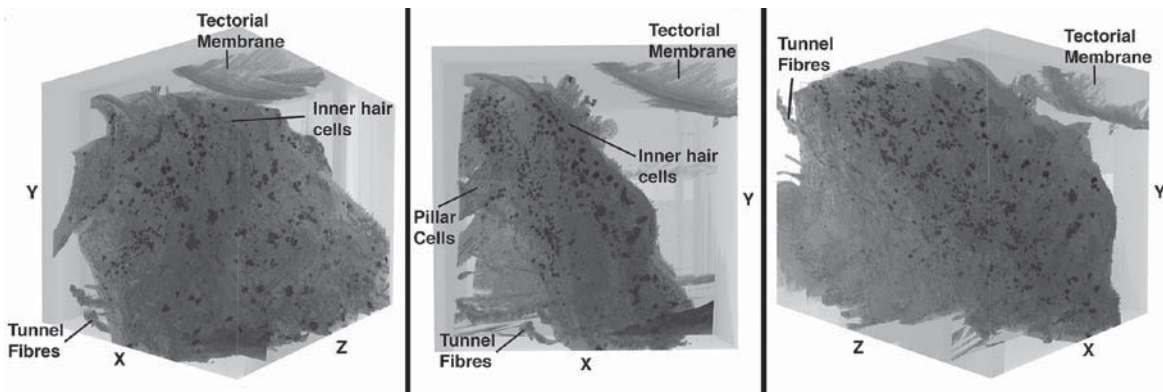
The structure is shown in the XY projection with organ of Corti structures labeled. Projections at a rotation of approximately 45° from the XY projection show the row of inner hair cells, the tectorial membrane and the projection of tunnel fibres through the organ of Corti.

Fig. 7 Reconstruction of the habenula perforata by manual segmentation.
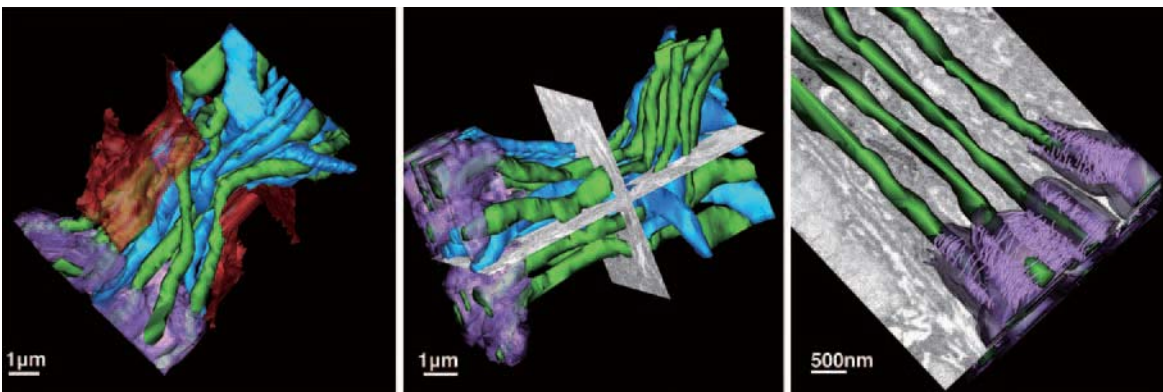
Nerve fibres (green and blue) are shown passing through a gap in the basement membrane (red) at the habenula perforata. Myelin (purple) is shown unwinding from the nerve fibres just before they pass through the basement membrane into the organ of Corti. Fibres with unwinding myelin visible in the image stack are shown in green, those without are shown in blue.

interpolate contours in regularly shaped objects reconstructions such as that shown in **Fig. 7** may be produced relatively quickly. These reconstructions may then be mined for quantitative information.

Although the process of image segmentation has been significantly speeded up by advances in segmentation software, the process is still too time consuming to be useful for producing large quantitative datasets over multiple samples, or for rapid assessment of potentially interesting structures. Stereology is a technique that has been used for some time as a method of assessing changes in samples over three dimensional datasets, but without requiring full reconstruction of the data. Point counting stereology, in which a grid of points is placed over the 2D XY image and the points categorised by what object they overlay, has been used by our laboratory for extracting quantitative data from SBF-SEM datasets. By placing grids at intervals throughout the image stack it is then possible to build up a numerical representation of the distribution of different objects throughout the cell, without having to reconstruct the objects themselves. This quantitative data may then be used to compare the number and distribution of cellular objects between, for example, control and treated samples. Although a stereology grid still requires a human expert to classify the points, data can be generated relatively quickly and it is possible to classify a relatively large number of cells. In our work, we have extended the use of stereology grid sets from cells as 3D objects; as the grid set as a whole represents the cell and the distribution of organelles within it, it is possible to obtain information on cell shape and the distribution of objects within a cell by manipulating the grid set as a 3D object and dividing data along axes of interest. An example of such a stereology grid set used in a recent data analysis is shown in **Fig. 8**. Although such analysis loses resolution from being performed on point sampled data sets rather than complete reconstructions, the speed at which such data can be gathered and therefore the number of points and cells that may be included in a single analysis allows for the production of statistically significant results.

Using these techniques for our studies of organ of Corti samples it has been possible to identify unique aspects of cellular architecture in hair cells and supporting cell classes, which had not been accessible by other imaging techniques. The generation of quantitative data from SBF-SEM data has allowed us to assess the prevalence of observed structural motifs across many cells. These results are now informing further studies into the structure-function relationships of sensory and supporting cells, and to examine the roles of cyto-architectural changes in pathological conditions.

Future Directions

The advantages of being able to image large tissue areas at electron microscopic resolution have made SBF-SEM a rapidly developing technique with potential applications across a range of life science fields. When considered with the present development of correlative light and electron microscopy (CLEM) techniques (Watanabe, Punge et al. 2011, Kukulski, Schorb et al., 2012, Muller-Reichert and Verkade 2012), the ability of SBF-SEM to image large volumes makes it a perfect complement to in vivo 2-photon microscopy (Briggman, Helmstaedter et al. 2011, Friedrich, Genoud et al., 2013) or super-resolution fluorescent microscopy (Kopek, Shtengel et al., 2012). Furthermore, by adapting the near infra-red branding technique developed by Bishop et al. (2011), it is possible to efficiently correlate in 3D between light and electron microscopy. In this way, complex 2 photon live cell studies can be performed and correlated to the underlying 3D ultrastructural information. SBF-SEM, by combining total automation of the sectioning and imaging process with the ability to image large volumes of tissue, earns a unique place in the space of imaging applications for biological samples and brings substantial essential added value to a wide range of cellular research.

The advent of automated large volume 3D electron microscopy techniques such as SBF-SEM has presented the field with a problem of big data similar to those faced by fields such

---

Fig. 8 Point counting stereology grid of an inner hair cell.
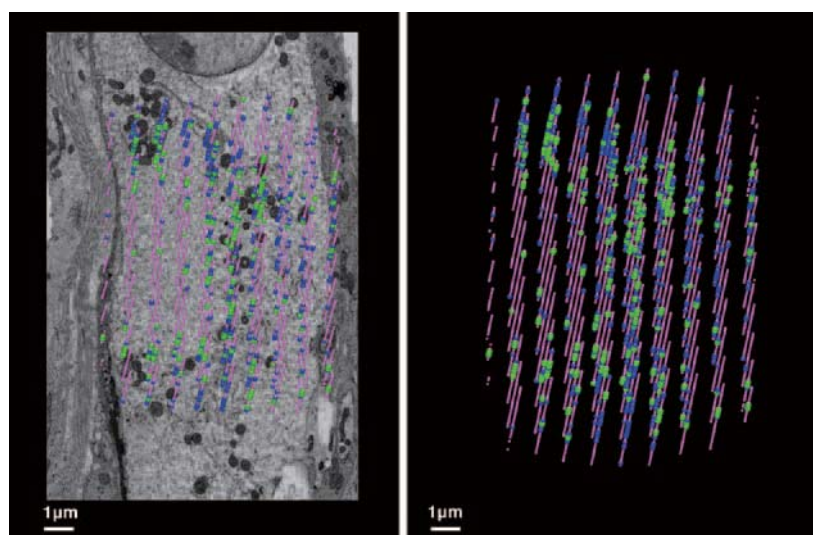
Stereology grid applied to an inner hair cell (left). Grids were used to plot the positions of internal membranes (blue) and mitochondria (green) in the cell. Pink spheres represent points that did not fall on a structure of interest. The sampled grid from the whole cell is shown on the right.

as genetics and proteomics. The problem is compounded in the imaging sciences, and in electron microscopy particularly, by the complexity of the computational tasks required for the analysis of such data automatically, the size of data (often extending into terabytes) required for large scale analysis of tissue areas, and the way data must be stored and handled in hardware for computation to take place. However, as the advantages provided by advances in fast I/O for storage devices and memory, disseminated processing (particularly the use of microprocessors other than the main CPU and the advent of practical cloud computing), and improvements in machine learning and machine vision are incorporated into image analysis software, this should bring rapid progress in the abilities of microscopists to extract the wealth of information produced by these techniques.

Conclusion

Seven months after installation of the JEOL SBF-SEM at King's College, we have demonstrated the capabilities of the instrument to perform at nm resolution in a variety of tissue types using a primary energy beam of between 1 and 3 kV delivered at high vacuum chamber conditions. Samples tested thus far include, Drosophila (brain and larvae); Various organs of the Zebrafish (*Danio rerio*); *C. elegans*; Algae (nanoparticle toxicity); Allium root (nanoparticle-formation); cell pellets and technically demanding cell monolayer preparations; mouse brain, forelimb bud, ear (hair cells and synaptic ribbons), skeletal muscle (neural junctions), cardiac muscle and tail skin; human liver and renal biopsy. SBF-SEM is positioned as a robust routine technique for the 3D investigation of tissues over at mm x-y-z scales with nm resolution.

Acknowledgements

References

(The following articles were referred to for this article as a whole.)

[1] Bishop, D., Nikić, I., Brinkoetter, M., Knecht, S., Potz, S., Kerschensteiner, M. and Misgeld, T. Near-infrared branding efficiently correlates light and electron microscopy. *Nat. Methods* **8**, 568-570. (2011)

[2] Briggman, K. L., M. Helmstaedter and W. Denk. Wiring specificity in the direction-selectivity circuit of the retina. *Nature* **471**(7337), 183-188. (2011)

[3] Caceci T. and Frankum K.E. Measurement of increased uptake of osmium in skin and in a gelatin model 'tissue' treated with tannic acid. *Journal of Microscopy*, **Vol. 147**, Pt 1, pp. 109-114. (1987)

[4] Deerinck, T.J, Bushong, E.A, Lev-Ram, V, Shu, X, Tsien, R.Y and Ellisman, M.H. Enhancing Serial Block-Face Scanning Electron Microscopy to Enable High Resolution 3-D Nanohistology of Cells and Tissues. *Micro.Microanal.* **16** (Suppl 2) (2010)

[5] Deerinck, T. J., Bushong, E., Thor, A. & Ellisman, M. H. NCMIR methods for 3D EM: A new protocol for preparation of biological specimens for serial block-face SEM. *Microscopy (Oxf)*, 6-8. (2010)

[6] Denk, W., and Horstmann, H. Serial block-face scanning electron microscopy to reconstruct three-dimensional tissue nanostructure. *PLoS biology* **2**, e329. (2004)

[7] Friedrich, R. W., C. Genoud and A. A. Wanner. Analyzing the structure and function of neuronal circuits in zebrafish. *Front. Neural Circuits*. **7**: 71. (2013)

[8] Hayworth, K.J., Morgan, J.L., Schalek, R., Berger, D.R., Hildebrand, D.G.C. & Lichtman, J.W. Imaging ATUM ultrathin section libraries with WaferMapper: a multi-scale approach to EM reconstruction of neural circuits. *Front. Neural Circuits*. **8**, 68. doi:10.3389/fncir.2014.00068. (2014)

[9] Kopek, B. G., G. Shtengel, C. S. Xu, D. A. Clayton and H. F. Hess. "Correlative 3D super resolution fluorescence and electron microscopy reveal the relationship of mitochondrial nucleoids to membranes." Proc Natl Acad Sci USA 109(16): 6136-6141. (2012)

[10] Kremer J.R., D.N. Mastronarde and J.R. McIntosh. Computer visualization of three-dimensional image data using IMOD. *J. Struct. Biol.* **116**:71-76. (1996)

[11] Kukulski, W., M. Schorb, M. Kaksonen and J. A. Briggs. "Plasma membrane reshaping during endocytosis is revealed by time-resolved electron tomography." *Cell* **150(3)**: 508-520. (2012)

[12] Leighton S.B. SEM images of block faces, cut by a miniature microtome within the SEM - a technical note. *Scan Electron Microsc*. **(Pt 2)**:73-6. (1981)

[13] Muller-Reichert, T. and P. Verkade. "Introduction to correlative light and electron microscopy." *Methods Cell Biol*. **111**: xvii-xix. (2012)

[14] Mikula, S., J. Binding and W. Denk. "Staining and embedding the whole mouse brain for electron microscopy." *Nat. Methods* **9(12)**: 1198-1201. (2012)

[15] Seligman AM, Wasserkrug HL, Hanker JS. A new staining method (OTO) for enhancing contrast of lipid-containing membranes and droplets in osmium tetroxide-fixed tissue with osmiophilic thiocarbohydrazide (TCH) *J. Cell Biol*. **30**: 424-432. (1966)

[16] Starborg, T., N. S. Kalson, Y. Lu, A. Mironov, T. F. Cootes, D. F. Holmes and K. E. Kadler. "Using transmission electron microscopy and 3View to determine collagen fibril size and three-dimensional organization." *Nat. Protoc*. **8(7)**: 1433-1448. (2013)

[17] Tapia, J. C., N. Kasthuri, K. J. Hayworth, R. Schalek, J. W. Lichtman, S. J. Smith and J. Buchanan. "High-contrast en bloc staining of neuronal tissue for field emission scanning electron microscopy." *Nat. Protoc*. **7(2)**: 193-206. (2012)

[18] Watanabe, S., A. Punge, G. Hollopeter, K. I. Willig, R. J. Hobson, M. W. Davis, S. W. Hell and E. M. Jorgensen. "Protein localization in electron micrographs using fluorescence nanoscopy." *Nat. Methods* **8(1)**: 80-84. (2011)

[19] Wilke, S. A., J. K. Antonios, E. A. Bushong, A. Badkoobehi, E. Malek, M. Hwang, M. Terada, M. H. Ellisman and A. Ghosh. "Deconstructing complexity: serial block-face electron microscopic analysis of the hippocampal mossy fiber synapse." *J. Neurosci*. **33(2):** 507-522. (2013)

Detailed Structural Characterization of Polymers by MALDI-TOFMS with a Spiral Ion Trajectory

Hiroaki Sato   National Institute of Advanced Industrial Science and Technology

Introduction

Detailed structural characterization of polymers is important because molecular properties of polymers strongly influence the material properties. Structural characterization of polymers have been performed by various instrumental analyses such as spectroscopic techniques (nuclear magnetic resonance spectroscopy: NMR, infrared spectroscopy: IR), chromatographic techniques ((pyrolysis-)gas chromatography: (Py-)GC , high performance liquid chromatography: HPLC, size exclusion chromatography: SEC), as well as mass spectrometry. Matrix-assisted laser desorption ionization time-of-flight mass spectrometry (MALDI-TOFMS) can observe molar mass of each polymer chain without fragmentation. Therefore, it exhibits its power for the determination of detailed polymer structures such as repeating units, end-groups, molecular weight distribution, and copolymer compositions. However, characterization of industrial complicated polymers such as copolymers and polymer blends are difficult by conventional MALDI-TOFMS, because a mass of polymer chains within complex polymeric materials increases the likelihood of isobaric interference, in which the peaks of different chemical compositions with the same nominal mass overlap. Peak separation of isobaric components requires high-resolution mass spectrometry. This report first describes brief features of high-resolution MALDI-TOFMS with a spiral ion trajectory, termed "MALDI spiral-TOFMS", and then some applications of MALDI spiral-TOFMS for a detailed structural characterization of complicated polymers are presented.

Fundamental: Time-of flight mass spectrometer with a spiral ion trajectory

The combination of a MALDI source and a time-of-flight mass spectrometer is better suited for mass spectrometry of the ions generated by pulsed laser irradiation. MALDI-TOFMS system is typically composed of a UV pulse laser, a MALDI source, a flight tube, and a detector. Ions generated by pulsed laser irradiation are accelerated by electrical potential between a target plate and a grid electrode about 20 kV. Accelerated ions are pushed into an electric-field-free flight tube and finally detected. When ions with mass m flight along with the flight tube with L (m) at a velocity of v (m/s), the flight time t (s) can be calculated as,

$$t = L / v \text{ .... (1)}$$

The velocity v can be obtained according to the law of conservation of energy,

$$ezV_0 = \frac{1}{2} muv^2 \text{ .... (2)}$$

or

$$v = 2ezV_0 / mu \text{ .... (3)}$$

where, z is a charge of ion, V_o is an accelerating voltage, e is the elementary charge (=1.6×10^{-19} C), and u is unified atomic mass unit (=1.66×10^{-27} kg), respectively.

The velocity v is substituted into eq. (1), giving,

$$t = L \sqrt{\frac{u}{2eV_0}} \times \sqrt{\frac{m}{z}} \text{ .... (4)}$$

Thus, the flight time t of ion is directly proportional to the square root of mass-to-charge ratio (m/z). To improve the resolving power, the flight time t should be elongated. Variable parameters in Eq. (4) are limited to the flight path L and the accelerating voltage V_o. Here, decreasing of V_o causes lowering of the efficiency of ion extraction and expands a variation of the initial velocity. Extension of the flight path L results in increasing size of instruments and loss of transparent ions caused by diffusion of ions. To overcome these problems, a new type of high-resolution TOFMS based on a spiral ion trajectory in a compact space has been developed. **Figure 1** shows a schematic of the ion optical system of a SpiralTOF™ mass spectrometer (JEOL JMS-S3000). This system has a long flight path of approximately 17 m (2.1 m × 8 turns) along the spiral ion trajectory within a compact space [1], [2]. Because ion beams are focused at every turns, loss of transparent ions can be prevented. As a result, spiral TOFMS can achieve a high mass-resolving power over 60,000 at full width at half maximum (FWHM) and provide high mass precision and accuracy at a milli mass unit.

〉〉 16-1 Onogawa, Tsukuba, 305-8569, Japan │ E-mail: sato-hiroaki@aist.go.jp

Structural characterization of polymers by MALDI-TOFMS

Polymer samples with a simple structure would give a series of peaks with regular intervals on the MALDI mass spectra. The m/z values observed on the MALDI mass spectra can be calculated according to Eq. (5),

$$m/z = M_{monomer} \times n + M_{end} + M_{cation} \quad \cdots \cdots (5)$$

where, $M_{monomer}$ is the mass of repeating unit, n is the numbers of repeating units, M_{end} is the mass of end-groups, and M_{cation} is the mass of cation (*e.g.* Na$^+$), respectively. $M_{monomer}$ can be determined by the peak interval and M_{cation} can be easily speculated from the used cationization reagents. Therefore, the end-group structures can be speculated from the mass M_{end}.

The chemical structures of a simple homopolymer can easily be determined by MALDI-TOFMS. However, most industrial polymers are complex materials such as copolymers, polymer blends, and composites. Furthermore, various additives such as flame-retardants, anti-oxidants, stabilizers, surfactants, pigments, and so on, are usually added to the industrial polymeric materials. A variety of chemical structures in the complicated polymer samples would give extremely intricate mass spectra observed by a conventional MALDI-TOFMS, resulting in increasing the likelihood of isobaric interference.

Peak separation of isobaric components within complicated polymer samples requires high-resolution mass spectrometry. One might thought that Fourier transform ion cyclotron mass spectrometry (FTICR-MS) would be useful to characterize such polymer samples. Although FTICR-MS is the most powerful tool for separating isobaric components at an ultrahigh resolution, it requires special skills for operation and careful maintenance of FTICR-MS, especially in the case of combination with a

MALDI source. Limitation of the amount of trapped ions in the ICR cell is a disadvantage for the measurements of polymer samples composed of various polymer chains. Furthermore, the requirement of long ion life-times (second level) to record long free induction decay (FID) signal would also be disadvantage for the detection of polymer ions generated by MALDI, because ion life-time of polymers by MALDI would be shorter than the FID recording time. The advantage of spiral-TOFMS over FTICR-MS is that high-resolution mass spectrometry can be readily performed using basically the same procedure as with conventional TOFMS instruments. This report describes representative applications of MALDI spiral-TOFMS for the characterization of complicated polymers.

Application of MALDI spiral-TOFMS for the structural characterization of copolymers

Copolymers are types of polymers composed of two or more monomers. To modify the properties and functions of polymeric materials, copolymers have been widely used in industrial materials. Improvement of copolymer materials has been accomplished by detailed characterization of copolymers, including copolymer composition and comonomer sequences, as well as end-group structures, molecular weights, and their distributions. This report presents the structural characterization of free radical polymerized methacrylate ester copolymers [3].

The sample used in this study is a copolymer composed of methyl methacrylate (MMA) and tartly butyl methacrylate (tBMA). This polymer was synthesized by free radical polymerization using 2,2-azobis(2,4-dimethylvaleronitrile) (AVN) as an initiator in ethyl lactate (EL) solvent acting as a chain transfer agent. Under this condition, polymerization would


Fig.1
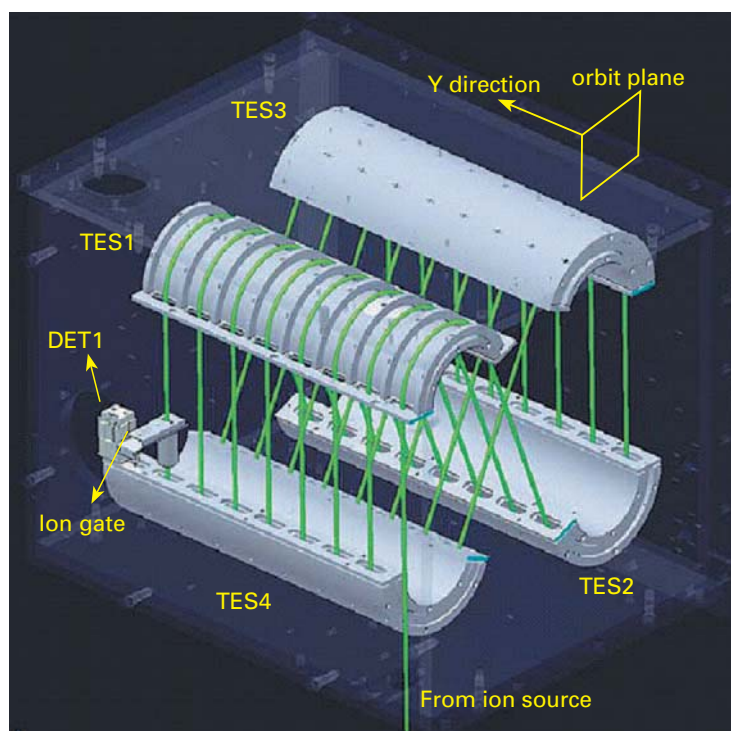
Spiral ion trajectory ion optical system. (Courtesy of JEOL)

start both from AVN initiator and solvent, resulting in two types of initial ends. The polymerization reaction would be terminated by disproportion resulting in saturated and unsaturated ends. As another termination, recombination of two radical chains would also occur. As a result, a total of seven different types of end-group combinations would be possible as shown in **Fig. 2**(a).

Figure 2(b) shows the high-resolution MALDI mass spectra of poly(MMA-*co*-tBMA) with a feed ratio of MMA/tBMA = 45/55 (mol/mol). This copolymer would be composed of various

polymer chains having different end group combinations and copolymer compositions. The peak resolution of about 60,000 by MALDI spiral-TOFMS could be achieved up to m/z 3000, and therefore, the isobaric peaks could be separated. From the obtained precious mass values, the combination of end-group and the copolymer composition of each component could be identified. For example, isobaric peaks observed around m/z 1218 could be separated. Among these, the peak at m/z 1218.714 could be assigned as the molecule composed of MMA/tBMA

Fig. 2

(a)

(b)
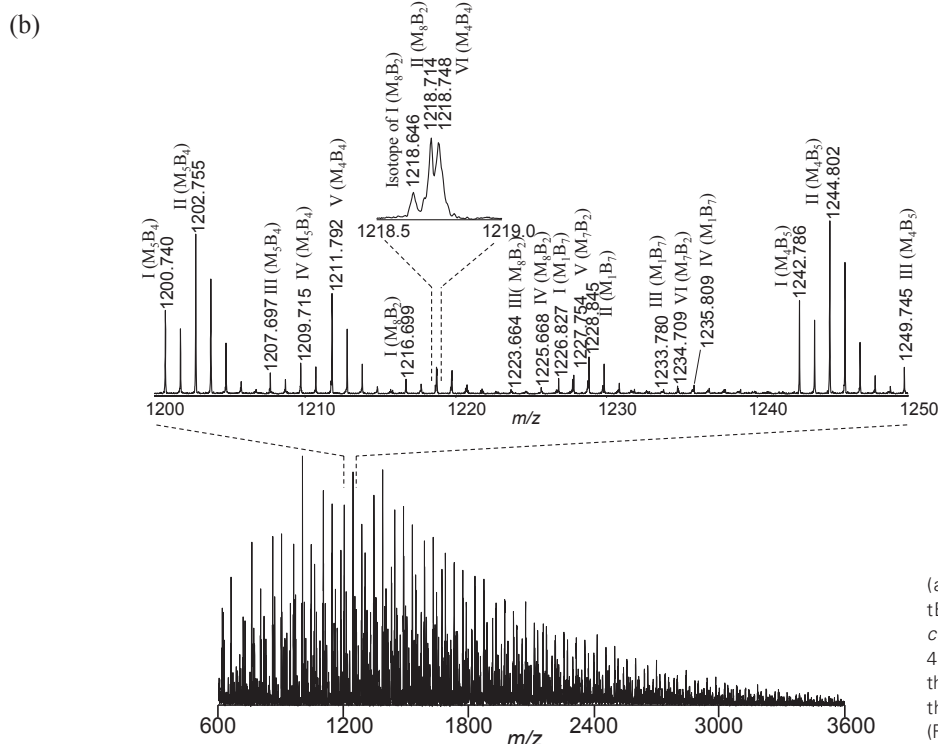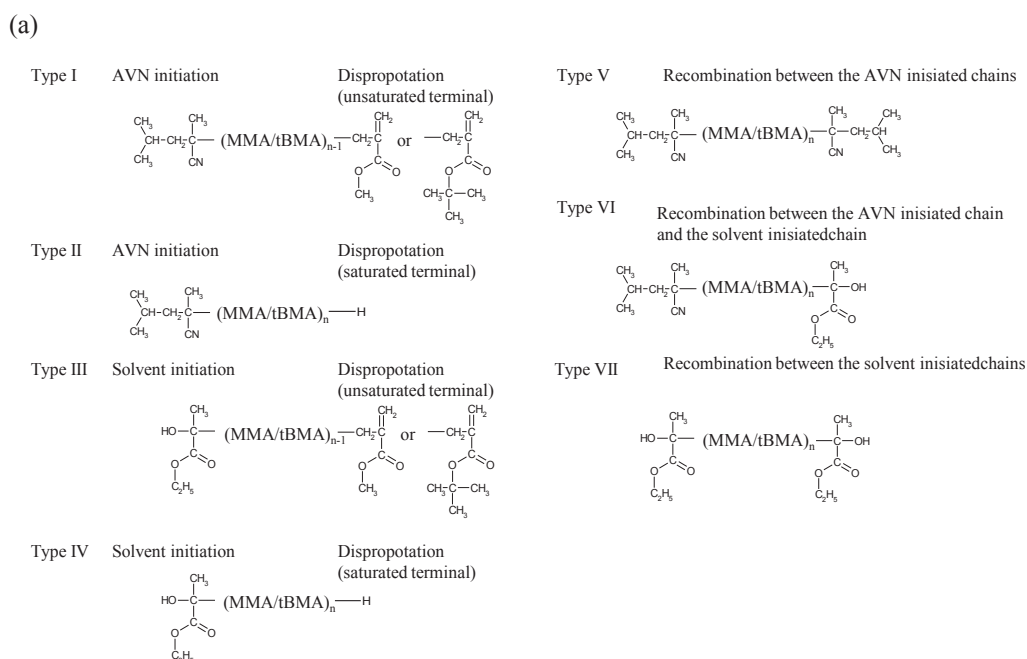
(a) Possible structures of poly(MMA-*co*-tBMA) and (b) mass spectra of poly(MMA-*co*-tBMA) with a feed ratio of MMA/tBMA = 45/55 (mol/mol). Roman numerals indicate the structure types in (a) and ($M_m B_n$) indicates the compositions of MMA and tBMA units. (Reprints with permission from ref. [3].)

= 8/2 units with type II end-group combination (AVN-initiated and saturated terminus), denoted as $II(M_8B_2)$. Similarly, the peak at m/z 1218.748 could be assigned as $III(M_4B_4)$ having EL initiated and unsaturated terminus. Here, the adjacent peak at m/z 1218.646 could be assigned as the isotope peak of $I(M_8B_2)$.

Figure 3 shows a comparison of expanded mass spectra of the poly(MMA-*co*-tBMA) with different copolymer compositions in the range of m/z 1226-1232. As for the sample with MMA/TBMA=12/88 (mol/mol), two components of $I(M_1B_7)$ and $II(M_1B_7)$ are mainly observed at m/z 1226.832 and m/z 1228.844. With rising MMA composition, the relative peak intensities of these components decrease, whereas the peaks of $III(M_7B_1)$ increase. The mass differences between these peaks have only ca. 0.08 Da. Conventional reflector type TOFMS could not separate such peaks as shown in the bottom figure, where three peaks of $I(M_1B_7)$, $II(M_1B_7)$, and $III(M_7B_2)$ were not discriminated. Therefore, the high resolving power of spiral-TOFMS should be needed for the precious peak assignments. The results obtained by MALDI spiral-TOFMS could give an insight into the mechanisms of copolymer synthesis based on the information such as bivariate distributions in copolymer composition and compositional distributions of the different end group combinations (data not shown , see Ref [3]). These results are difficult to obtain by other method, so, MALDI spiral-TOFMS is a powerful tool for the structural and compositional characterization of complicated copolymers.

Compositional analysis using Kendrick mass defect analysis

Although MALDI spiral-TOFMS is possible to characterize complicated polymers based on a complete peak assignment, it should deal with an enormous collection of peak data. Therefore,

an effective data processing method without relying on peak assignments is required. Here, this report describes "Kendrick mass defect (KMD) analysis" applied for the characterization of complicated polymers. KMD analysis is, in fact, an old technique proposed by Kendrick [4] in 1963, and it has been used chiefly to characterize petroleum and lipid samples by means of ultra-high-resolution FT-ICRMS. The KMD analysis, however, have not been applied for the polymer characterization, probably due to the limitation of the polymer measurements by MALDI-FT-ICRMS as described in the former section. The high resolving power of spiral-TOFMS, which can determine precious mass with a high-mass accuracy within a few ppm error, opens the way to KMD analysis in the field of polymer characterization. Here, this report explains the details of KMD analysis and several applications.

This has been proposed to discriminate homologous series differing only by a number of base units based on the "mass defect". Here, we consider the differences in nominal mass and accurate mass of various atoms containing in organic compounds. The accurate masses of hydrogen and nitrogen are larger than their nominal mass, whereas the masses of oxygen, sulfur, and phosphorus are deficient. In organic compounds, the mass of CH_2, corresponding to saturated hydrocarbons, shows the largest mass sufficiency. KMD is defined as the exact Kendrick mass subtracted from the nominal Kendrick mass.

The Kendrick mass (M_K) can be converted from the IUPAC mass (M_{IUPAC}) according to Eq.(6),

$$M_k = M_{IUPAC} \times \frac{nominal\ mass\ of\ base\ unit}{IUPAC\ mass\ of\ base\ unit} \cdots\cdots (6)$$

Originally, the methylene unit (-CH_2-) giving the maximum mass sufficiency is set as the base unit, i.e., *nominal mass of base unit* = 14 and *IUPAC mass of base unit* = 14.01565. In


Fig. 3

Comparison of the expanded mass spectra of poly(MMA-*co*-tBMA) with different copolymer compositions. The figures in the parentheses indicate the feed composition of (MMA/tBMA) in mol%. The bottom mass spectrum was observed using a conventional reflector type TOFMS.

polymer characterization, we set repeating unit of the polymer as the base unit.

Figure 4 explains the data processing procedures to make the KMD plot using a simple example. The sample of this example is a commercial detergent, which is a mixture of polyoxyethylene lauryl ether (C_{12}-PEO) and sodium dodecylbenzenesulfonate (LAS). The mass spectra of this detergent observed by MALDI spiral-TOFMS shows a distribution of the peaks of [M+Na]$^+$ ions of (C_{12}-PEO) over m/z 900 together with the peaks of LAS having different alkyl chain length (C_{11}-C_{13}). The observed m/z values were converted to M_K according to Eq. (6). In this case, ethylene oxide (EO) unit was set as the base unit (i.e. C_2H_4O = 44.0261 Da was converted to 44). For example, the peak observed at m/z 429.3181 was converted to 429.0634 in Kendrick mass scale based on EO unit. The M_K values consist of nominal and decimal parts. That is, 429 as nominal M_K and 0.0634 as KMD. A set of M_K and KMD of each observed peak was plotted on the two-dimensional graph (the KMD plot), where the components having common repeat units line up in the horizontal direction, whereas the components having different structures shift to the vertical direction. In this case, C_{12}-PEO chains having EO repeating units line up in the horizontal direction, whereas three LAS components having different numbers of CH_2 units line up obliquely.

The next application represents the case of more complicated samples. The samples of this application are different grades of commercial laundry detergents produced by the same company. **Figure 5** compares MALDI mass spectra and the KMD plots. Because several series of peak distributions have ca. 44 Da interval, it can be easily speculated that most components would contain the surfactants having EO repeating units. Setting EO unit as the base unit in KMD analysis, the m/z values of all observed peaks were converted to M_K, and the resulting nominal

M_K and KMD values were plotted. (Here, the KMD values in y-axis were omitted to avoid the specification of the samples). The general views of two plots are very similar, in which several lines distributing to the horizontal direction indicate that these detergents are the mixture of at least three different types of surfactants having EO units. By comparing two plots, it can be easily found out the differences in the chain length distribution of each components having EO chain. The EO chain length of the components in detergent B (for strong stain) seems to be longer than that in detergent A (for normal stain). Because a compound has a specific combination of KMD and nominal M_K values, the visual identification of each compound would be performed, if the database of KMD values of various compounds is prepared. Based on the plot patterns, one might be able to have an insight into a basic design concept of these detergents. If one has interests in specific lines in the KMD plots, then detailed structural characterization can be proceeded based on their precious masses of the corresponding peaks in the observed mass spectra. Thus, the KMD analysis would be useful for the extraction of characteristic compounds in a complex material.

Displaying the compositional distribution of copolymers on the KMD plot

The next application of the KMD analysis is relating to the characterization of copolymers [5]. **Figure 6** shows the mass spectra of a block copolymer composed of poly(ethylene oxide) and poly(propylene oxide) [P(EO-*b*-PO)]. A peak distribution can be observed with a maximum at *m/z* ca. 1900. The copolymers composed of EO and PO units theoretically give a peak series with ca. 2 Da interval corresponding to the mass differences in EO_xPO_y and $EO_{x+4}PO_{y-3}$, together with their isotope peaks. In this case, the monoisotope peaks of $EO_{x+4}PO_{y-3}$

Fig. 4

IUPAC mass: **429.3181**
^{12}C = 12 (by definition)

Kendrick mass:
$^{12}C_2{}^1H_4{}^{16}O$ = 44

$$429.3181 \times \frac{44}{44.0261} = 429.0634$$

Nominal Kendrick mass: **429**
Kendrick mass defect: **0.0634**

Polymers having EO units distribute in the horizontal direction.

The compounds having different repeating units line up obliquely

Explanation of the data processing procedures to make the KMD plot of a commercial detergent.

Fig. 5

(a) Detergent A

(b) Detergent B

Comparison of the KMD plots and original mass spectra of two different grades of commercial laundry detergents. The size of each dot indicates peak intensity. Note: the KMD values in y-axis were omitted to avoid the specification of the samples.

Fig. 6

Mass spectra of P(EO-*b*-PO). The broad-band mass spectrum (bottom) and the expanded mass spectrum in the range of *m/z* 1303-1313 (middle) and *m/z* 1307.7-1308.2 (top). Reprints from ref. [5] (open access).

should be accompanied with closely adjacent peaks of the second isotope (mainly due to $^{13}C_2$) of EO_xPO_y with only 0.027 Da differences as shown in Fig. 6. Spiral-TOFMS can resolve these peaks. The observed *m/z* values of all peaks were then converted to the M_K values based on PO unit (C_3H_6O, 58.0419 Da to 58), and plotted to make the KMD plot as shown in **Fig. 7**.

In the plot, the distribution of PO units line up in a horizontal distribution at intervals of 58. On the other hand, the distribution of EO units line up obliquely, where nominal M_K increases by 44 and KMD value increases by 0.0055. Theoretical lines of EO/PO compositions are also indicated in Fig. 7 as a guide. By reading the plot patterns, the compositional distribution of P(EO-*b*-PO) sample could be characterized, where EO distributes 0-35 units and PO distributes 13-23 units. The dots on the lines of EO = 0 indicated the existence of poly(propylene oxide) homopolymers. These results suggest that this polymer was synthesized by elongation of EO chains from the both ends of core poly(propylene oxide) chains.

The reports demonstrated that MALDI spiral-TOFMS made it possible to perform KMD analysis for polymer characterization. One of the key advantages of this method is that the KMD plot visually represents patterns in the structural distribution of a given polymer without the need to perform peak assignment or peak picking. This feature is potentially useful for high-throughput profiling (or typing) of industrially-produced polymers, to inspect how the polymer was made and processed.

Conclusions

MALDI-TOFMS would have seemed to ensure the strong position as a powerful characterization tool. Actually, however, complicated polymers have been difficult to be characterized by conventional MALDI-TOFMS instruments mainly due to insufficient resolution. The new type of TOFMS with a spiral ion trajectory (SpiralTOF™) has a potential to make a breakthrough in the characterization of complicated polymers. This report presented the features of MALDI spiral-TOFMS

and its applications for the characterization of complicated polymers. The first application was relating to the detailed structural characterization of copolymers. High-resolution mass spectrometry of spiral-TOFMS can avoid isobaric interference of the observed mass spectra, and it enables us to almost completely identify copolymer compositions and end-group combinations. The second application was the visualization of the high-resolution mass spectra composed of a huge numbers of peaks. By introducing KMD analysis, compositional distributions of complicated polymers such as blends and copolymers can visually be understood without any peak assignments. In conclusion, MALDI spiral-TOFMS has a great potential as a powerful tool for the structural and compositional characterization of complicated polymers.

References

[1] Satoh, T., Tsuno, H., Iwanaga, M., Kammei, Y.: The design and characteristic features of a new time-of-flight mass spectrometer with a spiral ion trajectory. *J. Am. Soc. Mass Spectrom*. **16**, 1969-1975 (2005).

[2] Satoh, T., Sato, T., Tamura, J.: Development of a high-performance MALDI-TOF mass spectrometer utilizing a spiral ion trajectory. *J. Am. Soc. Mass Spectrom*. **18**, 1318-1323 (2007).

[3] Sato, H., Ishii, Y., Momose, H., Sato, T., Teramoto, K.: Structural characterization of free radical polymerized methacrylate ester copolymers using high-resolution MALDI-TOFMS with a spiral ion trajectory. *Mass Spectrometry* **2**, A0014 (2013).

[4] Kendrick, E.: A mass scale based on CH2=14.0000 for high resolution mass spectrometry of organic compounds. *Anal. Chem*. **35**, 2146-2154 (1963).

[5] Sato, H., Nakamura, S., Teramoto, K., Sato, T.: Structural characterization of polymers by MALDI spiral-TOF mass spectrometry combined with Kendrick mass defect analysis. *J. Am. Soc. Mass Spectrom*. **25**, 1346-1355 (2014). Open access.

Fig. 7
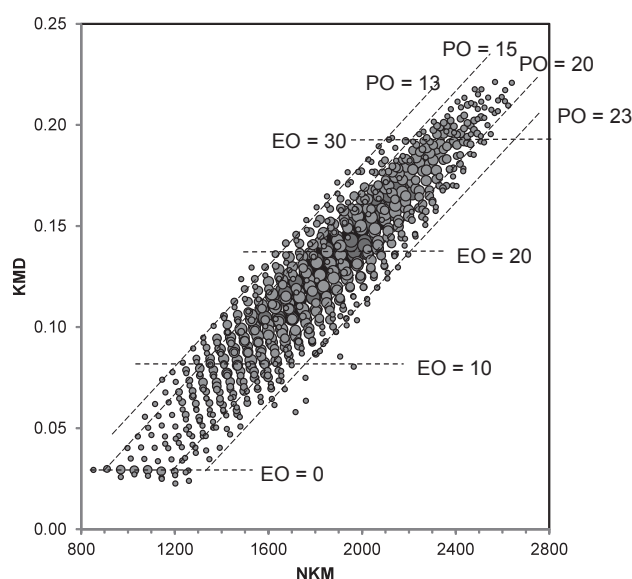
The KMD plot of P(EO-*b*-PO). The lines indicate the theoretical distribution of the homologue having the same numbers of EO or PO compositions. The size of each dot indicates peak intensity. Reprints from ref. [5] (open access).

^{13}C and ^{1}H Solid-state NMR of Proteins and Other Systems under Ultra-Fast MAS at 80-100 kHz and Beyond

Songlin Wang and Yoshitaka Ishii   Department of Chemistry, University of Illinois at Chicago

This article highlights a couple of drastic changes in the field of protein solid-state NMR (SSNMR) associated with ultra-fast magic-angle spinning (MAS) at 80 kHz or higher in a high magnetic field (^{1}H NMR freq. 750 MHz). We discuss how a traditional cross-polarization MAS (CP-MAS) scheme has been transformed into an efficient low-power RF scheme suited for high-field applications under ultra-fast MAS (UFMAS). We also discuss a nano-mole-scale SSNMR analysis of protein side chains by ^{1}H detection. It is demonstrated that ^{1}H-detected 2D and 3D SSNMR analyses are feasible for ~10 nmol of a stereo-selectively ^{2}H- and ^{13}C-labled ubiquitin within 2.5 h and 3 days at a spinning speed of 80 kHz. The data suggest that UFMAS approach is likely applicable to a variety of larger proteins.

Introduction

Although NMR spectroscopy is often considered as a matured field, recent development in high-resolution SSNMR has provided transformative improvements in its capabilities. High-resolution SSNMR using a CP-MAS scheme was originally introduced by Schaefer and Stejskal about 40 years ago using MAS at a spinning speed of 3 kHz for characterization of polymers and other organic systems [1]. Recent advances in hardware for fast MAS has dramatically increased the available spinning speed from 30 kHz to 100 kHz or higher during the past decade [2-6]. Despite initial concerns about a limited sample volume (≤1 μL) in a small MAS rotor having a diameter of 1 mm or less, SSNMR using UFMAS at 80 kHz or higher in an ultra high field has become a practical tool for structural biology. The advancement has been made through development of a series of sensitivity enhancement methods compatible with UFMAS such as ^{1}H indirect detection [7-10], paramagnetic assisted condensed data collection (PACC) [4], and other methods including isotope labeling [11, 12]. Thus, despite a limited sample volume, recent studies using UFMAS indicate sufficient sensitivity for a 3D SSNMR analysis of a limited amount of proteins. In this study, we present how basic building blocks of CP-MAS such as cross polarization (CP) and ^{1}H decoupling are evolved under UFMAS. We also present that a SSNMR microanalysis of proteins is possible through discussing our efforts to achieve side-chain signals assignments for a stereo-array-isotope labeled protein by ^{1}H-detected ^{13}C SSNMR under UFMAS.

Results and Discussion

Figure 1 shows a picture of three MAS rotors used in this study (left: 0.75-mm rotor; middle: 1-mm rotor; right: 2.5-mm rotor) in a comparison with a US one-cent coin so that the readers get some idea about the size of the samples we were using in UFMAS experiments to be presented in this study. Although a 2.5-mm rotor has been used for fast MAS experiments up to ~30 kHz spinning, it is clear that the dimensions of the 0.75-mm and 1-mm rotors are much smaller. Thus, it is natural that many in the NMR community were originally skeptical about the feasibility of multi-dimensional protein SSNMR experiments under UFMAS using such a small rotor.

Figure 2(a, b) shows a comparison of pulse sequences for (a) a CP-MAS scheme under UFMAS and (b) a traditional CP-MAS scheme. In a traditional scheme in (b), ^{13}C signals are acquired during high-power ^{1}H decoupling after polarization transfer from ^{1}H to ^{13}C spins by a CP. High-power RF decoupling typically requires a ^{1}H nutation frequency of 60-100 kHz, which exceeds the range of ^{1}H-^{13}C dipolar couplings (10-40 kHz). In a typical amplitude ramped (or adiabatic) CP scheme [13, 14], ^{1}H or ^{13}C RF-field strength is swept to match the following condition that

$$\langle v_{\mathrm{H}} \rangle - \langle v_{\mathrm{C}} \rangle = n v_{\mathrm{R}}, \cdots\cdots (1)$$

where $\langle v_{\mathrm{H}} \rangle$ and $\langle v_{\mathrm{C}} \rangle$ respectively denote the average nutation frequencies by ^{13}C and ^{1}H RF fields, v_{R} is the spinning frequency, and $n = \pm 1$ or ± 2. In contrast, in the pulse sequence for UFMAS in (a), ^{13}C signals are acquired under low-power ^{1}H decoupling at ~10 kHz [3, 6, 8, 15], as UFMAS eliminates a majority of line broadening due to ^{13}C-^{1}H dipolar couplings.

>> 845 W Taylor St. Chicago IL 60607, USA | E-mail: yishii@uic.edu

Since heat generated by an RF field is proportional to the square of the field strength, this scheme produces negligible sample heating compared with that by high-power ^{1}H RF decoupling. A low-power decoupling sequence also minimizes a hazard of probe arcing, which has been typical in SSNMR experiments. More importantly, a low-power scheme allows us to repeat CP-MAS experiments at a fast recycling rate that is matched to short ^{1}H T_1 values of some hydrated proteins or proteins incubated with paramagnetic dopants in the PACC scheme [4, 16]. Under UFMAS, a traditional CP condition defined in eq. (1) requires a very strong RF irradiation for which either of v_H or v_C exceeds 100 kHz. Thus, for the pulse sequence under a UFMAS condition in (a), a double-quantum CP (DQ-CP) pulse sequence [3, 4] is adopted with a matching condition of

$$\langle v_H \rangle + \langle v_C \rangle = |n| v_R. \cdots\cdots (2)$$

When $|n| = 1$ is selected, this generally guarantees a lower RF power as both $\langle v_H \rangle$ and $\langle v_C \rangle$ are less than v_R. Despite a common conception about the difficulties of CP under fast MAS, the CP efficiency of the DQ-CP scheme at a spinning speed of 80-100 kHz turns out to be comparable to that in a tradition MAS condition [3, 12]. Cares should be taken in an adjustment of

the CP as there are various conditions that can degrade a CP efficiency; for example, a rotary resonance condition $\langle v_H \rangle \sim v_R/2$ quenches ^{1}H spin polarization quickly during the contact time. Such "pitfalls" can be easily avoided by a careful two-dimensional grid search of the best CP efficiency using $\langle v_H \rangle$ and $\langle v_C \rangle$ as adjustable parameters. Thus, a renewed low-power CP-MAS scheme using low-power CP and decoupling sequences is now widely utilized as a standard pulse sequence for proteins and other organic molecules in the UFMAS condition.

Figure 3(a, b) shows 1D ^{13}C CP-MAS spectra of uniformly ^{13}C- and ^{15}N-labeled L-alanine (U-^{13}C, ^{15}N L-Ala) in (a) a low-power scheme using UFMAS at 100 kHz at a static B_0 field of 17.6 T (^{1}H NMR frequency of 750.1 MHz) and (b) a tradition scheme using MAS at 20 kHz at a static B_0 field of 9.4 T (^{1}H NMR frequency of 400.2 MHz). The data in (a) were obtained with a new JEOL 0.75-mm CPMAS probe installed at a 750 MHz SSNMR system at UIC. Clearly, the spectral resolution in (a) is higher than that in (b) obtained under high-power decoupling in a lower field. It is not trivial that low-power ^{1}H decoupling at ~10 kHz successfully removed residual dipolar couplings even in a high field in (a), considering that broadening is visible in (b) obtained with high-power ^{1}H decoupling at

Fig. 1
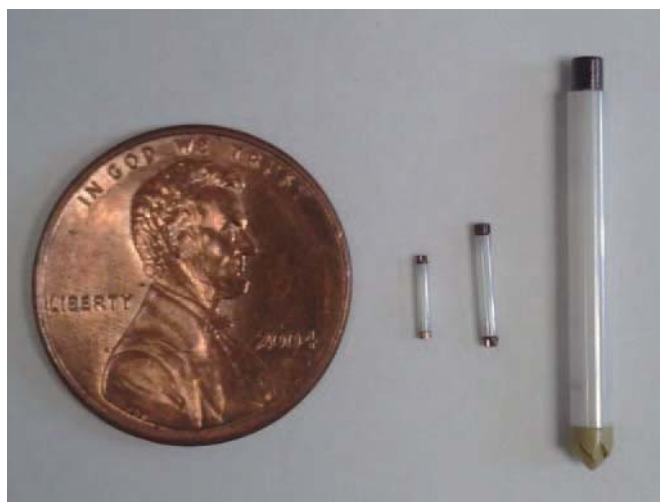
A picture of three MAS rotors used for this study in a comparison with a US one-cent coin. (Left) JEOL 0.75-mm rotor, (middle) JEOL 1-mm rotor, and (right) Varian 2.5-mm rotor.

Fig. 2
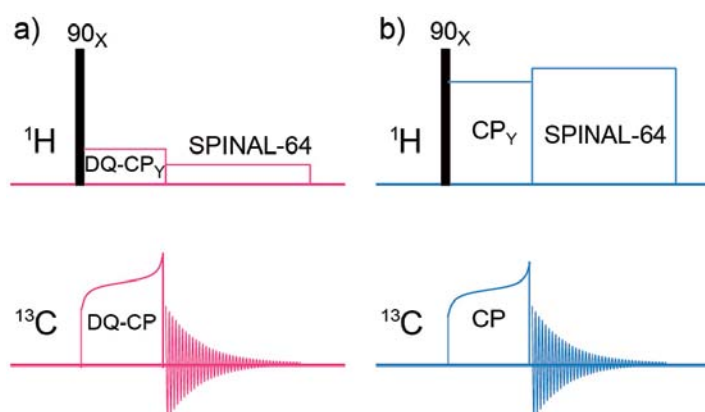
Pulse sequences of (a) a low-power CP scheme suited for a UFMAS condition and (b) a high-power CP scheme used for a conventional CP-MAS.
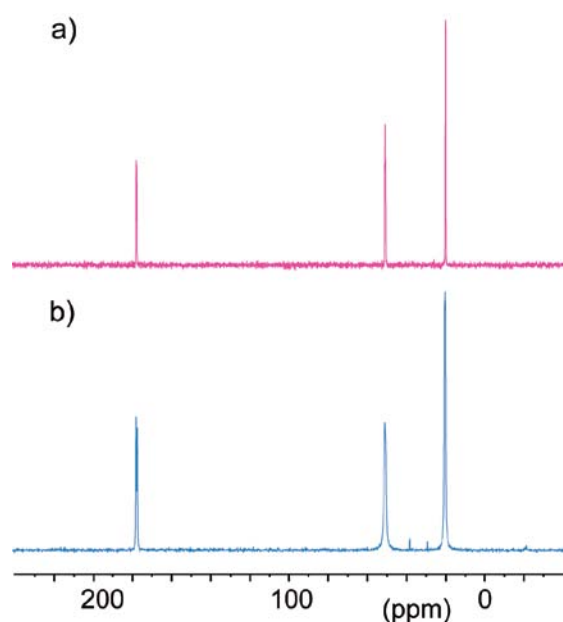
A comparison of ^{13}C CP-MAS spectra of uniformly ^{13}C-, ^{15}N-labeled L-alanine obtained with (a) a low-power decoupling scheme under UFMAS at 100 kHz in a high static magnetic field at 17.6 T and (b) a high-power decoupling under MAS at 20 kHz in a lower field at 9.4 T. The data were obtained with (a) JEOL 0.75-mm quad-resonance CP-MAS probe and (b) a home-built 2.5-mm triple-resonance CP-MAS probe equipped with a Varian 2.5-mm spinning module. In (a), ^{13}C signals were prepared with an adiabatic DQ-CP sequence in which the ^{1}H RF field strength was set to ~25 kHz while the ^{13}C RF field strength was ramped from 55 kHz to 95 kHz. The ^{13}C signals were acquired under low-power SPINAL-64 ^{1}H decoupling at 10 kHz. In (b), ^{13}C signals were prepared with an adiabatic CP sequence in which the ^{1}H RF field strength was set to ~75 kHz while the ^{13}C RF field strength was ramped from 40 kHz to 70 kHz. The signals were acquired under high-power ^{1}H TPPM decoupling at 85 kHz. The spectra were processed without any window functions. The sample amount is only 0.3 mg in (a) while that is 5.9 mg in (b); the sample in (b) was mixed with 5.9 mg of adamantine.

85 kHz. One more critical difference between UFMAS and traditional MAS approaches is an available sample volume. Under UFMAS at 80-100 kHz, the engineering needs limit sample amount to less than 1 mg. For example, in (a), only 0.3 mg of U-^{13}C, ^{15}N L-Ala was accommodated in a 0.75-mm MAS rotor with a sample volume of 0.3 μL while 5.9 mg of the sample was placed in a 2.5-mm rotor for (b) as a mixture with 5.9 mg of adamantane. Despite 20-fold difference in the sample size, the sensitivity in (a) was found to be approximately half of that in (b). It should be noted that the same number of scans (4 scans), recycle delays (3 s), and acquisition time (36 ms) were used for (a, b). Thus, the sensitivity per given sample amount (mass sensitivity) in (a) is ~10 times higher than that in (b), which was obtained in a traditional SSNMR approach using the lower field instrument. The excellent mass-sensitivity in the preliminary data in (a) is partly attributed to an efficient probe circuit of this JEOL 0.75-mm UFMAS probe. As highlighted in this example, a combination of a UFMAS probe and an ultra-high field has offered as much as 10-fold enhancement of mass sensitivity. The result signifies the importance of probe development in an ultra-high field for biomolecular SSNMR.

Next, we present an example of a SSNMR microanalysis for a protein sample. A traditional biomolecular SSNMR analysis by ^{13}C detection has typically required 0.3-1 μmoles of proteins for a 2D-3D analysis using ^{13}C SSNMR. Here, we have attempted to improve the sensitivity by employing ^{1}H-detected SSNMR and stereo-array-isotope labeling (SAIL). The SAIL approach was originally introduced to suppress line broadening due to germinal ^{1}H-^{1}H dipolar and scalar couplings for solution NMR of large proteins [17]. In this approach, all the CH$_2$ groups are stereo-selectively replaced by CHD while CH$_3$ groups are replaced by CHD$_2$. In this example, we employ SAIL proteins in order to enhance ^{1}H resolution and sensitivity of SSNMR under UFMAS by effectively removing strong ^{1}H-^{1}H geminal dipolar coupling. **Figure 4**(a) shows a ^{1}H-detected 2D ^{1}H/^{13}C chemical-shift correlation SSNMR spectrum for SAIL ubiquitin that was incorporated with 7 SAIL L-isoleucine (Ile). Despite a limited sample amount of ~55 nmol (~0.5 mg), the excellent spectrum was obtained only within 5 min. The ^{1}H line widths were 0.14–0.25 ppm and 0.10–0.22 ppm, respectively, with and without window functions. Interestingly, ^{1}H shifts allow us to separate a handful of CHD$_2$ signals, which cannot be well separated by ^{13}C shifts. As a result of the excellent resolution and sensitivity enhancement, the 2D experiment takes only 5 min. Thus, within a few hours, 2D data can be collected for ~10 nmol of the protein. Figure 4(b) shows a corresponding ^{13}C-detected 2D ^{13}C/^{1}H correlation spectrum of the SAIL-Ubq sample collected with the same experimental time. In the ^{1}H-detected 2D spectrum, the sensitivity was dramatically improved (by a factor of 5.4–9.7) (Fig. 4(a)) relative to the ^{13}C-detected 2D data (b), as shown from the comparison of the slices corresponding to the peaks indicated by arrows (d–g). In contrast to the excellent sensitivity, the corresponding ^{13}C-detected 2D spectrum in (b) had a much lower signal-to-noise ratio. Clearly, our approach allows for micro-SSNMR analysis of a protein sample in a short time.

We also confirmed that the sensitivity enhancement factors by ^{1}H-detected data in (d, e) relative to 1D ^{13}C CP-MAS in (c) for resolved ^{13}CHD signals at 24.5 ppm and ^{13}CHD$_2$ signals at 7.9 ppm (orange arrows) were 2.1 and 5.0, respectively. To the best of our knowledge, this is the first demonstration that ^{1}H-detected 2D ^{1}H/^{13}C correlation SSNMR for a protein sample is significantly more sensitive than 1D ^{13}C direct detection. In other words, no previous studies established advantage of ^{1}H indirect detection method over traditional ^{13}C direct detection for concurrent improvement in sensitivity and resolution. The results described above suggest that most standard ^{13}C-detected 2D and 3D SSNMR involving side-chain signals can be replaced by ^{1}H-detected 3D and 4D SSNMR, respectively, with significantly enhanced resolution and sensitivity. We already

confirmed that for this sample, a 3D ^{1}H/^{13}C/^{13}C chemical-shift correlation spectrum can be collected within 2.5 h with nearly complete signal assignments for the 7 Ile residues [12]. The data suggest that side-chain assignments by 3D SSNMR analysis can be obtained from 10 nmol of a protein (or ~90 µg for Ubq) within only ~3 days.

Finally, we would like to point out the importance of optimizing probe design and its efficiency. **Figure 5** shows a 2D ^{1}H/^{13}C correlation spectrum for the same SAIL ubiquitin sample obtained with the first-generation double-resonance CPMAS probe with a 1-mm spinning module operated in a static magnetic field of 18.8 T (^{1}H frequency of 800 MHz). At this point, JEOL did not realize a vital role of a temperature control under UFMAS, and thus the UIC group designed a variable-temperature stack fitted from the top of the magnet for a

temperature control. Comparable signal-to-noise (S/N) ratios and resolution to those in Fig. 4(a) were obtained but with a much longer experimental time (~50 min). On a basis of the test results at UIC, the new quad-resonance 1-mm probe used for Fig. 3 was developed. The JEOL probe development group significantly improved the efficiency of the ^{1}H RF channel of the new 1-mm probe. The quad-resonance probe is also equipped with a dedicated VT air line built into the probe and a ^{2}H-RF channel for ^{2}H decoupling. **Figure 6** compares an aliphatic region of ^{13}C CP-MAS spectra of SAIL L-isoleucine (a) with and (b) without ^{2}H decoupling. Clearly, the sensitivity and resolution of CDH and CD$_2$H signals are greatly enhanced by ^{2}H decoupling. The 0.75-mm quad-resonance probe used for Fig. 3 was designed based on the success of the 1-mm quad-resonance probe. It would not be surprising that further improvements in the design

Fig. 4
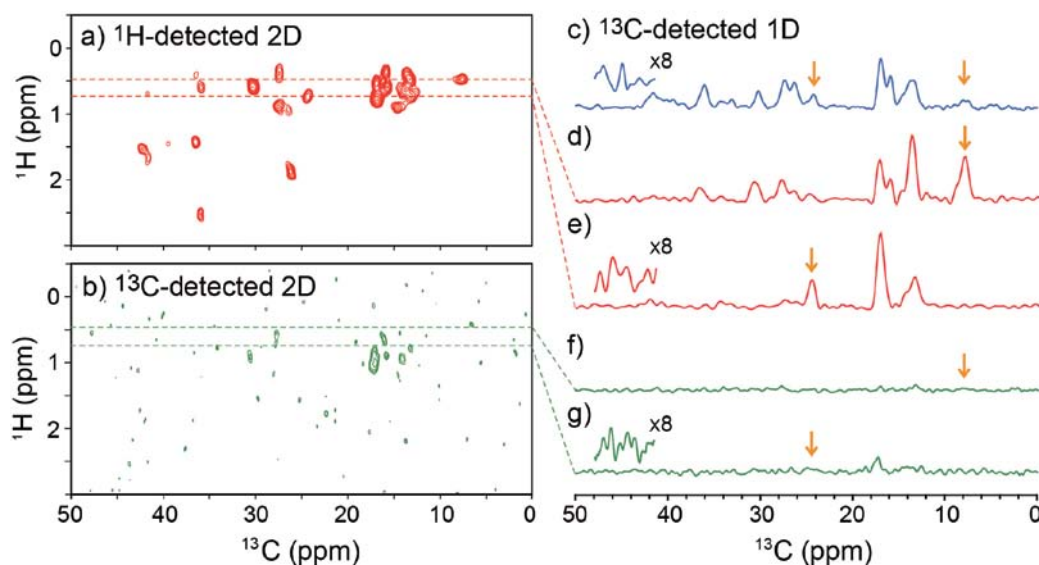
A comparison of (a) ^{1}H-detected and (b) ^{13}C-detected 2D ^{13}C/^{1}H spectra and (c) a 1D ^{13}C CP-MAS spectrum of a SAIL-Ubq microcrystalline sample (~0.5 mg) at MAS 80 kHz. (d–g) 1D slices from ^{1}H shifts of (d, f) 0.43 ppm and (e, g) 0.69 ppm from (d, f) ^{1}H-detected and (e, g) ^{13}C-detected experiments. All the data were collected with a JEOL 1-mm quad-resonance 750 MHz probe. All spectra were processed with 45°- and 60°-shifted sine-bell window functions in the ^{1}H and ^{13}C dimensions, respectively. The ^{1}H and ^{13}C line widths were 0.10–0.22 ppm and 0.66–0.94 ppm, respectively, in the absence of any window functions. The insets in (c, e, and g) show the magnified noise regions. Each spectrum in (a–c) was collected within ~5 min. The data were modified from ref. [12]. The pulse sequences used for (a) and (b) are found in ref. [12].

Fig. 5
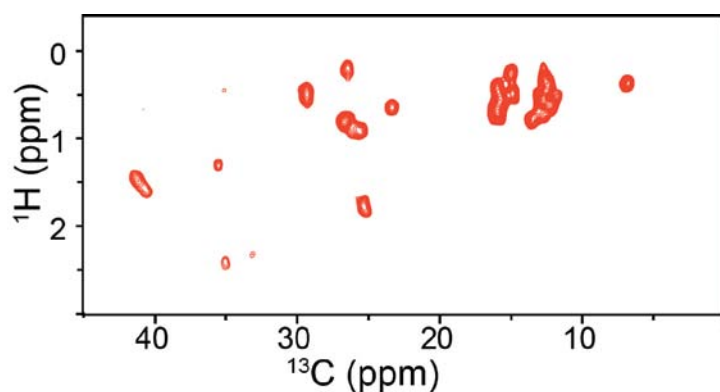
A ^{1}H-detected 2D ^{13}C/^{1}H spectra of the same SAIL-Ubq (~0.5 mg) sample collected at MAS 80 kHz with the first-generation prototype 1mm double-resonance CP-MAS probe for a 800 MHz spectrometer. The experimental conditions are similar to those for Fig. 4(a) except for the experimental time (~50 min) and the lack of ^{2}H decoupling.

Fig. 6

a) With ^2H dec
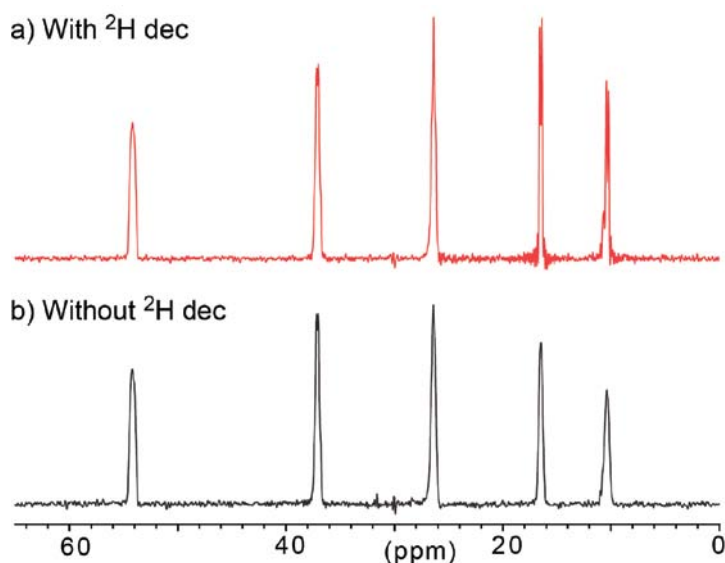
b) Without ^2H dec

A comparison of the aliphatic region of ^{13}C CP-MAS spectra of SAIL L-isoleucine (a) with and (b) without ^2H RF decoupling. In (b), ^2H WALTZ-16 decoupling at 0.25 kHz was applied during the signal acquisition [12].

of a probe equipped with a micro coil and a UFMAS module would offer additional 2-3 fold mass-sensitivity enhancement from the current status. Serious probe development efforts are also demanded for ultra-high-field SSNMR spectroscopy at a ^1H frequency over 1 GHz in the next several years.

Conclusion

Although NMR spectroscopy is generally considered to be a matured research field, recent development of novel SSNMR instruments and methods has provided tremendous enhancements in sensitivity and resolution for biomolecular SSNMR. Here, we presented up to 10-fold sensitivity improvements when a ^1H-detected 2D–3D experiment is compared with an equivalent ^{13}C-detected 2D–3D experiment. This was achieved by a combination of ^1H detection, SAIL scheme, and UFMAS at 80 kHz. Equally importantly, our data clearly showed advantage of ^1H indirect detection method over traditional ^{13}C direct detection for concurrent improvement in sensitivity and resolution for SSNMR for the first time. It will be feasible to reach the detection limit of a few nmol or sub-nmol of proteins by further sensitivity enhancement using paramagnetic doping [4, 18], modified polarization transfer schemes [19], and non-uniform sampling [20].

Acknowledgments

References

[1] Schaefer, J.; Stejskal, E. O. *J. Am. Chem. Soc* **1976**, 98, 1031.
[2] Nishiyama, Y.*et al. J. Magn. Reson*. **2011**, 208, 44.
[3] Parathasarathy, S.; Nishiyama, Y.; Ishii, Y. *Acc. Chem. Res*. **2013**, 46, 2127.
[4] Wickramasinghe, N. P.*et al. Nature Methods* **2009**, 6, 215.
[5] Laage, S.; Sachleben, J. R.; Steuernagel, S.; Pierattelli, R.; Pintacuda, G.; Emsley, L. *J. Magn. Reson*. **2009**, 196, 133.
[6] Ernst, M.; Meier, M. A.; Tuherm, T.; Samoson, A.; Meier, B. H. *J. Am. Chem. Soc*. **2004**, 126, 4764.
[7] Ishii, Y.; Tycko, R. *J. Magn. Reson*. **2000**, 142, 199.
[8] Ishii, Y.; Yesinowski, J. P.; Tycko, R. *J. Am. Chem. Soc*. **2001**, 123, 2921.
[9] Zhou, D. H.; Shah, G.; Cormos, M.; Mullen, C.; Sandoz, D.; Rienstra, C. M. *J. Am. Chem. Soc* **2007**, 129, 11791.
[10] Marchetti, A.*et al. Angew. Chem. Int. Edit*. **2012**, 51, 10756.
[11] Chevelkov, V.; Rehbein, K.; Diehl, A.; Reif, B. *Angew. Chem. Int. Edit*. **2006**, 45, 3878.
[12] Wang, S.*et al. Plos One* **2015**, 10, e0122714.
[13] Metz, G.; Wu, X.; Smith, S. O. *J. Magn. Reson. A*. **1994**, 110, 219.
[14] Hediger, S.; Meier, B. H.; Ernst, R. R. *Chem. Phys. Lett*. **1995**, 240, 449.
[15] Kotecha, M.; Wickramasinghe, N. P.; Ishii, Y. *Magn. Reson. Chem*. **2007**, 45, S221.
[16] Wickramasinghe, N. P.; Kotecha, M.; Samoson, A.; Past, J.; Ishii, Y. *J. Magn. Reson*. **2007**, 184, 350.
[17] Kainosho, M.; Torizawa, T.; Iwashita, Y.; Terauchi, T.; Ono, A. M.; Guntert, P. *Nature* **2006**, 440, 52.
[18] Nadaud, P. S.; Helmus, J. J.; Sengupta, I.; Jaroniec, C. P. *J. Am. Chem. Soc*. **2010**, 132, 9561.
[19] Althaus, S. M.; Mao, K.; Stringer, J. A.; Kobayashi, T.; Pruski, M. *Solid State Nucl. Magn. Reson*. **2014**, 57-58, 17.
[20] Suiter, C. L.*et al. J. Biomol. NMR* **2014**, 59, 57.

Development of Super-High Sensitivity EDS System for GRAND ARM (JEM-ARM300F)

E. Okunishi[1], T. Sasaki[1], H. Sawada[1], Y. Jimbo[1], Y. Iwasawa[2], K. Miyatake[2], S. Yuasa[1], I. Onishi[1], M. Mita[2], T. Kaneyama[1] and Y. Kondo[1]

[1] EM Business Unit, JEOL Ltd.
[2] EC Business Unit, JEOL Ltd.

GRAND ARM

We developed a 300 kV Super-high resolution electron microscope, GRAND ARM (JEM-ARM300F) [1] (**Fig. 1**). The GRAND ARM is equipped with a variety of innovative components. These revolutionized components include 1) a new aberration corrector (ETA Corrector developed by JEOL), 2) COSMO System to control the corrector, 3) two types of newly developed objective polepieces: FHP (full high resolution polepiece) for high resolution imaging and WGP (wide gap polepiece) for multi-purpose microscopy, 4) a highly-stable electric circuit, mechanical system and microscope column, and 5) STEM detectors optimized for a wide range of accelerating voltages.

In the GRAND ARM, STEM image resolution of 63 pm is guaranteed, Furthermore, recently, an unprecedented STEM resolution better than 50 pm has been achieved as its best performance (**Fig. 2**).

Multi-functionality of TEM with the developed WGP to meet diversified needs

Transmission electron microscopes (TEMs) have been increasingly adding versatile functions and the microscopes have been used for a great deal of research & development use. To meet such diversified needs, scientists are demanding a broad range of capabilities; not only traditional image resolution, but also analytical capabilities of EDS and EELS, in-situ observation and dynamic observation. The GRAND ARM is capable of incorporating a unique polepiece called WGP to provide multi-functionality and high resolution. The WGP was developed to place priority on multi-functionality of the TEM over its resolution. The design of the WGP features that its polepiece gap is wide enough to satisfy various analytical purposes, so that EDS detectors can approach to a sample as close as possible with high take-off angle.

As is well known, a shape of a polepiece determines a microscope resolution. To obtain a high resolution, its gap must be small and highly-precise machining is also required for the polepiece. The use of this type of polepiece makes it possible to achieve high resolution; however, its narrow gap limits the specimen tilt angle and the specimen holder. In addition, it is difficult to place the EDS detector near the polepiece, thus degrading EDS detection sensitivity. On the other hand, the WGP cannot offer the image resolution comparable to that obtained with the FHP. But, its polepiece gap is a few times wider than the FHP; therefore, the WGP can accommodate various type of specimen holder and high tilt angles. Furthermore, the EDS detector can be placed near the specimen.

In particular in recent years, a diverse range of specimen holders have been developed, which enable observations in liquid or gas environment, observation with heating or cooling,

Fig. 1

Appearance of GRAND ARM (JEM-ARM300F) with View camera system.

Fig. 2
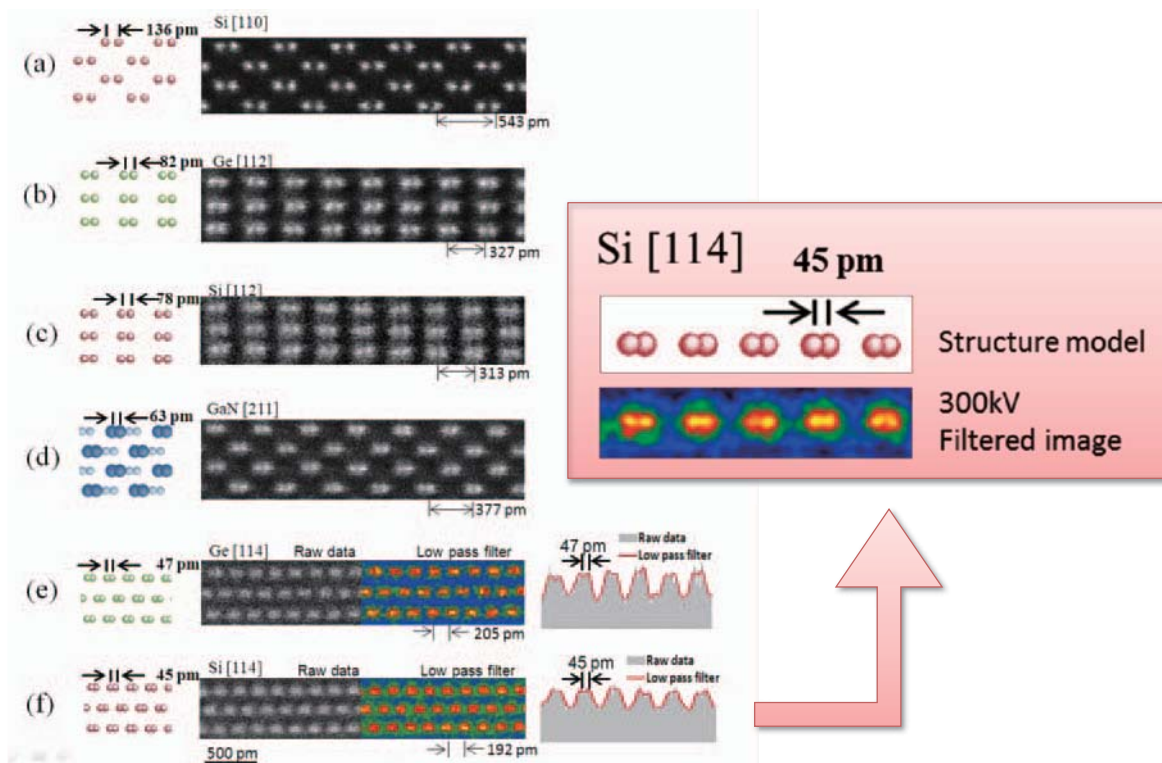
High-resolution HAADF images of dumbbells showing narrow spacings for various materials along various orientations.
(a) Si [110], (b) Ge[112], (c) Si[112], (d) GaN[211], (e) Ge[114], (f) Si[114].

with cathodoluminescence spectroscopy, etc. A big advantage of the WGP is that those unique holders can be used with the WGP.

Development of super-high sensitivity EDS system

EDS, an analytical function of the TEM, is widely used for elemental analysis which identifies constituent elements in a specimen by detecting characteristic X-rays emitted from the specimen. As is shown in **Fig. 3**, the EDS detector is placed near the specimen holder. The X-rays generated from the specimen emit isotropically in the direction of a sphere equal to 4π (equivalent to the solid angle for all directions in the sphere). But as is seen from the placement and geometry of the EDS detector, normally the detector can detect only a small portion of total emitted X-rays. This limitation leads to a small solid angle and low detection efficiency for EDS. In order to improve such a disadvantage, it is effective to place the detector close to the specimen and/or to make the detection area larger. A large solid-angle detector for TEM which has a detection element area of 105 mm² has recently been developed. For improving the limitation of the detection-element size, the detection system equipped with plural detectors has also been developed. For the GRAND ARM, a newly developed super-high sensitivity EDS system composed of two detectors with 105 mm² detection area is incorporated in the microscope.

The present super-high sensitivity EDS system features 1) Equipped with dual detectors of 105 mm² detection area, 2) One

(SDD1) is placed at 90° with respect to the specimen holder rod axis, 3) and the other (SDD2) is placed along the holder axis, where SDD stands for silicon drift detector. The simple detector scheme of this innovative EDS system is shown in **Fig. 4**. Moreover, the geometriy of the polepiece and the EDS detectors were optimized to allow high X-ray take-off angle. As is shown in **Fig. 5**, normally when an EDS detector is placed closer to the specimen, the take-off angle becomes unavoidably lower due to the shape of the upper pole of the polepiece. However, a breakthrough measure was taken in the GRAND ARM to overcome this problem. As described above, we designed the WGP and the EDS detectors in such a way that the amount of detected characteristic X-rays becomes optimum from the viewpoints of the detector (distance between the detector and specimen) and the X-ray take-off angle. Our development achieved a take-off angle as high as 25° or more. As is listed in **Table 1**, both of high solid angle and high take-off angle are enabled without tradeoff. Table 1 demonstrates that the total solid angle of the dual detectors is 1.6 sr, which is approximately $\pi/2$. The spectral intensities of Ni-Kα lines (Ni-K counts) from NiO_2 layer, acquired with the detectors at the same measurement conditions, are compared in **Fig. 6**. From this graph, it is found that SDD2 for the GRAND ARM has very high sensitivity, approximately twice that of SDD1. From this result, it is clear that the use of the dual EDS detectors achieves dramatically high sensitivity.

The result of atomically-resolved elemental maps obtained from $SrTiO_3$ is shown in **Fig. 7**. Owing to high sensitivity of

Fig. 3
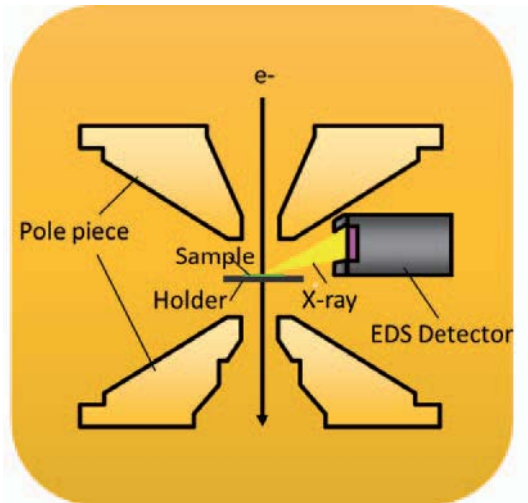
EDS detector geometry around the specimen holder and the objective polepiece.

Fig. 4
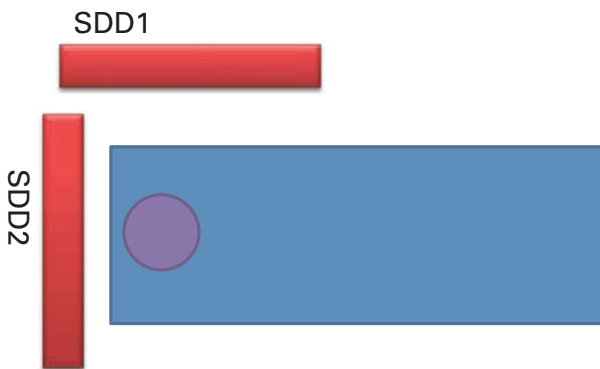
SDD1

SDD2

Detector geometry of the new EDS system. Each detector make 90 degree relationship. SDD2 position is much closer to the specimen holder than SDD1.

Fig. 5

Pole piece(upper)

(1)Position (high)

(2)Position (Low)
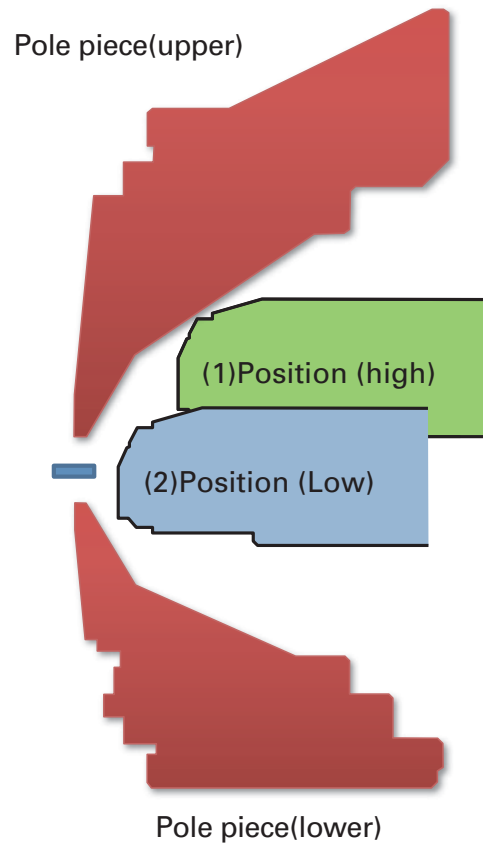
Pole piece(lower)

Cross section of polepieces and EDS detector.
(1) Position(high) has high take-off angle, but the distance from the specimen becomes longer.
(2) Position(Low) can set the detector location closer to the specimen, but take-off angle becomes lower.

Table 1

	Detector size (mm^2)	Take Off angle (degree)	Solid angle (sr)
SDD1	105	24.775	0.552
SDD2	105	29.043	1.080
Dual			1.632

Solid angle and Take-off angle.

the new EDS detectors, sharp distribution at each elemental site is acquired in approximately 2.5 min. In addition, since SDD2 detects X-rays from the direction along the specimen holder rod, it is easily estimated that SDD2 is hardly influenced by tilting of specimen holder. Thus, this placement of SDD2 offers is expected to be a good condition for 3D EDS tomography. Furthermore, the highly sensitive EDS detector system is very effective when probe current is low, enabling analysis with reduced beam damage to specimen.

Application example 1

EDS maps of ZrO_2 polycrystalline ceramics acquired with the dual SDD X-ray detection system are shown in **Fig. 8**. Even with

Fig. 6

Probe current : 1nA
Specimen : NiO_2 thin film
Acquisition time : 60sec
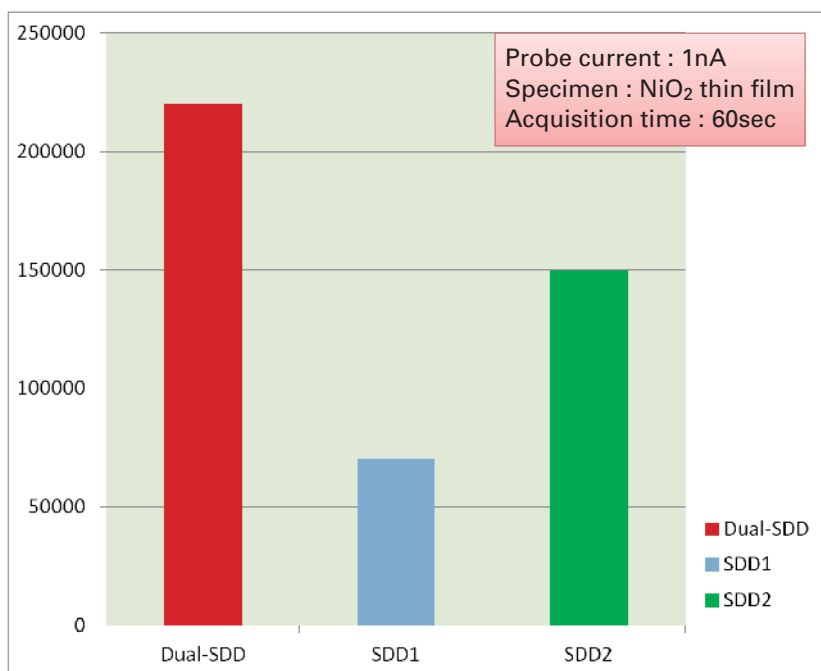
Comparison of Ni-K counts at each microscope configuration

Fig. 7
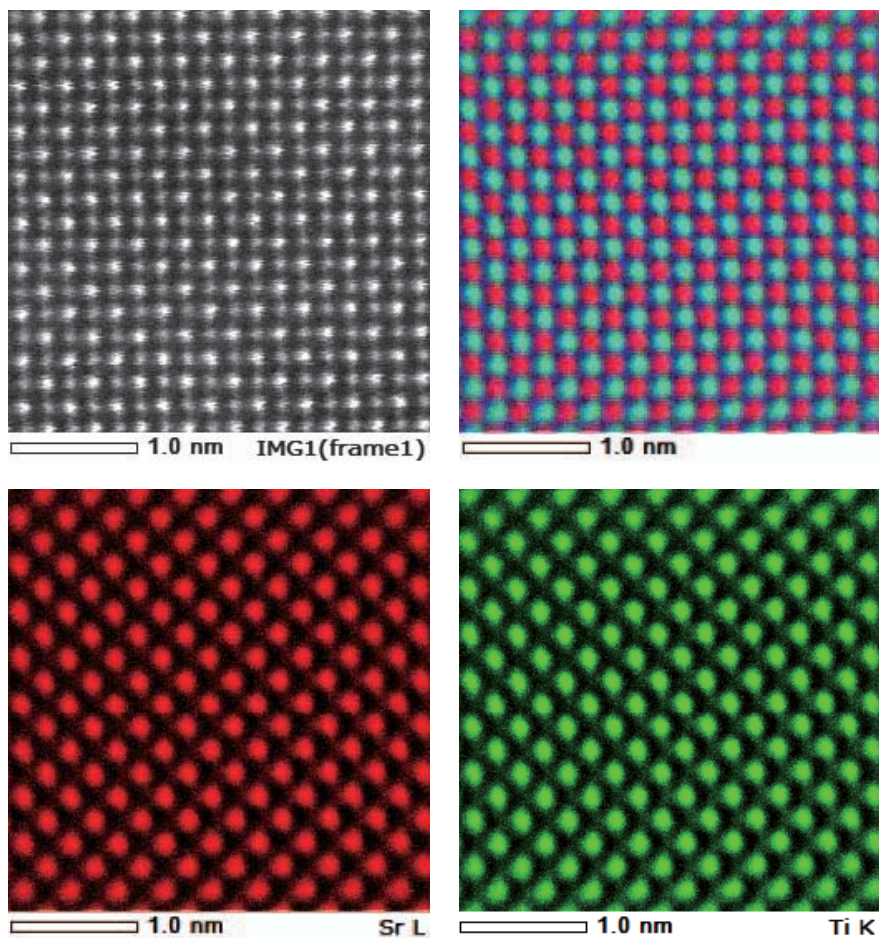
256 × 256 pixels map.
Acquired in 2.5min(with filtered)
Probe current 80pA.
300kV accelerating voltage.

Example of atomic resolution EDS maps. Specimen: $SrTiO_3$

pixels of 512 × 512, sharp elemental distribution is acquired in the analysis time of approximately 30 min. Normally, trace amounts of dopant elements are added to ceramics in order to improve its material properties. In materials analysis, it is important to know how these doped elements behave in a material because this behavior may answer for improvements in material properties. From the result of the EDS mapping, in addition to Zr and O, Si, Y and Al are detected. The elements are found at grain boundaries. Especially, these elements segregate a lot at triple junctions of the grain boundaries to a great amount. Furthermore, it is revealed that Y particles are also located within the grains and their distributions agree well with the image contrast that seems to be defects in the grains. Since defects in a crystal can give rise to element segregation, this result shows that the segregation states are elucidated by EDS mapping.

Application example 2

EDS maps obtained from Pd/Au core-shell particles (particle diameter: approx. 17 nm) are shown in **Fig. 9**. Such particles are susceptible to damage by electron-beam irradiation. Therefore, when measured with a large probe current, their sizes and elemental distributions are likely to change. To prevent this problem, measurement was performed at an accelerating voltage of 160 kV and with a probe current as low as 30 pA. As can be seen in the EDS maps, distributions of each element are clearly visible. In a particular particle, Pd layer which constitutes a shell surrounding Au core is extremely thin. In addition, as is shown in **Fig. 10**, there is no large difference in STEM (HAADF) images acquired before and after EDS mapping. This result indicates that beam damage to the specimen is suppressed to be low. The X-ray intensity profiles acquired from the EDS maps show that the obtained Pd layer has a width of approx. 0.6 nm (Fig. 9). This width corresponds roughly to three atomic layers.

Owing to the use of the newly-developed detection system, very high detection sensitivity is achieved, thus leading to acquisition of a sufficient amount of X-ray signals even at a low probe current. Utilizing this capability, atomic resolution EDS elemental maps are obtained from a very thin region composed of a few atomic layers while keeping electron-beam damage to the specimen to be low.

Summary

We developed a super-high sensitivity EDS system for the JEM-ARM300F (GRAND ARM), a Cs-corrected 300 kV TEM. In addition to a large detection area, this new detector positions were optimized by changing the shape of the objective lens polepiece. The solid angle for X-rays detection is obtained to be 1.6 sr. The use of the new system enables one to acquire X-ray signals as doubly or triply high as those acquired with the conventional EDS system. Such high sensitivity enables one to perform very fast analysis even in an atomic-resolution elemental mapping. Furthermore, even when the probe current is dramatically reduced to minimize specimen damage caused by an electron beam, analysis with sufficiently high sensitivity is enabled. These capabilities are very advantageous for an EDS analysis.

Thus, this newly-developed EDS system for the GRAND ARM will broaden applications to beam-sensitive specimens and also enhance X-ray acquisition throughput.

References

[1] H. Sawada et al.; Super high resolution imaging with atomic resolution electron microscope of JEM-ARM300F. *JEOL News*, **49**, **No.1**, 51-58 (2014).

Fig. 8
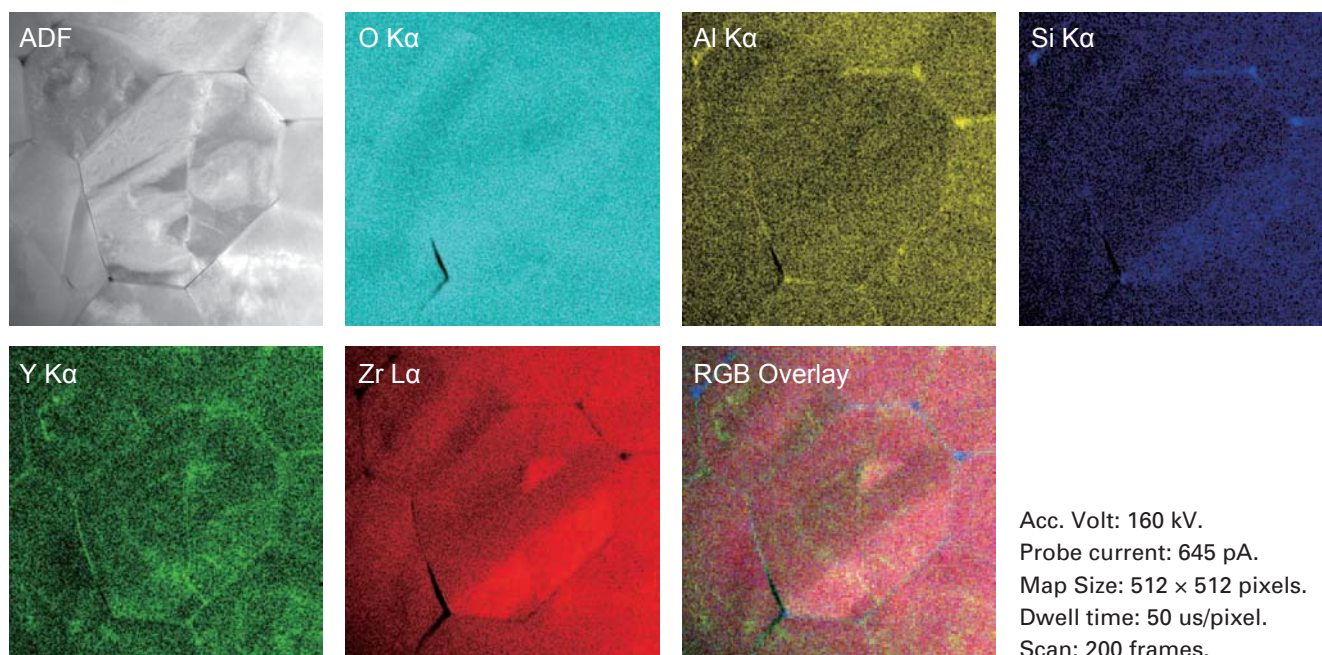
EDS mapping of ZrO_2 ceramics. Y, Al and Si were segregated in grain boundaries and triple junctions. Y also segregated on defects in crystal grain.

Acc. Volt: 160 kV.
Probe current: 645 pA.
Map Size: 512 × 512 pixels.
Dwell time: 50 us/pixel.
Scan: 200 frames.

Fig. 9

HAADF

17 nm

5 nm

Au

Pd

Au+Pd

Intensity profiles

0.6nm

Pd
Au

nm
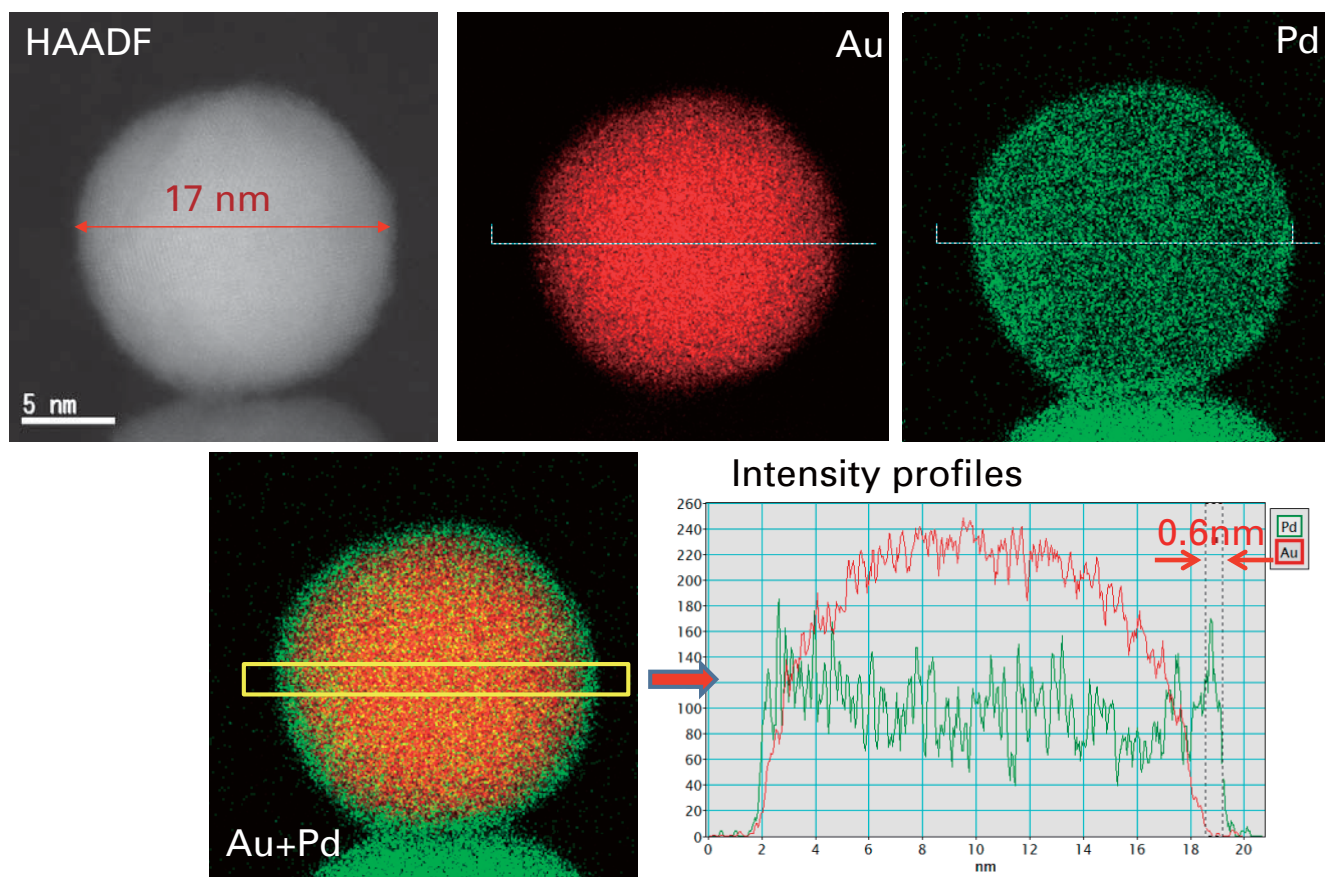
EDS mapping of Core-Shell nano-particles at low current probe condition.

Fig. 10

(a) Before mapping
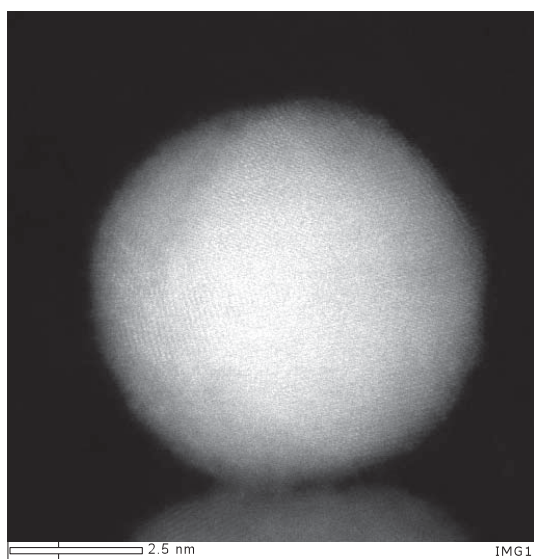
(b) After mapping (18 min later)

2.5 nm

IMG1

2.5 nm

IMG1
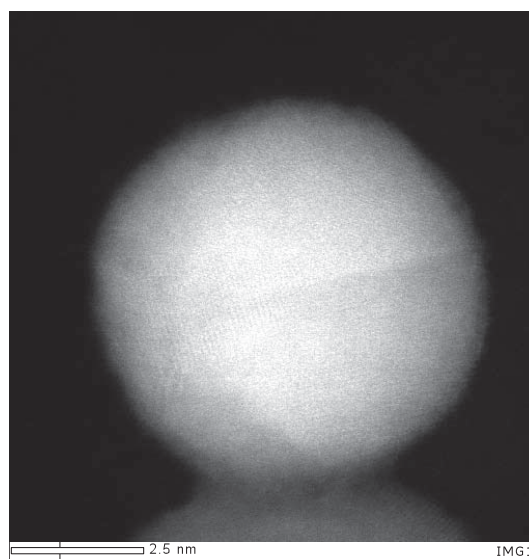
Comparison of STEM-HAADF images acquired before and after mapping.

Newly Developed Soft X-ray Emission Spectrometer, SS-94000SXES

Masaru Takakura[1], Takanori Murano[1], and Hideyuki Takahashi[2]

[1] SA Business Unit, JEOL Ltd.
[2] Global Business Promotion Division, JEOL Ltd.

Introduction

JEOL's SS-94000SXES is a brand-new spectrometer which can detect ultra-soft X-ray in an energy range from 50 to 210 eV. The characteristic X-ray in the energy range includes the emission spectra based on the valance band transitions of many elements. Soft X-ray Emission Spectrometer (SXES) enables higher energy resolution than that of the conventional EPMA. Thus, this spectrometer is an instrument being applicable to chemical bonding state analysis. On the other hand, whole elemental analysis needs to measure the characteristic X-rays at least up to 10 kV which are generated by deeper core level transitions than those of soft X-rays. Accordingly, SXES is used in conjunction with the wavelength dispersive X-ray spectrometers (WDSs) including some of analyzing crystals and the energy dispersive X-ray spectrometer (EDS). In this paper, our new soft X-ray emission spectrometer, SS-94000SXES will be introduced, and its specification and application to some materials will be shown.

Background of developing SXES and specifications of SXES

This spectrometer design has been developed at first in one of the Leading Projects of the Ministry of Education, Culture, Sports, Science and Technology by Prof. Terauchi [1] who aimed at detection of the soft X-ray emission spectra using a transmission electron microscope (TEM). For versatile use, this spectrometer has been designed to attach to a scanning electron microscope (SEM) and an electron probe microanalyzer (EPMA), which was implemented in one project of Japan Science and Technology Agency (JST). Commercial version (**Fig. 1**) has been started to be provided in Oct. 2013.

Figure 2 shows a schematic view of SXES attached to an SEM. SXES is belonging to WDS, so the geometrical positions of a specimen (an electron-beam irradiated position), diffraction grating, and CCD array should be adjusted precisely to one another. The diffraction grating is adopted with the variable line and space (VLS) which is designed to obtain a high resolution X-ray spectrum by a CCD array detector. In the case of the EPMA-SXES system, a built-in optical microscope is used for adjusting a sample height in order to measure a soft X-ray spectrum with stable peak position.

Main specifications of the SS-94000SXES are as follows.

Acquired energy range:	50 to 170 eV (JS50XL)
	70 to 210 eV (JS200N)
Energy resolution:	0.3 eV or better
	(Al-L emission spectrum at Fermi edge)
Applicable models:	JSM-7800F, JSM-7800F Prime,
	JSM-7100F
	JXA-8230, JXA-8530F,
	JXA-8100, JXA-8200, JXA-8500F

Specifications of SXES, WDS, and EDS are listed in **Table 1** for comparison. **Figure 3** shows the energy band diagram and X-ray emission spectra obtained by SXES and WDS. This figure shows the aluminum energy band diagram, and the emission spectra obtained from an aluminum-boron compound. The red colored spectra correspond to aluminum emission peak from the aluminum phase, and blue colored spectra to that from the aluminum boride inclusion. In the case of conventional EPMA and EDS, the Al-Kα (1.486 keV) line which is based on the $L_{2,3}$-K electron transition is measured for elemental analysis. There is no big difference in peak position and peak shape between these spectra from the two phases, whereas this X-ray intensity ratio is nearly proportional to the mass fraction of the two phases in the sample. So, these characteristic X-rays can be used for elemental analysis of the sample.

WD spectra from some of the elements exhibit the difference of the chemical bonding states such as the Al-Kβ (1.557 keV) line which is based on the transition between valence band and K shell level. SXES can measure the soft X-ray emission spectra in the region between 50 and 210 eV, which mainly includes the information about the transition from the valence band. In case of Al alloy, SXES can exhibit the Al-L band (~73 eV) [2] emission. Figure 3 also shows the energy shift of Al-L Fermi edge by about 1 eV between aluminum-boron compound and aluminum. This is regarded as a shift of the L-band edge associated with the Al-B alloying.

Fig. 1

Soft X-ray Emission Spectrometer, SS-9400SXES.
This can be attached to JSM-7800F series.

Fig. 2
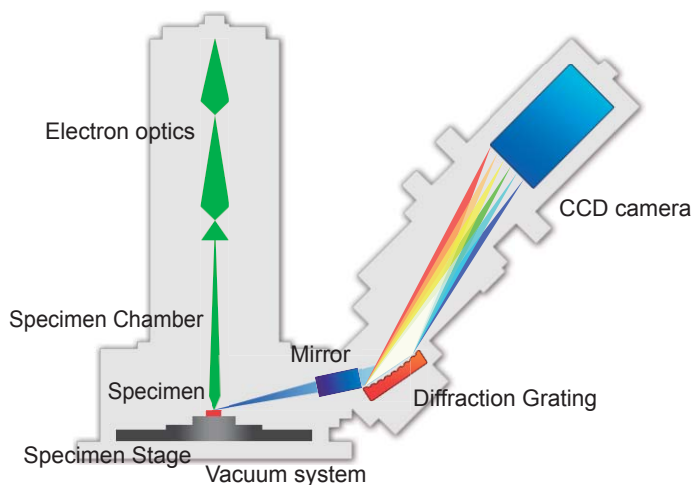
Schematic view of SXE spectroscopy

Table 1

	SXES	WDS	EDS
Energy Range	50 ~ 210 eV (~ 700 eV (High order X-ray))	100 eV ~ 12 keV	100 eV ~ 20 keV
Energy Resolution	0.3 eV @ Al-L Fermi edge	~ 8 eV @ Fe-Kα FWHM	~ 130 eV @ Mn-Kα FWHM
Chemical bonding state analysis	Yes	Yes	No
Parallel detection	Yes	No	Yes
Analyzer and Detector	VLS Grating, and CCD	Analyzing Crystal, and Proportional Counter	SDD
Detection limit	20 ppm *	100 ppm *	5000 ppm *

Comparison of specs among SXES, WDS, and EDS

"Information depth" obtained by SXES is expected to be smaller than those by the conventional EPMA and EDS. In case of the bulk sample analysis, the information depth obtained from the characteristic X-ray measurement depends on specimen and accelerating voltage used for the measurement. In an actual bulk sample analysis, high-kV analysis at an accelerating voltage higher than 10 kV is not suitable because the lower energy X-ray emissions are seriously absorbed in the specimen [3]. It is more practical to use X-ray emissions of less than 5 kV. **Figure 4**(a) shows the Al-L spectra taken from carbon coated samples at an accelerating voltage of 2 kV, and Fig. 4(b) shows the Be-Kα spectra taken from gold coated samples at 5 kV. The coating thicknesses are calculated by the thin-film analysis program of EPMA [4]. The decrease of Al-L intensity can be approximately expressed by the exponential decay curve. We defined the information depth of SXES as three times the decay coefficient. **Table 2** shows the calculated information depth of SXES at

2 kV and 5 kV. The information depth of SXES is distributed over the wide range from tens of nm to several hundred nm. It is found that the information depth obtained by SXES is about one order smaller than that by the conventional EPMA.

Application example of SXES

A blade surface on tool steel and super-steel is often coated by TiN, TiCN, Al_2O_3, and their multilayers. EPMA is used to analyze the TiN coating. It is well known to be difficult to analyze the X-ray spectrum of TiN because the energies of Ti-Lι and N-Kα are very close and then these spectra are frequently overlapped in conventional EDS and WDS. Therefore spectra deconvolution techniques have to be applied for quantitative analysis. Regarding this problem, it is effective to measure the Ti-Lι and N-Kα emission spectrum by SXES because of its higher energy resolution. **Figure 5** shows the spectra of a

Fig. 3
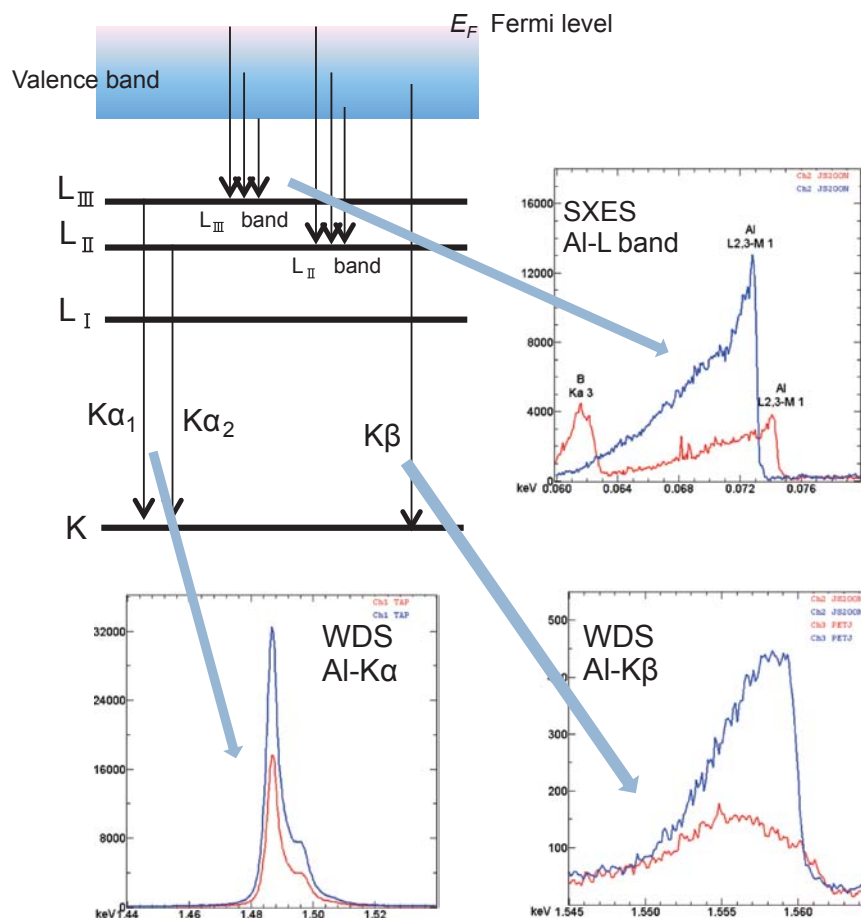
Energy band diagram of aluminum, and X-ray emission spectra acquired by SXES and WDS.

titanium nitride sample obtained by several detectors, SXES, WDS, and EDS. In Fig. 5, SXES is the second order diffracted spectrum. SXE spectrum has higher energy resolution, which makes it possible to reveal the spectral shoulder due to Ti-Lι. **Figure 6** shows a sectional backscattered electron image of the super-steel blade, and SXE spectra acquired from the TiCN and top Ti coated regions. **Figure 7** also shows the SXE line profiles across the ceramic coated layers in the super-steel blade surface. It is found that SXES can easily distinguish the distributions of Ti and N.

Summary

We have developed a unique X-ray emission spectrometer, SS-94000SXES. This spectrometer has many merits for analysis of bulk surfaces such as chemical bonding state analysis, low-kV analysis, and several tens to several hundred nm region analyses. On the other hand, spectral data in the soft X-ray region have not been sufficiently stored for the practical application of SXES. The standard spectra database is now under construction for future use of SXES.

References

[1] M. Terauchi, H. Yamamoto and M. Tanaka, *Journal of Electron Microscopy*, **50**, 101, (2001).

[2] J. A. Berden, *Reviews of Modern physics*, **39**, No.1, 78 (1967).

[3] H. Takahashi, T. Murano, M. Takakura, N. handa, M. Terauchi, M. Koike, T. Kawauchi, T. Imazono, N. Hasegawa, M. Koeda, T. Nagano, H. Sakai, Y. Oue, Z. Yonezawa, and S. Kumamoto, *JEOL News* **49, No.1**, 74 (2014).

[4] M. Takakura, H. Takahashi, and T. Okumura, *JEOL News* **33, No.1**, 15 (1998).

Fig. 4

C (ρ ~ 2.0g/cm³) on Al
Acc. V. : 2kV

C-Kα (n=4)

C : non coat
11nm
15nm
24nm
39nm

Al-L (73 eV)

C-Kα (n=5)

X-ray Intensity (arb. Unit)

X-ray Energy (keV)

Au (ρ ~ 19.3g/cm³) on Be
Acc. V. : 5kV

Be-Kα (110 eV)

Au : non coat
1.5nm
4.4nm
8.7nm
12.7nm

Au-N (n=2)

X-ray Intensity (arb. Unit)

X-ray Energy (keV)
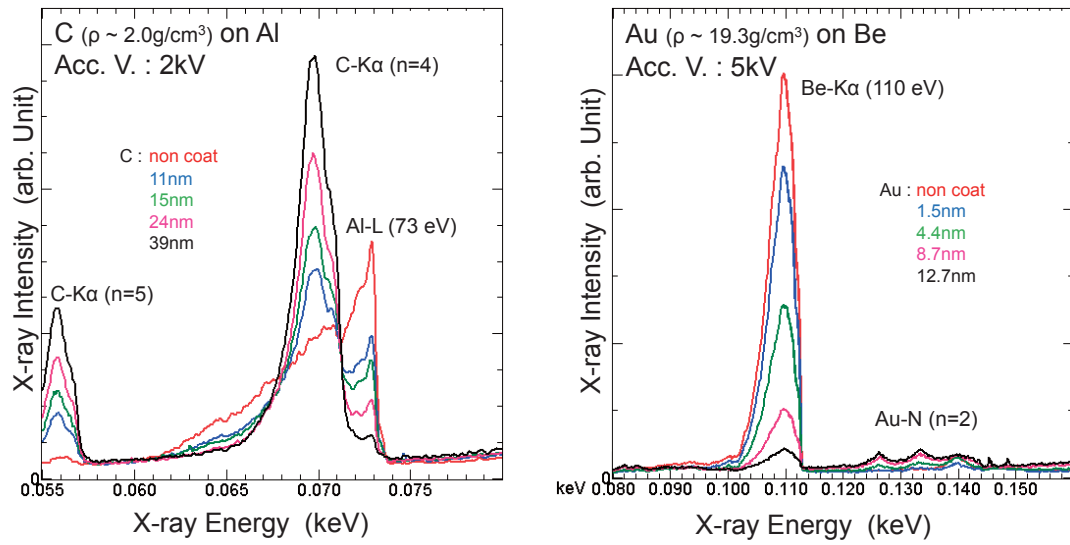
SXE spectra obtained from coating samples. a) carbon coated aluminum sample measured at 2 kV. b) gold coated beryllium sample measured at 5 kV.

Table 2

Acc. V. : 2 kV	Al-L *(73 eV)*	Be-Kα *(110 eV)*
Carbon	54	71
Gold	10	13

Acc. V. : 5 kV	Al-L *(73 eV)*	Be-Kα *(110 eV)*
Carbon	103	273
Gold	15	31

unit : nm

Calculated information depth of SXES at 2kV and 5kV.

Fig. 5

N-Kα

Ti-Lι

Ti-Lα,Lβ

SXES
EDS
WDS

Normalized X-ray Intensity (%)

X-ray Energy (keV)
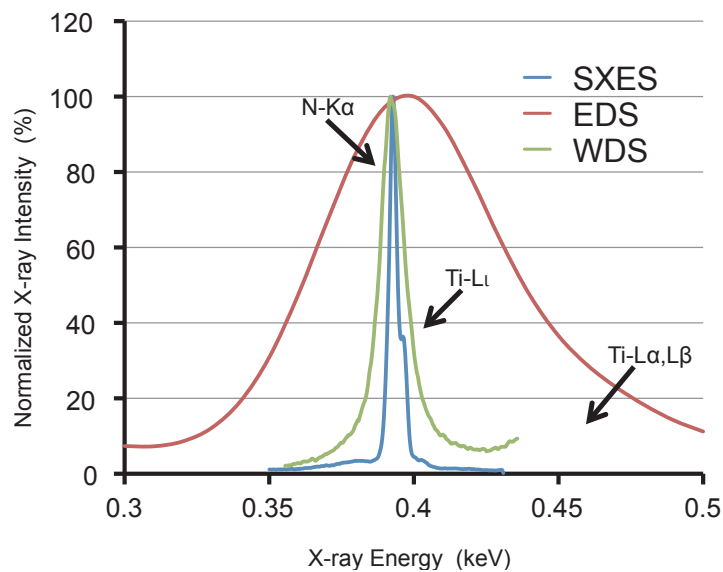
Comparison of spectra from a TiN sample measured by SXES, EDS and WDS. SXES can measure the second order N-Kα and Ti-Lι line spectra. This graph is converted to the energy of the first order.

Fig. 6

Super-steel   TiCN   Al$_2$O$_3$ Ti coating

▬ 2μm

N-K (n=2)   Ti-Lι (n=2)

X-ray Intensity (Arb.Units)

Ti coating

TiCN

0.190   0.195   0.200   0.205

X-ray Energy (keV)
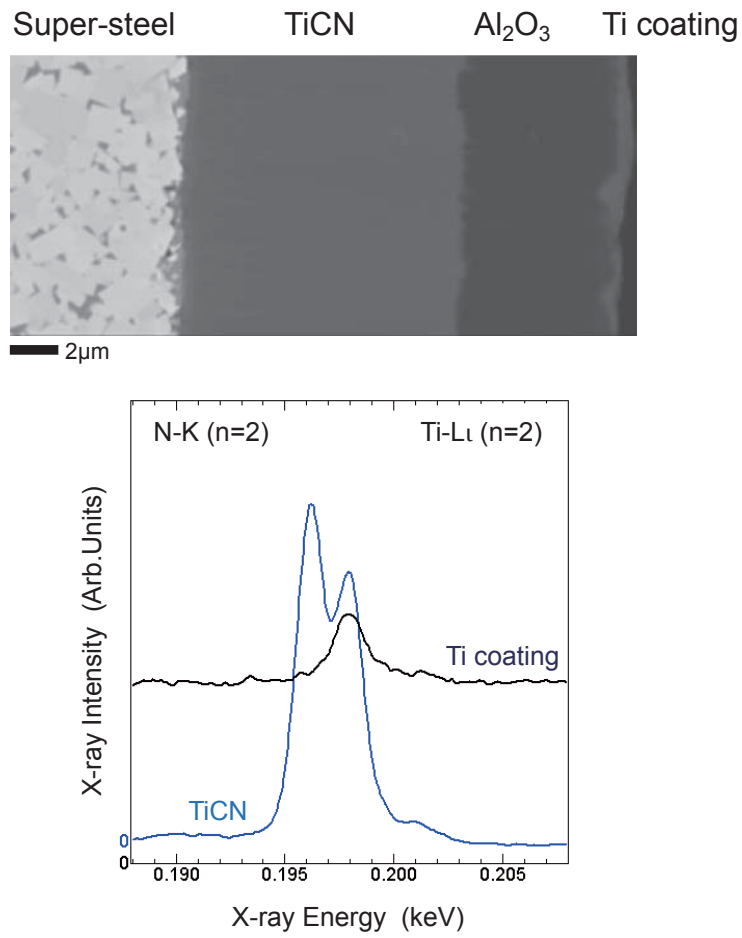
Sectional view of the ceramic coated layers on the super-steel, and SXE spectra from the TiCN and top Ti regions.

Fig. 7

W-N (n=1)

C-K (n=2)

Ti-Lι (n=2)

N-K (n=2)

O-K (n=3)

X-ray Intensity (Arb. Units)

000   0.0010   0.0020   0.0030   0.0040   0.0050   0.0060   0.0070

Length (mm)
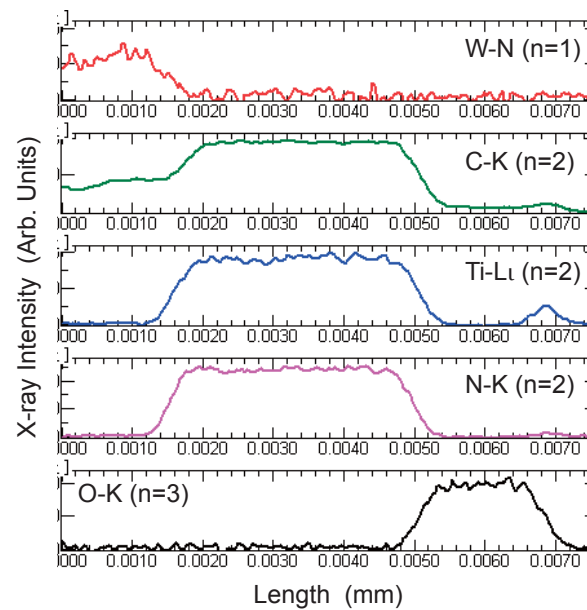
SXE line analysis of the ceramic coated layers in Fig.6

Additional Ar-Ion Etching of FIB-Prepared TEM Samples using Ion Slicer

T. Mihira[1], N. Endo[2], H. Hashiguchi[2] and T. Suzuki[1]

[1] IB Business Unit, JEOL Ltd.
[2] EM Business Unit, JEOL Ltd.

Additional Ar-Ion Etching method using the Ion Slicer (Ion Slicer Finishing Method) was developed. This new method is intended to improve the quality of a thin-film sample prepared by FIB while maintaining advantages of FIB thinning. Improvement in the quality of the thinned sample is achieved by irradiating the sample with a low-accelerating voltage Ar-ion beam after FIB processing using the Ion Slicer, an ion-milling thin-film sample preparation tool. Furthermore, the development of the special-shape FIB grid and the FIB-Ion Slicer common holder facilitated the transfer of the sample from the FIB system into the Ion Slicer, and improved the efficiency of the sample-preparation procedures.

Introduction

Thin-film TEM sample preparation using FIB provides a high-positional accuracy thinning on the order of sub-micrometers or less, and also requires non-expert processing techniques. However, a thin-film sample prepared by FIB suffers a larger sample damage due to a gallium (Ga) ion beam, compared with that prepared by argon (Ar) ion milling.

To prevent this problem, the Additional Ar-Ion Etching method using the Ion Slicer (Ion Slicer Finishing Method) was developed. This new method is intended for improving the quality of a thin-film sample prepared by FIB while maintaining advantages of FIB thinning. Improvement of the quality of the thinned sample is achieved by irradiating the sample with a low-accelerating voltage Ar-ion beam after FIB processing using the Ion Slicer, an ion-milling thin-film sample preparation tool. Also in this report, the effectiveness of this method was examined.

Overview of Thin-Film Sample Preparation Methods Using FIB and Ion Slicer

The Ion Slicer Finishing Method for a thin-film sample prepared by FIB employs both FIB and the Ion Slicer. Those tools can perform thin-film processing independently of each other. Prior to explanation of the new method, each thin-film preparation method is described.

Thin-film sample preparation procedures using FIB (Bulk Pickup Method)

The Bulk Pickup Method [1], one of thin-film sample preparation methods using FIB, utilizes a FIB grid for thin-film processing. The procedures of this method are shown in **Fig. 1**. The method has the following features.
A) Thin-film processing from a different direction, such as back-side thinning, is possible with simple operations.
B) Sample preparation for cross-section observation and plan-view observation can be easily performed.
C) A sample can be re-processed after TEM observation.
D) A sample composed of magnetic material can be subject to thin-film preparation for TEM observation.

Thin-film sample preparation procedures using the Ion Slicer (Ion Slicer method)

The Ion Slicer method, a new concept method, performs thinning using a shielding effect of a masking belt [2]. As shown in **Fig. 2**, this method has the following features.
A) There is no need for mirror-surface finishing or dimple-grinding treatment, thus enabling ion polishing simply after sizing a sample to a rectangular shape.
B) Since pre-polishing is simple, the method enables short-time specimen preparation and the polishing accuracy is almost the same among operators regardless of the skill of thinning.
C) Even for a soft metal material, sample distortion and specimen damage will be minimal during the polishing.
D) Since a shielding effect of a masking belt is utilized for thinning, the Ion Slicer can perform thin-film preparation even for a hard sample, a composite material or a fragile sample.

Ion Slicer Finishing Method for an FIB-Prepared Thin-Film Sample

The Ion Slicer Finishing Method for a thin-film sample

>> 3-1-2 Musashino, Akishima, Tokyo, 196-8558, Japan | E-mail: tmihira@jeol.co.jp

prepared by FIB is intended for finishing a thin-film sample milled with an FIB beam with Ar-ion beam using the Ion Slicer. Irradiation of a low-accelerating voltage Ar-ion beam using this method enables damage layers to be removed, which were formed by Ga ions during the FIB milling.

Features of the Ion Slicer Finishing Method

Table 1 shows the features of a thin-film sample prepared by both FIB and the Ion Slicer and an FIB-prepared thin-film sample subject to the Ion Slicer Finishing Method. The features of the FIB-prepared thin-film sample and those of the Ion Slicer-

Fig. 1 Thin-film sample preparation process using FIB.

1. Sample block **2. Pickup** **3. Thinning processing**
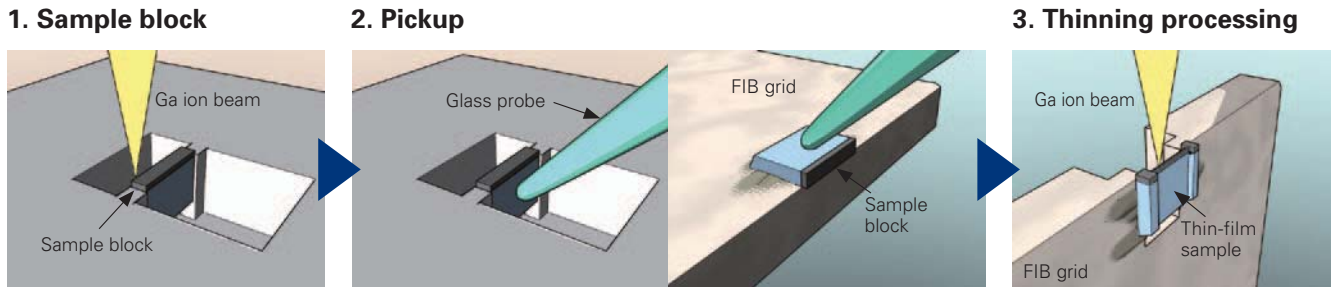
1. A sample block containing area of interest is cut and exposed by FIB processing. The block is processed to about 10 to 20 µm wide, about 2 to 10 µm thick and about 10 µm in height.
2. Using the pick-up system, the sample block is picked up with a glass probe and fixed onto the FIB grid. Epoxy resin is used to fix the sample block.
3. Thinning processing using FIB is made to obtain an appropriate sample thickness for TEM observation.

Fig. 2 Thin-film sample preparation process using the Ion Slicer.

Material **1. Cutting** **2. Polishing** **3. Ar-Ion milling** **TEM observation**
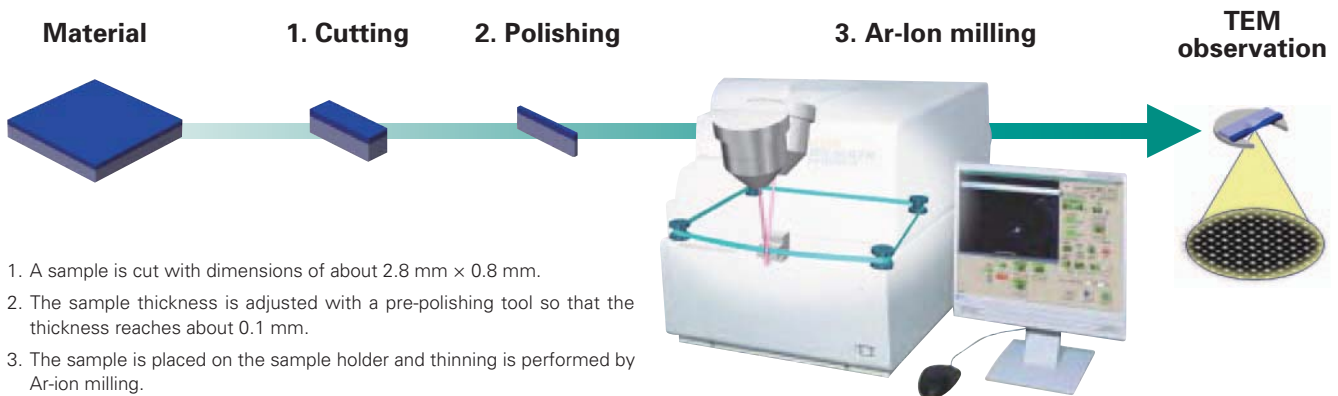
1. A sample is cut with dimensions of about 2.8 mm × 0.8 mm.
2. The sample thickness is adjusted with a pre-polishing tool so that the thickness reaches about 0.1 mm.
3. The sample is placed on the sample holder and thinning is performed by Ar-ion milling.

Table 1 Features of a thin-film sample prepared by the Ion Slicer Finishing Method.

	FIB-prepared thin-film sample	Ion Slicer-prepared thin-film sample	The Ion Slicer Finishing method
Positional accuracy	< 100 nm	~ 100 µm	< 100 nm
Width	~ 10 µm	~ 100 µm	~ 10 µm
Thickness	< 100 nm, Uniform	< 30 nm, Wedge-shape	< 100 nm, Uniform
Damage	Amorphous layer at 20 nm (30 kV) Ga contamination	Amorphous layer at 2 nm (2 kV) No Ga contamination	Amorphous layer at 2 nm (2 kV) Low Ga contamination

Fig. 3 Thin-film sample preparation process using the Ion Slicer Finishing Method.

(a) Thin-film sample preparation using FIB

Ga ion beam

FIB grid
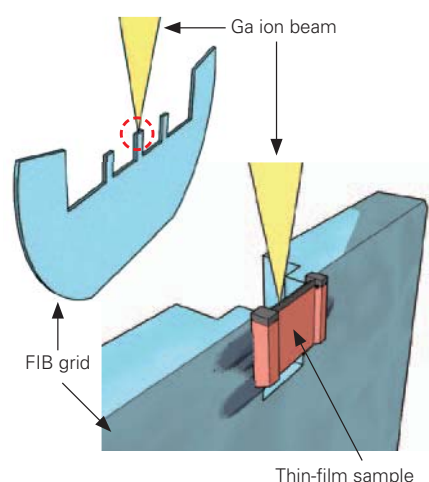
Thin-film sample

(b) FIB grid is loaded onto the sample holder.

Sample-fixed position

FIB grid

Sample holder
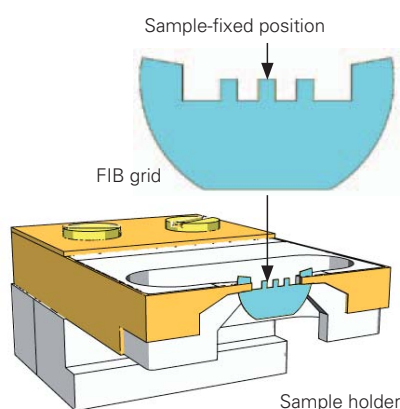
(c) Finishing for Ar-ion milling

+6°⇔ -6°
Rocking

Sample swing
+30°⇔ -30°

Ar-Ion
1kV~2kV

Sample holder

---
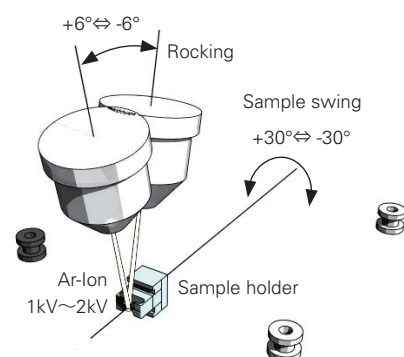
prepared thin-film sample are different from each other. The former sample (prepared by FIB) has good processing-position accuracy and uniform film-thickness. The latter sample (prepared by the Ion Slicer) features thinner sample thickness than that prepared by FIB, low sample damage and no contamination by Ga. When the Ion Slicer Finishing Method is applied to thin-film sample preparation, sample damage can be suppressed to minimum while the advantages of FIB are maintained, including a thin-film sample with high processing-position accuracy and with appropriate shape. The amount of the sample damage is comparable to that prepared by the Ion Slicer. Thus, the Ion Slicer Finishing Method dramatically improves the quality of the thin-film sample prepared by FIB.

Thin-film sample preparation procedures using the Ion Slicer Finishing Method

The following explanation presents the procedures of the Ion Slicer Finishing Method for an FIB-prepared thin-film sample.

1. A thin-film sample is prepared by the Bulk Pickup Method using FIB (**Fig. 3**(a)). At this time, the thin-film sample should be prepared around the center of the FIB grid.
2. The FIB grid with the fixed thin-film sample is loaded onto the sample holder dedicated to the Ion Slicer (Fig. 3(b)). The details of the dedicated sample holder will be explained in the next section.
3. Ar-ion irradiation using the Ion Slicer is performed on the sample. In this process, the masking belt is not used and an accelerating voltage of 1 to 2 kV is applied to the sample during thinning processing (Fig. 3(c)).

Development of the sample holder for finishing with the Ion Slicer

A dedicated sample holder (sample holder for finishing with the Ion Slicer), which enables Ar-ion irradiation onto an FIB-prepared thin-film sample, has been developed (**Fig. 4**(a)). This holder allows the FIB grid to be easily attached with the clipping method. Furthermore, combined use of a JEOL-developed FIB sample-holder adapter (Fig. 4(b)) makes it possible to directly

insert the FIB grid into the JEOL FIB system for thin-film sample preparation by FIB. After the completion of the thin-film sample preparation by FIB, removing the holder from the adapter enables us to place the sample onto the Ion Slicer for the subsequent Ar-ion beam irradiation. A series of these procedures can be easily made without transferring the sample with tweezers.

Development of the special-shape FIB grid

The most important point in the Ion Slicer Finishing Method is to prevent re-deposition of contaminants due to Ar-ion polishing onto the sample arising from Ar-ions irradiated onto the sample stub near the sample or onto the sample itself. This re-deposition arises mainly from the FIB grid with the fixed thin-film sample. To suppress the re-deposition, it is necessary to modify the shape of the FIB grid or to improve the method of fixing the sample to the FIB grid. As shown in **Fig. 5**, a special-shape FIB grid was made. This FIB grid was made of Mo or Ti because these elements are unlikely to be milled by Ar-ion irradiation. Furthermore, in order to suppress the re-deposition from the FIB grid during Ar-ion irradiation, a large space was created just beneath the sample fixing parts (shown in Fig. 5).

Examinations

Examination of re-deposition

The Ion Slicer Finishing Method was applied to two thin-film samples prepared by FIB. (Sample: Si single crystal, Ar irradiation conditions: 2 kV, 10 min). The special-shape FIB grid made of Mo was used for one sample, whereas the commercially-available FIB grid made of Cu was used for another sample. TEM observation was performed for the prepared thin-film samples (accelerating voltage: 200 kV) for comparison of re-deposition between the two samples. In the sample used with the commercially-available FIB grid made of Cu, large amounts of lined spots that were assumed to be re-deposition were observed (**Fig. 6**(a), (b)). On the other hand, in the sample used with the special-shape FIB grid made of Mo, no spots were seen (Fig. 6(c), (d)). These observation results

Fig. 4 Sample holder for finishing with the Ion Slicer.

FIB
Model: JIB-4000

Ion Slicer
Cryo Ion Slicer

(b)
FIB sample-holder adapter

(a)
Sample holder for finishing with Ion Slicer

Fig. 5 Special-shape FIB grid.

Post

Mo or Ti

Fixing part

Space
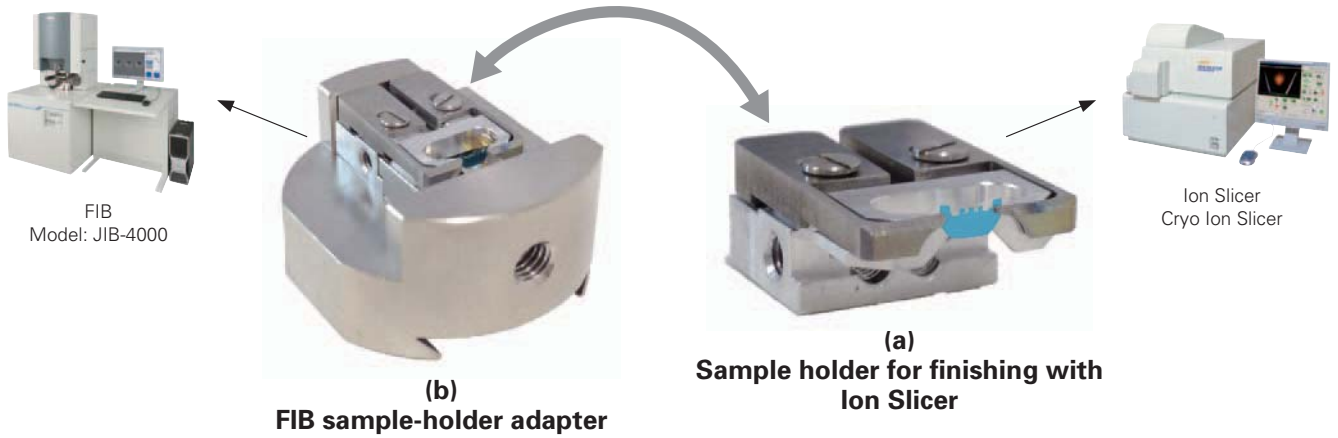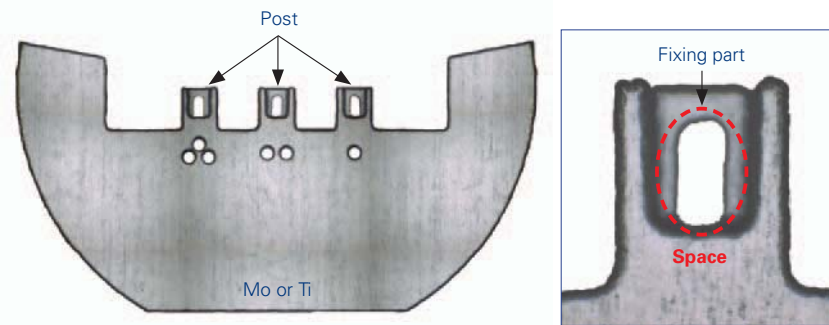
Fig 6 Comparison of re-deposition depending on FIB grid (TEM images).

(a) Thin-film sample

FIB grid

(c) Thin-film sample

FIB grid

(b) The whole area is re-deposited.

Redeposition

2 μm

(d) No re-deposition

2 μm
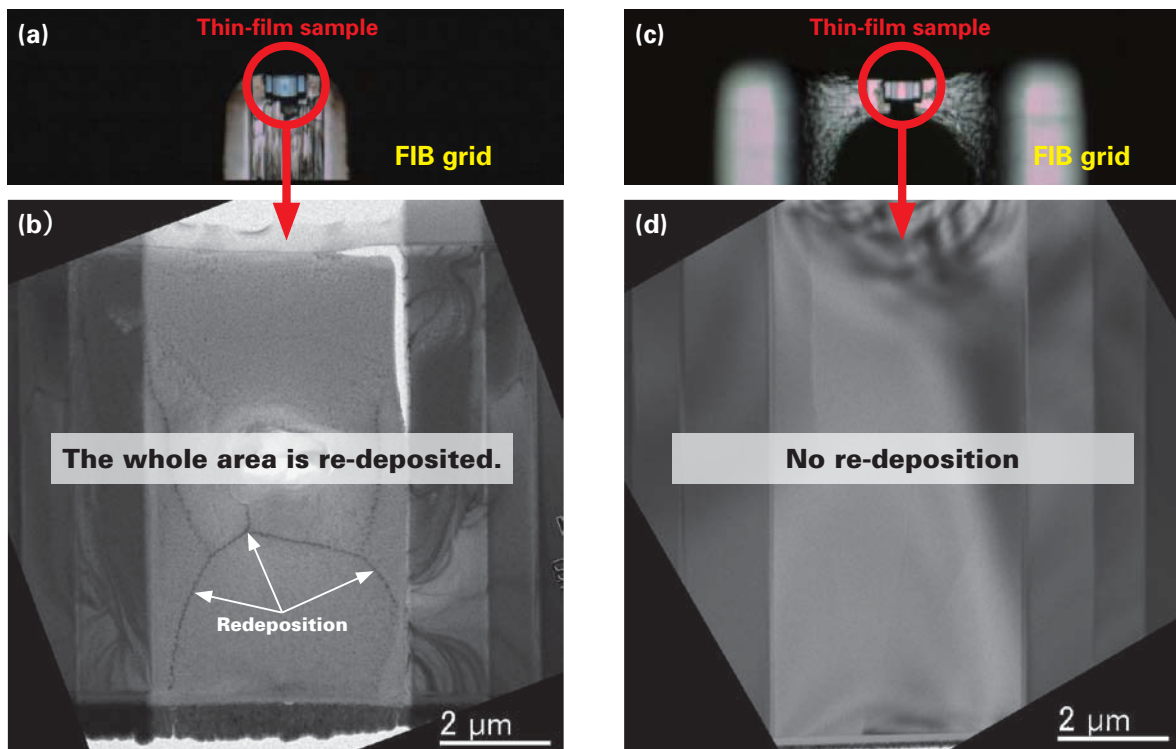
(a)(b) The commercially-available FIB grid made of Cu was used.
Enormous amounts of lined spots were observed on the sample.

(c)(d) The special-shape FIB grid made of Mo was used. No lined spots were observed.

confirm that the use of the special-shape FIB grid enables finishing by the Ion Slicer with no re-deposition.

Examination of amorphous layers

To confirm an effect of removing sample damage due to the Ion Slicer Finishing Method, the authors evaluated the thickness of amorphous layers of a thin-film sample prepared by the Ion Slicer Finishing Method. A sample (Si single crystal) which was thinned using FIB (accelerating voltage: 30 kV) was subject to finishing using the Ion Slicer with an Ar-ion beam (accelerating voltage: 2 kV, irradiation time: 5 min). Furthermore, that sample was subject to cross-section milling for TEM observation (accelerating voltage: 200 kV) so as to measure the thickness of amorphous layers formed on the top surface of the sample.

For comparison, the thicknesses of amorphous layers were measured for samples prepared only by FIB milling (accelerating voltage for the final milling: 5 kV, 10 kV, 30 kV) and for a sample prepared only by the Ion Slicer (accelerating voltage for the final milling: 2 kV).

Measurement results are presented in **Fig. 7**. For a sample prepared using FIB (accelerating voltage: 30 kV), the thickness of the amorphous layers was 22 nm. On the other hand, for the sample prepared using the Ion Slicer Finishing Method, the thickness dramatically decreased to 2 nm. Thus, this method effectively removes the amorphous layers arising from FIB milling. Furthermore, the thickness prepared only by the Ion

Slicer was approximately 2 nm. As a result, it was revealed that the quality of the sample prepared using the Ion Slicer Finishing Method is comparable to that prepared by Ar-ion milling.

Applications Using Various Samples

Examinations of the Ion Slicer Finishing Method explained up to now, were also performed for samples of LED (GaN), GaAs (quantum well), Si single crystal and SrTiO$_3$ single crystal. These examinations results are presented below.

GaN-LED

When a GaN-LED sample is subject to thin-film preparation using FIB, a TEM image taken from this sample does not show very sharp contrast. This sample was used for the effectiveness of the Ion Slicer Finishing Method. In our experiment, TEM images were acquired from both a thin-film sample prepared by the Ion Slicer Finishing Method and that prepared only by FIB milling, then the multiple quantum well structures of the two samples were compared based on the TEM images. A TEM image of the thin-film sample prepared only by FIB milling is shown in **Fig. 8**(a). The final milling with a 3 kV Ga-ion beam was applied to this sample. Next, a TEM image of the thin-film sample prepared using the Ion Slicer Finishing Method is shown in Fig. 8(b). For this sample, the final FIB milling was applied at an accelerating voltage of 5 kV, and subsequent finishing with

Fig. 7 Thicknesses of amorphous layers (sample: Si crystal).
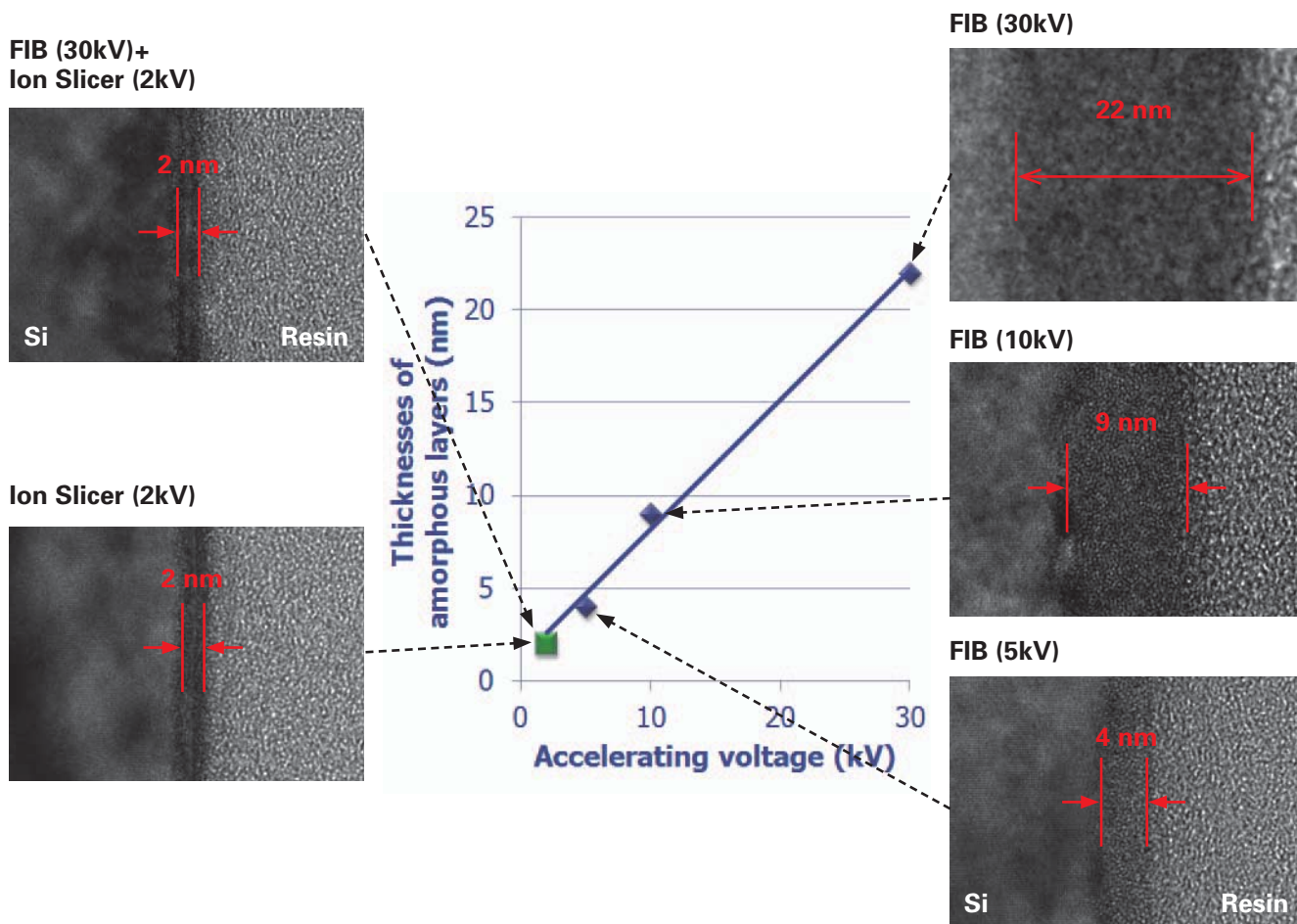
Fig. 8 TEM images of multiple quantum well structures of GaN/AIGaN.
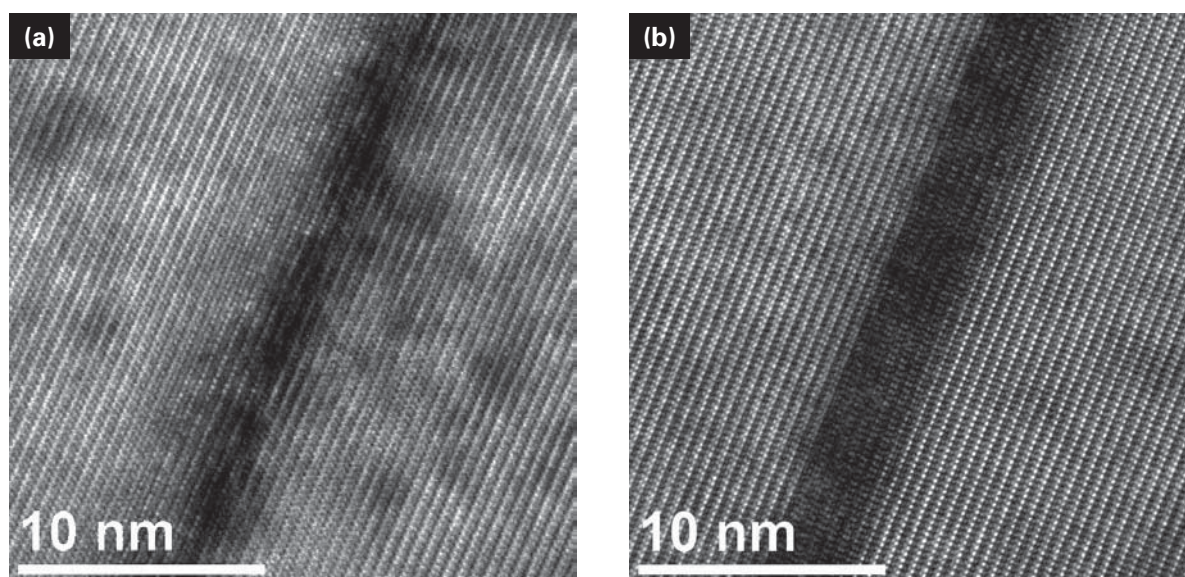
(a) Sample prepared only using FIB (accelerating voltage for the final milling: 3 kV).

(b) Sample prepared using both FIB (accelerating voltage for the final milling: 5 kV) and the Ion Slicer Finishing Method (accelerating voltage for the final milling: 2 kV and 1 kV).

the Ion Slicer was performed with an Ar-ion beam (accelerating voltage: 2 kV, irradiation time: 5 min) and further, performed with 1 kV accelerating voltage and 5 min beam irradiation. Both samples were subjected to TEM image observation at an accelerating voltage of 200 kV. As shown in Fig. 8(b), the TEM image of the sample prepared by the Ion Slicer Finishing Method does not exhibit black-bleed-like contrast which appeared in the TEM image of the FIB-prepared sample (Fig. 8(a)). Thus, the borders of multiple layers of quantum well structures are clearly visible. Furthermore, a sharper lattice image was observed in Fig. 8(b). This result reveals that when finishing with the Ion Slicer is applied to an FIB-prepared thin-film sample, a thin-film sample with less damage is prepared.

GaAs multiple layers

A sample composed of GaAs multiple quantum well structures was used to examine the effectiveness of the Ion Slicer Finishing Method.

TEM images were acquired from both a thin-film sample prepared by the Ion Slicer Finishing Method and that prepared only by FIB milling, then GaAs multiple quantum well structures of the two samples were compared based on the TEM images. A TEM image of the thin-film sample prepared only by FIB milling is shown in **Fig. 9**(a). The final milling with a 3 kV Ga-ion beam was applied to this sample. Next, a TEM image of the thin-film sample prepared using the Ion Slicer Finishing Method is shown in Fig. 9(b). For this sample, the final FIB milling was applied at an accelerating voltage of 30 kV, and subsequent finishing with the Ion Slicer was performed with an Ar-ion beam (accelerating voltage: 2 kV, irradiation time: 7 min). Both samples were subject to TEM image observation

at an accelerating voltage of 200 kV. As shown in Fig. 9(b), the TEM image of the sample prepared by the Ion Slicer Finishing Method exhibits sharper contrast of the borders of multiple layers of quantum well structures than the TEM image taken from the FIB-prepared sample (Fig. 9(a)). In addition, a lattice image in Fig. 9(b) is sharper than Fig. 9(a). This result demonstrates that the Ion Slicer Finishing Method achieves preparation of a thin-film sample with less damage.

Si single crystal

A Si single crystal sample was used to examine the effect for removing damage layers arising from the Ga ion beam preparation. First, a thin-film sample was prepared using FIB and the sample was subject to TEM image observation (accelerating voltage: 200 kV) (**Fig. 10**(a)). This sample was prepared with a Ga-ion beam at 30 kV. After that, the sample was subject to finishing with the Ion Slicer for TEM image observation (Fig. 10(b)). The processing conditions of this finishing are as follows: Beam: Ar-ion beam, Accelerating voltage: 2 kV, Irradiation time: 7 min. As shown in the TEM image of Fig. 10(a), in the sample before subject to the Ion Slicer Finishing Method, black-bleed-like contrast appears as indicated with circles. On the other hand, after the sample is subject to this method, black-bleed-like contrast disappears in the TEM image (Fig. 10(b)). This result verifies that applying the Ion Slicer Finishing Method removes sample damage caused by Ga-ion irradiation onto the sample.

SiTiO$_3$ single crystal

A thin-film sample of SrTiO$_3$ was prepared by the Ion Slicer Finishing Method. In the FIB final milling, accelerating voltage
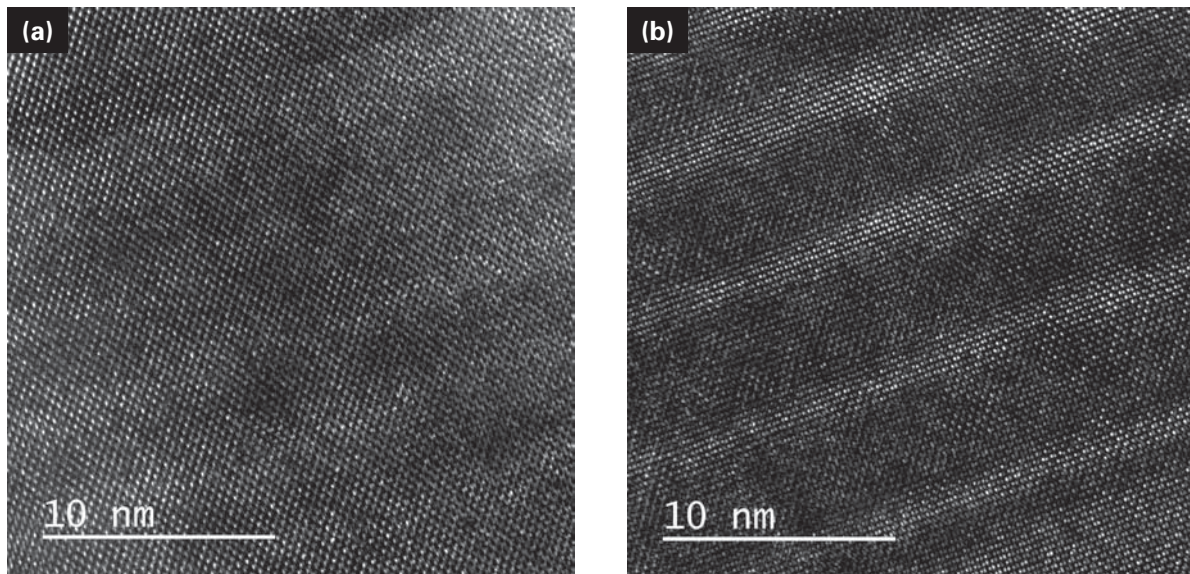
(a) Sample prepared only using FIB (accelerating voltage for the final milling: 3 kV).

(b) Sample prepared using both FIB (accelerating voltage for the final milling: 30 kV) and the Ion Slicer Finishing Method (accelerating voltage for the final milling: 2 kV).

Fig. 10 TEM image of Si single crystal.
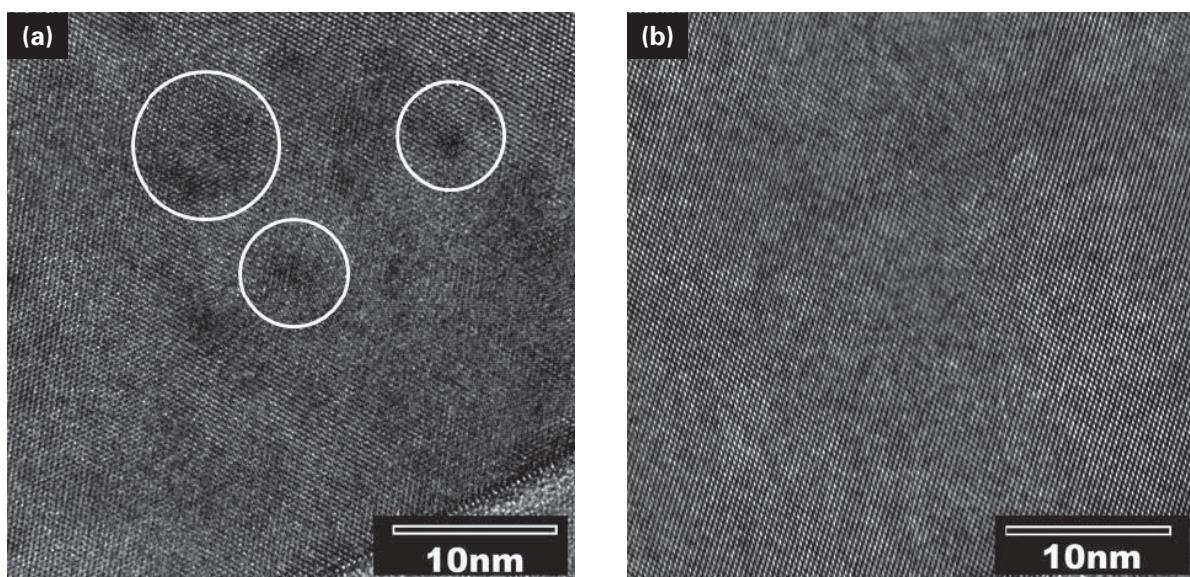
(a) Sample prepared by FIB milling (accelerating voltage: 30 kV).

(b) Sample (a) further subject to the Ion Slicer Finishing Method (accelerating voltage: 2 kV).

Fig. 11 STEM-HAADF images of SrTiO₃ single crystal.
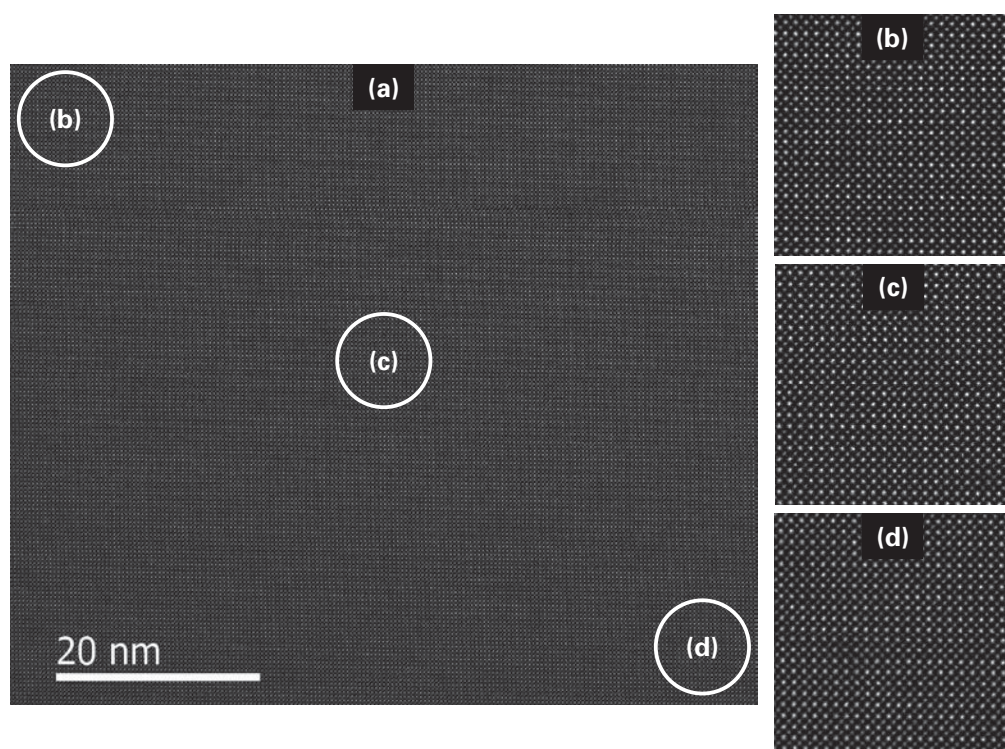
(a) Sample prepared using both FIB (accelerating voltage for the final milling: 5 kV) and the Ion Slicer Finishing Method (accelerating voltage for the final milling: 2 kV and 1 kV).

(b) (c) (d) Enlarged images of the corresponding circles indicated in Fig. 11(a).

is 5 kV. In the Ion Slicer Finishing Method, an Ar-ion beam with 2 kV accelerating voltage and 5 min irradiation time are first applied, and then 1 kV accelerating voltage and 10 min irradiation time are further applied. STEM-HAADF images of these samples taken with the JEM-ARM200F are shown in **Fig. 11** (accelerating voltage: 200 kV). As shown in Fig. 11(a), a high-resolution HAADF image with high uniformity and sharp contrast is obtained over a wide area, it is demonstrated that this sample has uniform thickness and less sample damage. This result confirms that the Ion Slicer Finishing Method applied to an FIB-prepared sample features both uniform sample thickness achieved by FIB milling and low sample damage offered by the Ion Slicer Finishing Method.

Conclusion

Our experiments presented in this article revealed that irradiation of a low-energy Ar-ion beam onto an FIB-prepared thin-film sample using the Ion Slicer makes it possible to perform higher quality sample preparation. Furthermore, the development of the special-shape FIB grid and the FIB-Ion Slicer common holder facilitated the transfer of the sample from the FIB system into the Ion Slicer, and improved the efficiency of the sample-preparation procedures. The Ion Slicer itself can prepare a thin-film sample with high quality, but the Ion Slicer

cannot pinpoint a narrow area for thin-film sample preparation. To the contrary, FIB can easily prepare a thin-film sample from a specific site, but the formation of damaged layers due to Ga-ion irradiation is unavoidable. The Ion Slicer Finishing Method is a breakthrough technique that utilizes both the Ion Slicer and the FIB system. As a conclusion, the authors believe that, by selecting an appropriate method from the Ion Slicer, FIB and the Ion Slicer Finishing Method according to sample properties or analytical purposes, it becomes possible to perform thin-film sample preparation for more kinds of samples with easier operation and higher quality.

References

[1] Suzuki, T., Shibata, M., Okunishi, E., Endo, N., and Kuba, T.; *Journal of The Japan Institute of Metals and Materials*, **68-5**, 293-198 (2004) (in Japanese)

[2] Yasuhara, A.; *JEOL News*, **40**, 46-49 (2005).

New Gas Chromatography/ High Resolution Time-of-Flight Mass Spectrometer JMS-T200GC "AccuTOF GCx"

Masaaki Ubukata   JEOL USA, Inc.

General

As mass spectrometry (MS) is used in a wide range of scientific fields today, different types of MS systems are available to meet different research objectives and applications. Compared to other scientific instruments, the most powerful feature of MS is its high sensitivity. Some of the commercial MS systems can easily detect and analyze ultra trace components in the fg (10^{-15} g) order. Time-of-flight MS (TOFMS) and magnetic sector MS systems, capable of acquiring high resolution (HR) and high mass accuracy data, make it possible to determine elemental compositions from the exact mass data of the detected ions. Thus, MS is being used in a variety of fields as a powerful analytical instrument for qualitative and quantitative examination of ultra trace components.

In the fall of 2004, JEOL announced the JMS-T100GC AccuTOF GC, the first gas chromatography/high resolution time-of-flight mass spectrometer (GC/HR-TOFMS) developed in Japan. The system has been received well by many users. JEOL has recently completed the 4th generation GC/HR-TOFMS, JMS-T200GC AccuTOF GCx, featuring higher sensitivity and higher mass resolution. In this article, we will provide an overview of the AccuTOF GCx, and describe its advantages in comparison to the original system.

System Overview

Figure 1 shows an external view of the system. The AccuTOF GCx supports the same ionization techniques as the original system, that is, electron ionization (EI), chemical ionization (CI), field ionization (FI), as well as desorption electron ionization (DEI), desorption chemical ionization (DCI), and field desorption (FD) ionization using specialized direct sample inlet probes.

Figure 2 shows the low acceleration ion transfer and orthogonal acceleration (oa)-TOFMS systems. The low acceleration ion transfer system, using a split lens and the potential difference of deflectors, eliminates 99% or more of the helium ions from the GC carrier gas before the oa-TOFMS system. This feature maximizes detector lifetime. The oa-

TOFMS system incorporates an ion accelerating mechanism and reflectron. The ion beam is spatially focused by the ion accelerating mechanism, and is further time-focused by the reflectron to accomplish high resolution mass analysis at all times. While the oa-TOFMS remains nearly identical to the original system, the parameters were reviewed and optimized to achieve higher mass resolution. An isolation valve between the ion source-ion transfer unit and the oa-TOFMS makes it possible to bring the ion source and ion transfer unit to atmospheric pressure while maintaining a high vacuum in the oa-TOFMS.

The ion detector and electric circuits of the detector system were also modified and optimized to achieve higher resolution and higher sensitivity, simultaneously. The data detection system uses an ADC 4 GHz-digitizer to acquire mass spectral data with ample data points. The system enhances the reproducibility of the mass accuracy (horizontal axis of mass spectrum) and the intensity (vertical axis of mass spectrum) of the ion peaks detected.

The AccuTOF GCx achieves a sensitivity level 3 times higher and a mass accuracy level twice higher than the original system, while the dimensions of the system remain unchanged from the older models.

Basic Performance

The basic performance of the AccuTOF GCx is as follows:
- Ionization mode: EI, CI, FI, DEI, DCI and FD
- GC/EI sensitivity: OFN 1 pg, S/N>300
- Mass resolution: >10,000 (FWHM)
- Mass accuracy: <1.5 mDa or 4 ppm (RMS)
- Mass range: m/z 4 to 6,000
- Spectrum recording speed: Up to 50 spectra/sec

The GC/EI sensitivity is specified as S/N 300 or higher for 1 pg of octafluoronaphthalene (OFN). **Figure 3** shows the extracted ion chromatogram (EIC) of the molecular ion at m/z 271.9867 and EI mass spectrum when 1 pg of OFN was analyzed. Both the EIC and EI mass spectrum demonstrate a high S/N ratio. **Figure 4** shows the EIC of the molecular ion acquired from 100 fg of OFN that was analyzed continuously

>> 11 Dearborn Road, Peabody, MA 01960, USA | E-mail: mubukata@jeol.com

Fig. 1 JMS-T200GC "AccuTOF GCx"

Fig. 2 Low-acceleration ion transfer system and oa-TOFMS system

Electrostatic lenses

Source magnet

Sample ions

Helium ions

Plug & socket type chamber (EI, CI)

Low-acceleration ion transfer system

oa-TOFMS system
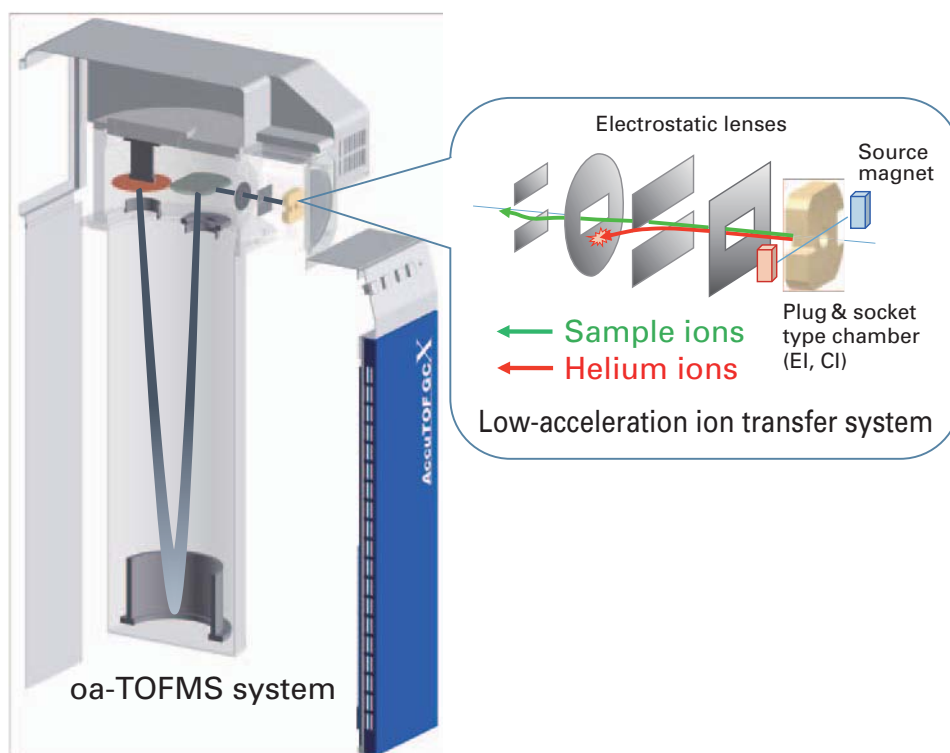
8 times. The figure also shows the peak area, the relative standard deviation, and the instrument detection limit (IDL) calculated from these data. Despite the ultra micro amount of 100 fg, the relative standard deviation was 5.2%, demonstrating high stability. The IDL, which was statistically calculated from the repeated accuracy of the peak areas with a given level of reliability, was 16 fg. As the data above demonstrates, the AccuTOF GCx is a GC/MS system that combines high sensitivity and high stability in ultra micro analysis.

Figure 5 compares the data acquired by the AccuTOF GCx and the conventional system, showing the peaks of $C_6F_{11}^+$, a fragment ion of perfluorokerosene, which is used widely as a mass calibration sample for GC/MS, and $C_7H_{21}O_4Si_4^+$ observed as a background ion from the GC column. These ions, being extremely close in exact mass, were not completely separated in the original system (bottom of Fig. 5; mass resolution: 5,105; peak FWHM: 55 mDa). The AccuTOF GCx, with a specified resolution of 10,000, separated these peaks completely (top of

Fig. 3 OFN 1 pg: EIC of *m/z* 271.9867 and EI mass spectrum

Fig. 3 OFN 1 pg: EIC of *m/z* 271.9867 and EI mass spectrum

Fig. 4 OFN 100 fg: EICs of *m/z* 271.9867 and IDL
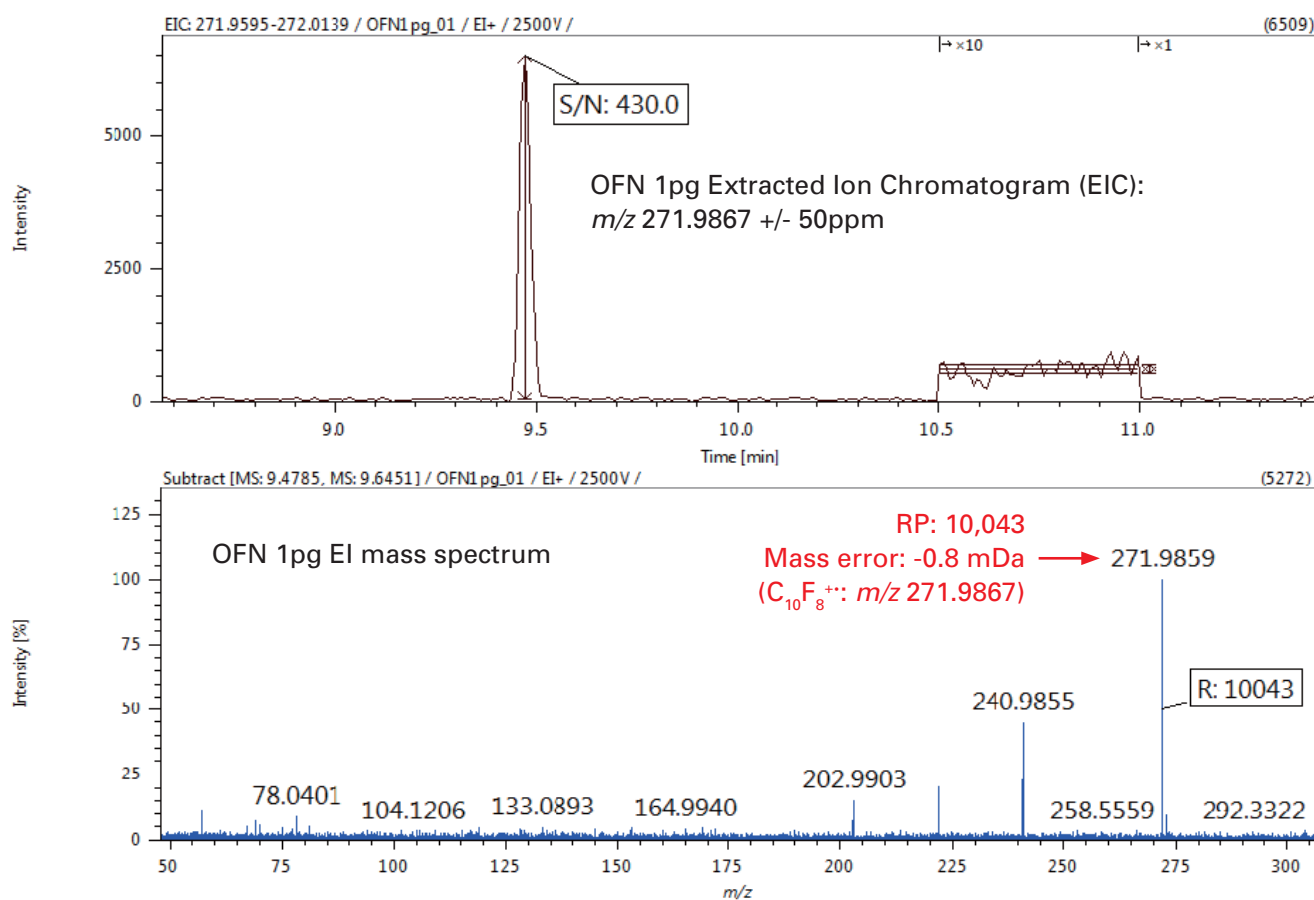
Fig. 4 OFN 100 fg: EICs of *m/z* 271.9867 and IDL
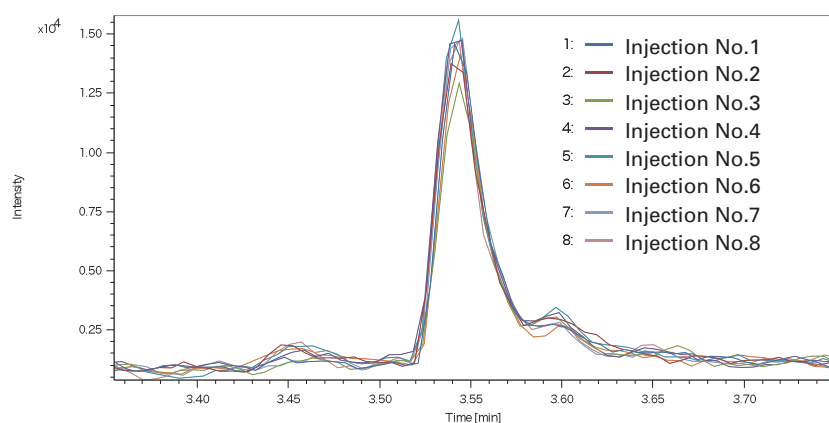
Injection No.	Peak Area
1	65745
2	67212
3	58394
4	70698
5	65897
6	65604
7	65994
8	65230

Relative Standard Deviation (%)	5.2
IDL (fg)	16

Fig. 5; mass resolution: 10,476; peak FWHM: 27 mDa).

As the mass resolution is improved, so is the mass accuracy, which is specified at 1.5 mDa or 4 ppm or less. The system easily acquires mass spectral data featuring a high level of mass accuracy in all ionization techniques. This allows the user to determine the molecular formula of a target compound from the accurate mass data of the molecular ions and protonated molecules observed by soft ionization techniques such as CI and FI, and the structural formula of a target compound from the accurate mass data of fragment ions observed by hard ionization such as EI. **Figure 6** shows the EI and FI mass spectra of allyl(tert-butyl)dimethylsilane and the elemental

Fig. 5 Comparison of mass resolution and ion peak shape

280.9818
$C_6F_{11}{}^+$
281.0508
$C_7H_{21}O_4Si_4{}^+$

RP: 10,476
Δm: 27mDa
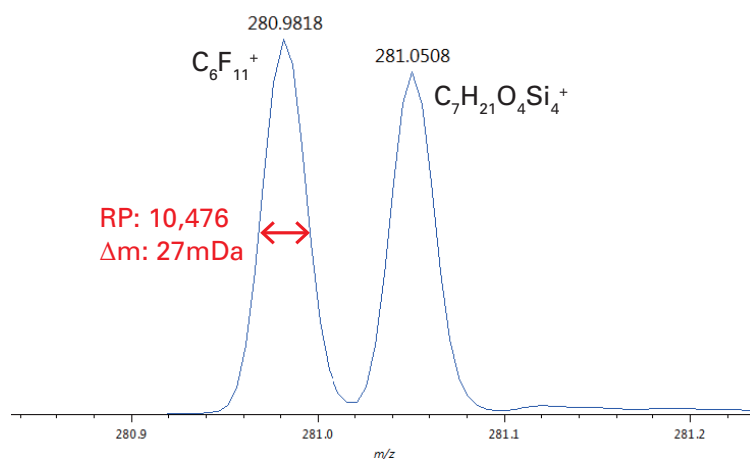
JMS-T200GC AccuTOF GCx (4th model)

280.9824
$C_6F_{11}{}^+$
281.0501
$C_7H_{21}O_4Si_4{}^+$

RP: 5,105
Δm: 55mDa
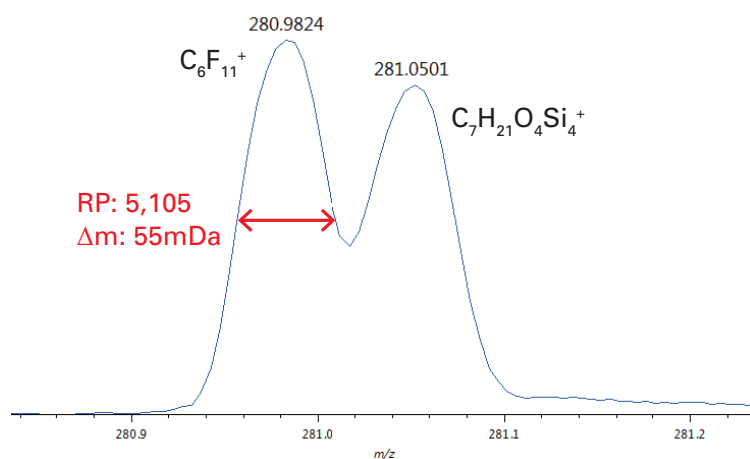
JMS-T100GC AccuTOF GC (1st model)

Fig. 6 EI and FI mass spectra of Allyl(tert-butyl)dimethylsilane

EI+

1
73.0478

2
99.0625

3
115.0932

59.0326

M+•
156.1343

FI+
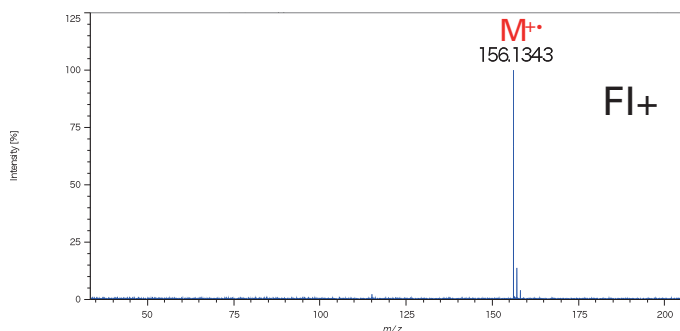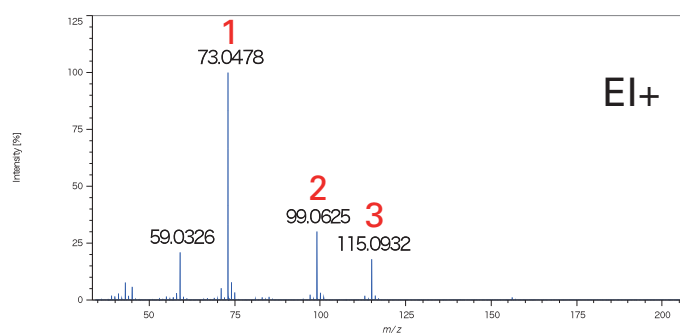
Mode	Ion	Obs. m/z	Error (mDa)	Formula
EI+	1	73.0478	1.0	C_3H_9Si
	2	99.0625	0.0	$C_5H_{11}Si$
	3	115.0932	-0.6	$C_6H_{15}Si$
FI+	M+•	156.1343	1.5	$C_9H_{20}Si$

m/z 99
m/z 73 (+H)
m/z 115
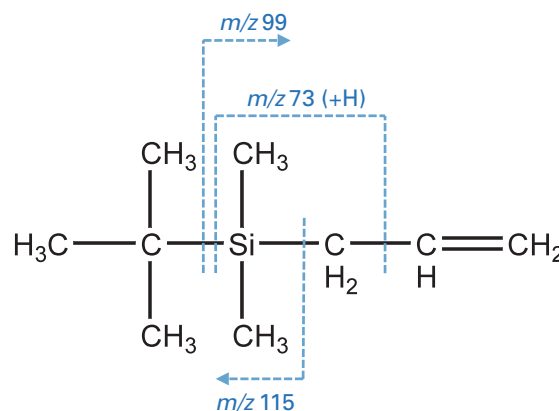
composition of the ions detected. While a small molecular ion was observed at *m/z* 156 in the EI mass spectrum, its intensity was extremely low. EI, being the hardest ionization technique, can detect many fragment ions other than molecular ions. However, it can often fail to detect the molecular ions. When analyzing an unknown sample, it is extremely difficult to determine from the EI spectrum alone if the ion with the highest mass is a molecular ion or a fragment ion. On the other hand, FI is capable of detecting molecular ions most easily, compared to other soft ionization techniques. In the FI mass spectrum of allyl(tert-butyl)dimethylsilane, the molecular ion at *m/z* 156 was detected with the highest intensity in the mass spectrum. From the accurate mass data of the molecular ion at *m/z* 156 in the FI mass spectrum, the elemental composition of this ion was identified as $C_9H_{20}Si$, the same molecular formula as allyl(tert-butyl)dimethylsilane. Also, the accurate mass data for the fragment ions observed in the EI mass spectrum provided the elemental composition data that indicated a segment of the structural formula of allyl(tert-butyl)dimethylsilane. Thus, combining the elemental composition data acquired by multiple ionization techniques, the AccuTOF GCx is capable of highly reliable qualitative analysis.

Another powerful feature of the AccuTOF GCx is a wide mass range from *m/z* 4 to 6,000. Typical GC/MS analysis, especially with EI, uses a mass range up to *m/z* 600. Meanwhile, FD is often used for samples having relatively large masses such as synthetic polymers and organic metal complexes. The mass range of the AccuTOF GCx up to *m/z* 6,000 enables analysis of these samples (**Fig. 7**). FD is one of the direct MS techniques using a specific direct sample inlet probe. While typical GC/MS systems are almost exclusively designed for GC/MS analysis, the AccuTOF GCx also supports two additional direct sample inlet probes (Direct Exposure Probe, Direct Insertion Probe).

The AccuTOF GCx features a spectrum recording speed of up to 50 spectra/sec. This makes the AccuTOF GCx a powerful tool for any applications that require extremely fast data acquisition such as high speed gas chromatography (Fast GC) and comprehensive 2D gas chromatography (GCxGC).

The AccuTOF GCx is a next generation GC/MS system that combines high sensitivity, high mass resolution, high mass accuracy, wide mass range, and high speed spectrum recording.

EI/FI/FD combination ion source

The EI/FI/FD combination ion source is an optional accessory for the AccTOF GCx, a single ion source that supports sample analysis using 3 different ionization techniques (GC/EI, GC/FI, FD). An ionization mode is selected by replacing the probe. Probes can be changed while keeping the ion source in high vacuum, minimizing system downtime for an ionization mode switch. The effectiveness of this unique EI/FI/FD combination ion source has been valued by many users since it was first incorporated in the second generation system, the AccuTOF GCv. As discussed above, because the TOFMS base unit accomplishes high sensitivity and high mass resolution, the EI/FI/FD combination ion source acquires mass spectral data that features higher sensitivity and higher resolution.

New software "msAxel"

The AccuTOF GCx is accompanied by a new software package, msAxel, for system control and data analysis (**Fig .8**). msAxel has an intuitive user interface in which each view is designed to facilitate access to all necessary information. msAxel also includes a Tuning Assistant, one of the features of the previous software, to optimize the system conditions. Tuning

Fig. 7   Polystyrene 5200 FD mass spectrum

$[H-(C_8H_8)_{57}-C_4H_9 + Li]^+$

6000.6669
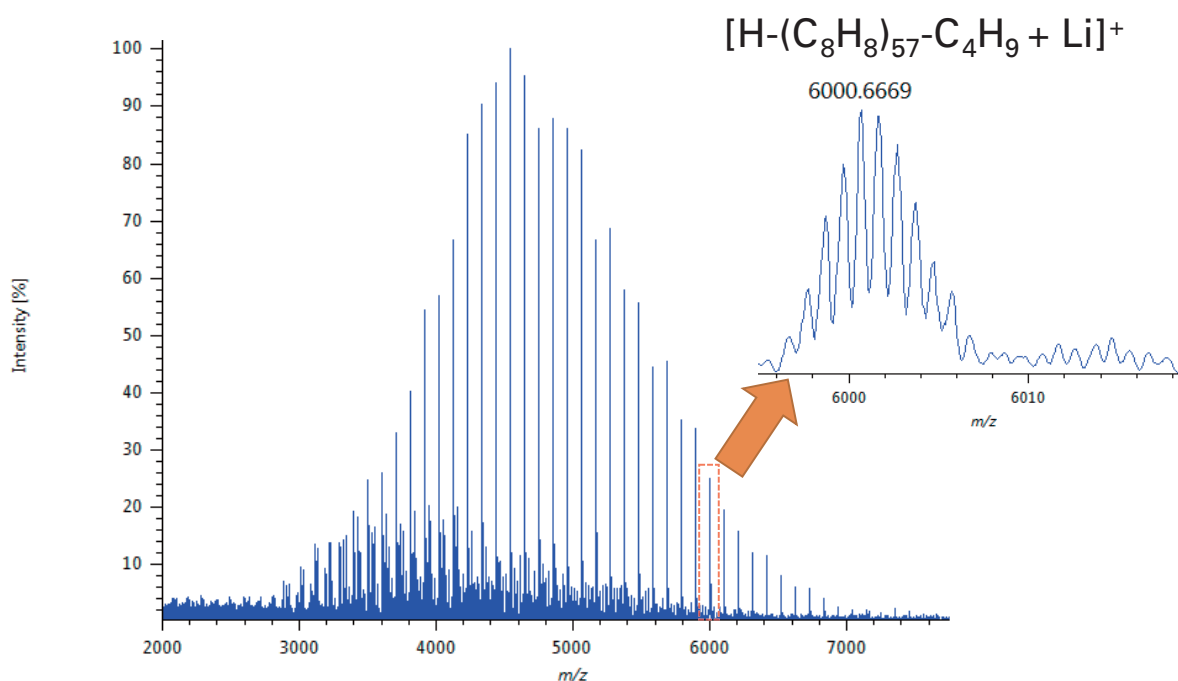
Assistant is supported in all ionization modes.

The most powerful feature of msAxel is that it enables speedy setup of data processing conditions from a single view. The system accomplishes the steps listed below, which are essential in mass data analysis, under the preset conditions, as it acquires the mass spectrum.

1. Detect ion peaks
2. Determine the center point of ion peak
3. Calculate the exact mass, ion peak intensity/area
4. Create an ion peak list based on the data above

Furthermore, unlike the original software, msAxel can search the NIST library database and determine elemental compositions based on the peak list created in the process above. Accomplishing these steps while maintaining the profile mass spectrum, msAxel simplifies the data analysis process, and also

allows the user to process the data while examining ion peaks that have similar exact masses.

Summary

The AccuTOF GC series has been appreciated by many users since the 1st generation AccuTOF GC system was introduced in 2004. The 4th generation AccuTOF GCx is JEOL's latest GC/HR-TOFMS system that combines the most advanced hardware and software components. It is a powerful and versatile system that is effective as a TOFMS for elemental composition determination, as a tool for advanced gas chromatography techniques such as Fast GC and GCxGC, and as a direct MS system that uses direct sample inlet probes. We expect that the AccuTOF GCx will be fully utilized in a wide range of applications, thus contributing to the advancement of science and technology.

Fig. 8 msAxel: Main and Data Processing Views

msAxel Main view
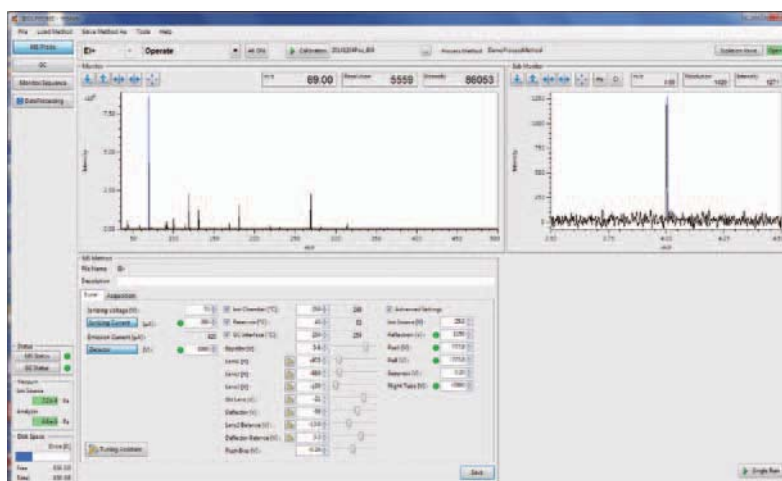
msAxel Data Processing view
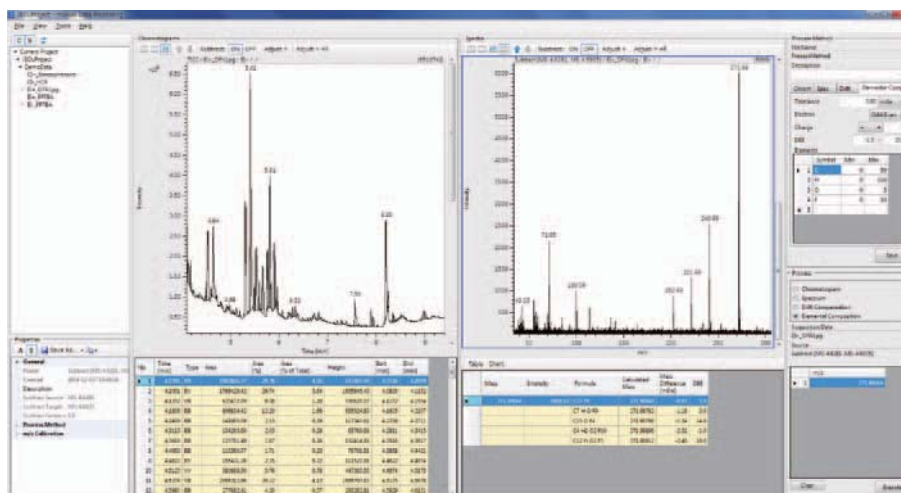
Introduction of JEOL Products

A new design of microwave unit. Much better sensitivity using 'High Sensitivity Mode'

Next Generation
Electron Spin Resonance Spectrometer

JES-X3 Series

Recently, it has been widely accepted that even relatively few unpaired electrons in a sample can affect the function of the material, so lower detection limits (higher sensitivity) is required of ESR measurements.

JEOL has achieved higher sensitivity by developing a low-noise Gunn oscillator for its new spectrometer, the JES-X3 series.

New functions for data acquisition and analysis enable a smooth transition from initial experiment selection to final detailed measurement.

- New Auto-tuning that has better reproducibility and shorter tuning time.
- Fully flexible sequential measurements including randomized values of parameters, e.g. sample temperature, microwave power, etc.
- A foot operated trigger (option) to start data measurement can be used to minimize dead time after reagents are mixed to generate short lived radicals.

Major New Functions

- Easy-to-use operation interface under Windows®7
- Hands-free measurement start using foot switch
- Both progressive and randomized settings of sequential measurement parameters possible.
- Improved display of multi-dimensional data.
- Batch processing of sequentially measured data, including background subtraction.

Major Features

- For measuring radicals generated by photo-irradiation, the standard universal cavity has an optical irradiation window which has high transmittance.
- High stability Auto-tuning.
- Each attachment easy to attach and detach.
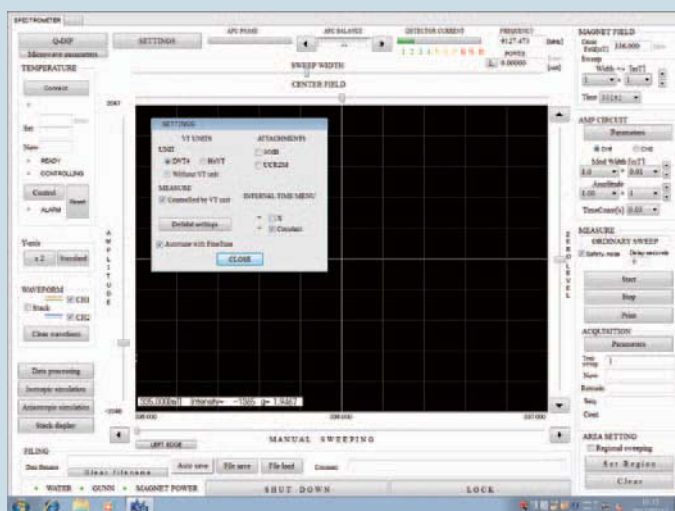
Easy-to-use Windows®7 user interface
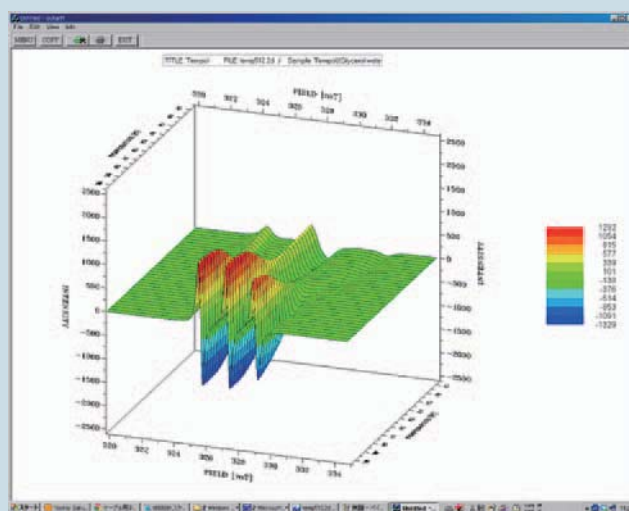
User customizable 3D display

Introduction of JEOL Products

Simple, Robust, Versatile

JMS-T100LP
AccuTOF LC-plus 4G

The AccuTOF LC-plus 4G, the third generation of the successful AccuTOF LC series, is a simple, robust and versatile atmospheric pressure ionization high-resolution time-of-flight mass spectrometer (API-HRTOFMS).

It can provide solutions for a wide variety of fields with JEOL's unique ionization technologies, DART and ColdSpray, in addition to the standard electrospray ionization (ESI), the most widely used ionization technique for LC/MS.

DART (Direct Analysis in Real Time)
DART mass spectrometer
from the inventor of DART

With the optional DART ion source, samples with various states and shapes can be analyzed directly without any sample preparation.

DART was born in 2003 at the mass spectrometry applications laboratory of JEOL USA, Inc. Among a series of new ionization techniques, which were late termed "ambient ionization," DART was the first to be invented and the first to be commercialized in 2005.

LC/MS

The AccuTOF LC-plus 4G is a simple and robust LC/MS system. It offers a wide variety of applications for LC/MS with optional Atmospheric Pressure Chemical Ionization (APCI) source, in addition to the standard orthogonal ESI source. Accurate mass measurements in LC/MS can be made routine by automating the introduction of the internal mass reference compound with the optional Auto-Injection Valve.

ColdSpray

With the optional ColdSpray ion source, thermally labile analytes, including self-assembling supra molecules, some classes of organometallic complexes, short-chain double stranded DNAs, can all be analyzed intact.

ColdSpray ionization was developed by Prof. Kentaro Yamaguchi, et al., of Kagawa School of Pharmaceutical Sciences, Tokushima Bunri University (previously Chiba University) and the result of a project funded by the Japan Science and Technology Agency (JST).

JEOL Ltd.

1-2 Musashino 3-chome Akishima Tokyo 196-8558 Japan   Sales Division Tel. +81-3-6262-3560   Fax. +81-3-6262-3577
www.jeol.com   ISO 9001 • ISO 14001 Certified